Kinetic-magnetohydrodynamic Hybrid Simulation Study of Energetic-particle Driven Instabilities in Heliotron J

Panith ADULSIRISWAD

Kinetic-magnetohydrodynamic Hybrid Simulation Study of Energetic-particle Driven Instabilities in Heliotron J

Panith ADULSIRISWAD

A thesis submitted in partial fulfillment of the requirements
for the degree of
Doctor of Science

Graduate School of Energy Science
Kyoto University
Japan

2021

Abstract

In this thesis, the energetic-particle (EP) driven magnetohydrodynamics (MHD) instabilities and their interactions with the EPs in Heliotron J, a low magnetic shear helical-axis heliotron, were numerically investigated and clarified with MEGA, the hybrid MHD-EP simulation code. A thorough understanding of the interplay between EP and shear Alfvén wave (SAW) is indispensable for the development of the suppression mechanism of the EP-driven MHD instabilities in the magnetic confinement fusion device. This can also be used in the optimization of the magnetic field. In the stellarator and heliotron magnetic configurations (toroidally asymmetric device), the continuous (steady-state) operation is inherently achieved; however, the additional toroidally asymmetric magnetic components (e.g. helicity and bumpy) create additional EP-SAW and SAW-SAW interactions. This potentially leads to more energy channels between EP and SAW and new coupling-type gap modes (e.g. helicity-induced Alfvén eigenmode). Heliotron J is the quasi-isodynamic optimized low magnetic shear helical-axis heliotron in Kyoto University. The quasi-isodynamic optimization is partially achieved in the corner section of Heliotron J. Heliotron J has the flexibility to adjust the magnetic field configuration by varying the current in the external coils. It was designed to obtain the compatibility between MHD stability and particle transport. In terms of MHD stability, the magnetic well is produced in the whole plasma region. This is sufficient to suppress the pressure-driven MHD instabilities up to $< \beta_b > \geq 3\%$. For the particle transport, the particle transport by neoclassical (NC) ripple is ameliorated by the external control of the bumpy magnetic field component that has an opposite sign to the toroidicity component. Heliotron J shares similar properties to other new-generation optimized stellarator devices such as low magnetic shear, helical-axis, and the vacuum magnetic well. Due to its low magnetic shear, the commonly observed EP-driven MHD instabilities in Heliotron J are energetic-particle mode (EPM) and global Alfvén eigenmode (GAE). The investigated MHD equilibria in this thesis are based on the experimental parameters of the control of EP-driven MHD instability by ECH/ECCD experiment in Heliotron J. In this experiment, the n/m=1/2 EPM and the n/m=2/4 GAE were destabilized and experimentally observed at r/a $\approx$ 0.8 and 0.6, respectively. The n/m=1/2 EPM

was found to have a much higher amplitude than the n/m=2/4 GAE. The main objectives of this thesis are to reproduce these experimentally observed modes and numerically clarify the EP-SAW interaction in Heliotron J. This also includes the calculation of the EP transport in Heliotron J.

This thesis consists of seven chapters.

In chapter 1, the criteria for achieving the continuous self-sustainable fusion plasma are discussed. The importance of the EP confinement and the suppression of the EP-driven MHD instabilities in the magnetic confinement fusion device are introduced. The experimental reports of the EP-driven MHD instabilities and their impacts on the EP transports are reviewed to emphasize the importance of the mitigation and suppression of EP-driven MHD instabilities. In the last part, the interaction of the EP-SAW and SAW-SAW interactions in the stellarator and heliotron configurations are summarized.

In chapter 2, the basic physics of EP-driven MHD instability in the toroidal magnetic confinement fusion device are summarized. In the first section of this chapter, the fundamental plasma descriptions are discussed. It is followed by the description of Alfvén eigenmode and energetic particle mode. In the last section, the interactions between EP and shear Alfvén wave are summarized.

In chapter 3, the properties of the Heliotron J magnetic field are presented. These include (1) low magnetic shear, (2) vacuum magnetic well, and (3) the role of the bumpy component. The neutral beam injection (NBI) system of Heliotron J and the properties of NBI-generated EPs are summarized. The EP energy distribution measured with a charge exchange neutral particle analyzer (CX-NPA) has a bump-on-tail structure. This will be used as the basis for the MEGA simulation in chapters 5 and 6. Lastly, the experimentally observed EP-driven MHD instabilities are summarized and compared with the calculated shear Alfvén continua by STELLGAP.

In chapter 4, the MEGA code is summarized. These include the single-fluid MHD equations coupled with the EP current density and the EP drift kinetic equations. The limitation and imposed assumptions of MEGA are presented.

In chapter 5, the EP-driven MHD modes were simulated in the currentless equilibrium. The n/m=2/4 GAE was reproduced as the dominant mode; however, the weak n/m=1/2 GAE was destabilized instead of the n/m=1/2 EPM. This contradicts the experiment in terms of the relative stability between the n/m=1/2 and 2/4 modes. The bump-on-tail and slowing-down EP velocity distributions were considered. The bump-on-tail case represents the experimentally observed EP energy distribution, while the slowing-down case represents the ideal scenario where $\tau_{cx} << \tau_{sd}$, where τ_{cx} and τ_{sd} are the charge-exchange time and the slowing-down time, respectively. The calculation results showed no significant difference in the linear growth rates between these two distributions. For the bump-on-tail case, the majority of the EP-drive is due to the high-velocity toroidicity-induced resonance. The helicity-induced resonances are much weaker because they are localized in the low-velocity region. These helicity-induced resonances are more significant in the slowing-down distribution. The differences in the initial EP distribution also cause differences in the redistributed EP pressure profile. The hollow (flat) EP pressure profile is formed after the saturation of the EP-driven MHD modes in the bump-on-tail (slowing-down) distribution. This is caused by the convective transport of the high velocity resonant co-passing EPs. These high velocity resonant co-passing EPs transit the core region during the linear phase; therefore, their transports significantly cause a finite reduction in the core region.

In chapter 6, the discrepancy between the simulation and experiment was tackled by introducing the free boundary simulation. Due to the low magnetic shear, any low-n MHD instabilities can potentially cause finite plasma displacement at the last closed flux surface (LCFS). The experimentally observed n/m=1/2 EPM and n/m=2/4 GAE were successfully reproduced by MEGA with the free boundary simulation. The effects on the MHD part of the equations are weak but stronger for the kinetic part (EP-SAW interaction). In the free boundary simulation, the spatial profiles of the n/m=1/2 and n/m=2/4 modes are broadened and shifted radially outward. This enhances the EP-SAW interaction when the EP spatial gradient is finite in the edge region, and thus the linear growth rates of both the n/m=1/2 EPM and the n/m=2/4 GAE increase. From the kinetic analysis of the resonant EPs, the EP-SAW interactions are intense in the plasma edge region. The major contribution is from the high velocity co-passing resonant EPs that transit the core region. These resonant EPs have sufficiently large orbit widths such that they can effectively interact with the n/m=1/2 EPM at the plasma edge. It was also shown that the linear growth rate of the n/m=1/2 mode is significantly underestimated in the fixed boundary simulation. The n/m=1/2 EPM at the plasma edge cannot be destabilized in the fixed boundary simulation even if the initial EP pressure is doubled.

Chapter 7 is devoted to the conclusion. The findings and the simulation results are summarized. The prospective research topics and the extensions of this study are also presented.

The main achievements of the presented thesis are as follows:

- The EP-driven MHD instabilities in Heliotron J, a low magnetic shear helical-axis heliotron has been successfully reproduced with MEGA, an EP-MHD hybrid simulation code. This is the first time that MEGA code has been experimentally validated in the helical-axis heliotron and stellarator configurations.

- The importance of the boundary condition on the simulation of the EP-driven MHD instability in Heliotron J has been revealed. The results also reflect the invalidity of the fixed boundary assumption in the simulation of the EP-driven MHD in Heliotron J.

- The roles of EP in each particular phase space region were clarified in Heliotron J. This information also allows us to understand the AE-induced EP transport in Heliotron J.

These achievements are beneficial for the study of the EP-driven MHD instability in Heliotron J. The validity of the free boundary condition can potentially be applied to other advanced helical-axis stellarator and heliotron configurations with low magnetic shear. It can also be extended to the stellarator/heliotron optimization and the alpha channeling through toroidal asymmetric resonance.

Contents

Chapter 1

Introduction

1.1 Background

Indispensably, mankind harnesses energy from the nature to perform daily activities. The earliest utilization of fire by prehistoric humans can be traced back since 1.5 million years ago[1]. It was used for hunting, defense, cooking, source of warmth, light source, and etc. With the accumulated knowledge and experiences through time, mankind started to utilize energy in more complex manners: copper metallurgy ($\sim$ 5000 BC.), steam engine (1760-1840), electricity (1870-1914), and etc. To account for the increasing demand, the main energy sources shifted from low energy density and inefficient energy sources (e.g. firewood) to higher one (e.g. coal, oil and natural gas). Since the 1$^{\text{st}}$ and 2$^{\text{nd}}$ industrial revolutions, the global energy consumption continuously increased, and inevitably led to the increase in the greenhouse gas emission (e.g. CO_2). The history of the global primary energy consumption and CO_2 emission are shown in figures 1.1 and 1.2, respectively[2, 3, 4]. These gradually raise the concern on the environmental issues and the depletion of the global fossil fuel supply. As a countermeasure, renewable energy such as wind power and solar energy were purposed. However, their issues on intermittency and energy density have not yet been resolved. Nuclear energy is the feasible alternative for the clean energy source. The first demonstration of the possibility of electricity generation by nuclear fission energy started in 1942 when Enrico Fermi successfully created the first self-sustainable nuclear fusion reactor. Number of nuclear fission power plant rapidly emerged between 1970 and 1985 due to the significant increase of the petroleum price. However the credibility of the nuclear energy was damaged by the reactor meltdown event in Three Miles Island, Pennsylvania in 1979 and the Chernobyl catastrophe in 1986. Since then the growth of the nuclear energy (fission) power plant and the development of the nuclear fission technology were halted. These histories suggest that the suitable energy source and technology must satisfies 4 criteria:

1. The fuel supply should be sufficient, sustainable, and high in energy density.
2. Electricity generation must be continuous.
3. The CO_2 emission and hazardous wastes should be minimized.
4. The possibility of major catastrophic event should be minimized.

One of the potential candidate that is capable to satisfy these criteria is nuclear fusion energy.

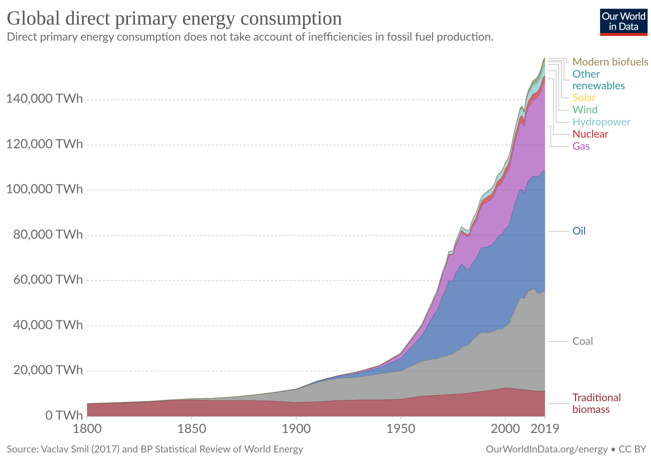

Figure 1.1: The global primary energy consumption from 1800-2019.

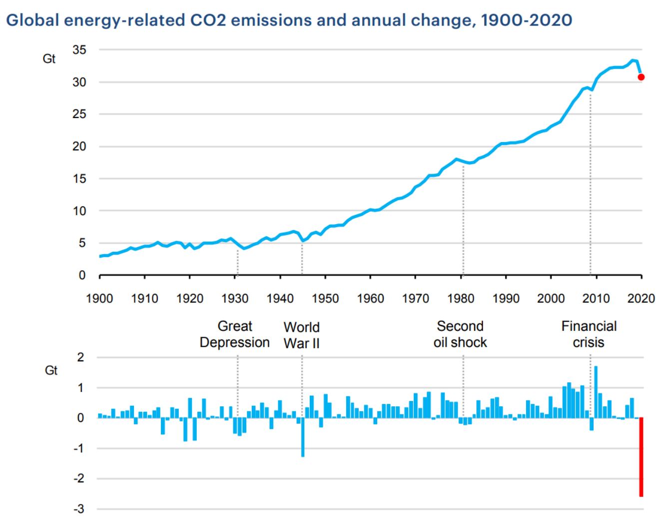

Figure 1.2: The global energy-related CO_2 emissions and annual change from 1900-2020.

Nuclear fusion is a nuclear reaction in which 2 or more nuclei fuse into heavier nuclei by a strong nuclear force. If the products of the nuclear fusion reaction have lower potential energy than the summation of their former nuclei, the energy deficit is released ($E = mc^2$). This is true for the fusing of the light nuclei (See the nuclear binding energy with respect to the atomic number shown in figure 1.3). The fuels for nuclear fusion reactions are the light elements, mainly hydrogen. The nuclear fusion reaction naturally occurs in the sun which is the primary energy source of our solar system. In the sun, the temperature is so high such that the hydrogen atoms are in the plasma state. These high energy hydrogen nuclei must be confined sufficiently long until the nuclear fusion reaction occur. These high temperature plasmas are confined by mean of the massive gravitational force of the sun; therefore, it is not feasible to apply the similar approach to the nuclear fusion reaction on the earth.

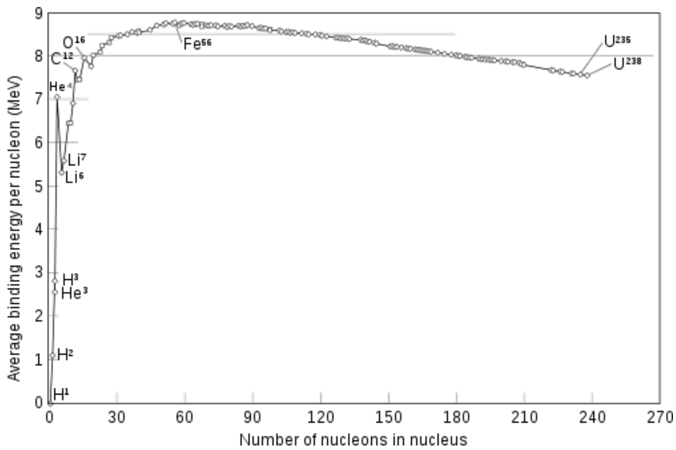

Figure 1.3: The nuclear binding energy with respect to the atomic number.

Magnetic confinement fusion is one of the approach to confine the high temperature plasmas on the earth. In the magnetic confinement, high energy plasma is confined inside a closed magnetic field by the Lorentz force. In this concept, both toroidal and poloidal magnetic fields are requisite to average out resulted $\vec{E} \times \vec{B}$ drift from the ∇B drift of ion and electron. Tokamak and stellarator/heliotron are the two main concepts for producing poloidal magnetic field. In tokamak, central solenoid is utilized to induce toroidal plasma current. Poloidal magnetic field is created by this induced toroidal plasma current. For stellarator/heliotron[5], both toroidal and poloidal magnetic fields are generated by either continuously helical magnetic coils or modular coils. The most feasible nuclear fusion reaction on the earth is deuterium (D) and tritium (T) fusion reaction (eq.1.1). The D-T reaction is selected because it has a high efficiency in term of the reaction rate. Secondly, the potential fuel supplies are near limitless. Deuterium can be extracted from seawater, while tritium can be obtained from lithium (Li) (eq.1.2).

$$D + T \rightarrow He^4(3.5MeV) + n(14.1MeV) \tag{1.1}$$

$$Li^6 + n \rightarrow T + He^4(4.8MeV) \tag{1.2}$$

$$Li^7 + n \rightarrow T + He^4 + n(-2.5MeV) \tag{1.3}$$

The magnetic confinement fusion concept was revealed to the public at the 2nd United Nations Conference on the Peaceful Uses of Atomic Energy in 1958. In the following years, it was founded that several instabilities can evolve in the magnetically confined plasma. These instabilities cause additional particle and energy transports and even disrupt the confinement. Tokamak, a toroidally symmetric magnetic confinement fusion, emerged as the mainstream of the thermonuclear fusion research after the international thermonuclear fusion conference in 1968 in Novosibirsk. In this meeting, T-3 tokamak successfully achieved the electron temperature of 1.00 keV. After that several new tokamaks were designed and operated: Joint European Torus (JET), Japan Torus-60 Upgrade (JT-60U), DIII-D, Experimental Advanced Superconducting Tokamak (EAST), K-STAR, and etc. Yet none of these tokamaks has achieved the break-even point. The current world record of the ratio of output power to input power (Q value) is 0.67 by JET in 1997. To surpass the break-even point, International thermonuclear experimental reactor (ITER) project, the world's largest toroidal magnetic confinement fusion device, is initiated. It is currently under construction in France. The first plasma is planned to initiate in December 2025. The goals of ITER are:

1. Achieve a self-sustainable deuterium-tritium fusion plasma by the released energy from nuclear fusion reaction.

2. Achieve 500 MW of fusion power for 400 s.

3. Testing the integrated plasma controlled and diagnostic systems in the fusion plasma condition.

4. Verifying the tritium breeding blanket.

5. Demonstrate the safety of the nuclear fusion reactor, reliability, and minuscule impact to the environment.

To achieve the first objective, the thermonuclear fusion condition must be maintained for the bulk plasma, and the D-T fusion-born energetic alpha particles (EPs) must be confined sufficiently long until they are thermalized with the bulk plasma. However, the magnetically confined fusion plasma is not in the thermodynamic equilibrium; therefore, several driving forces exist. As a result, several macro (MHD) and micro (turbulence) instabilities can be destabilized. These instabilities worsen the confinement by increasing the particle and energy transports of the bulk plasma and the energetic particles. Some of the major macro-instabilities (MHD) are the current-driven MHD instability, pressure-driven MHD instability, and energetic particle (EP) driven MHD instability. All of these 3 MHD instabilities exist in the tokamak configuration; however, current-driven MHD instability can be mitigated in the stellarator/heliotron configuration since the toroidal plasma current is not required to generate the poloidal magnetic field. The pressure-driven MHD instability can also be mitigated if the vacuum magnetic well exists throughout the confinement region[6, 7]. For the EP-driven MHD instability, it cannot be easily mitigated since the driving force is the fusion-born EPs that are necessary to maintain the self-sustainable fusion plasma. It is the major impediment of confining EPs.

EP-driven MHD instability is mainly destabilized shear Alfvén wave (SAW) by EPs. These high-energy particles can interact with the SAW through the fundamental and sideband resonances during the slowing-down process. These instabilities can increase the EP transport via the $\vec{E} \times \vec{B}$ drift and the perturbed magnetic field ($\delta\vec{B}$) of SAW. Lost EPs can potentially damage the first wall and the plasma-facing components (PFCs), and reducing the alpha particle heating efficiency. In other words, the D-T fusion-born EPs must be confined sufficiently long; however, these EPs can cause instability. The numerical investigation of EP-driven MHD instability will be investigated in this thesis.

1.2 Previous Study of EP-driven MHD instabilities

Various types of EP-driven MHD instabilities were reported. They are classified into the eigenmode of the bulk plasma and the energetic-particle mode (EPM). The first type, an eigenmode, is a weakly damped wave because the continuum damping is minimized within the frequency gaps in the continuous spectrum. The second type, an EPM, can exist within the shear Alfvén continuum with strong continuum damping. EPM can be destabilized when the EP pressure is comparable to the bulk plasma pressure. EPM is not an eigenmode of the bulk plasma. The frequency of the EPM strongly depends on the EP resonance and EP distribution function.

The electrical field and the perturbed magnetic field caused by these instabilities can cause significant EP transport. The growth of the EP-driven MHD mode correlates with the loss of EPs where the loss of EPs is measured with the reduction in the neutron diagnostics[8], lost ion probe[9, 10, 11], and the fast ion D-alpha. (FIDA) density[12]. The effect of the EP-driven MHD instabilities on the EP confinement is shown in figure 1.4. In this figure, the Alfvénic activities of the RSAE and TAE in the DIII-D plasma with the reversed q-profile are shown in panel (a). Panels (b) and (c) show their impacts on the EP density profile[13]. Panels (b) and (c) show the stiffness of the EP density profile where the further increment in NBI power does not cause a change in the EP density profile.

The behavior of the EP-driven MHD mode and the EP-SAW interaction are different between tokamak and stellarator/heliotron configurations. In the stellarator/heliotron configuration, the equilibrium magnetic field Fourier components are composed not only the toroidally symmetric components ($\nu_B = 0$) but also the toroidally asymmetric components ($\nu_B \neq 0$), such as helicity ($\mu_B/\nu_B = 1/1$) and bumpy ($\mu_B/\nu_B = 0/1$) components. These additional magnetic Fourier components cause change in the EP-SAW and SAW-SAW interactions. For the EP-SAW interaction, more EP-SAW energy channels exist. The EPs in stellarator/heliotron magnetic configuration can resonate not only with the toroidicity-induced resonance but also other toroidally asymmetric-induced resonances, such as the helicity-induced resonance[14, 15]. These additional resonances can potentially increase the linear growth rate (γ/ω_A) of the EP-driven MHD mode; however, it can also be compensated by the thermal ion Landau damping if these additional resonances exist in the low velocity region[16]. For the interaction between shear Alfvén waves (SAW-SAW), more shear Alfvén continuum (SAC) gaps are formed, such as the HAEs[17, 18] and the mirror-induced Alfvén eigenmode (MAE). The SAC gap width can also be reduced and even annihilated at a certain rational surface[15]. Both the toroidal asymmetric-induced eigenmodes and the reduction of the SAC gap width can be significant in the high magnetic shear stellarator/heliotron with the small number of toroidal field periods.

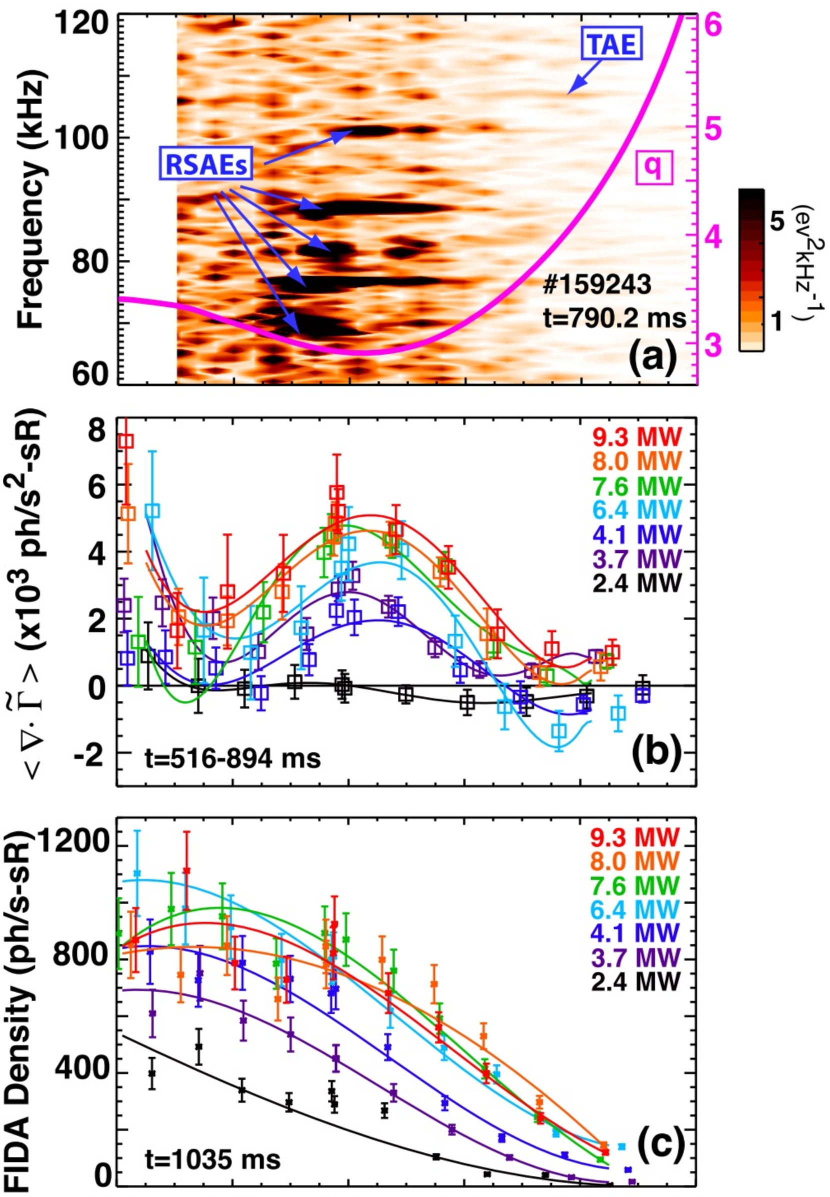

Figure 1.4: The Alfvénic activities and its effect of the EP confinement measured with the electron cyclotron emission (ECE) and fast-ion deuterium alpha (FIDA) diagnostics from the DIII-D discharge with the reversed q-profile[13]. (a) Radial profile and the frequency of the ECE power spectra at t=790.2 ms. (b) The radial profile of the averaged EP flux. (c) The comparison of the FIDA density profiles at t = 1035 ms between different beam power.

1.3 Research Motivations and Objectives

The low magnetic shear stellarator/heliotron configuration is currently one of the main concepts in the design of the modern optimized stellarator/heliotron configuration. In this concept, the radial variation of the local rotational transform value ($\iota/2\pi$) is negligible; therefore, the formation of the coupling-type shear Alfvén gap is unlikely. The most commonly observed EP-driven MHD instabilities in the low magnetic shear stellarator/heliotron are GAE, non-conventional GAE (NGAE), and EPM. The deterioration of the plasma confinement by the low order magnetic islands can also be mitigated; however, the Pfirsch-Schlüter and bootstrap current should be minimized in the high plasma beta MHD equilibrium. The low magnetic shear concept has been applied in Heliotron J[19], TJ-II, Wendelstein 7-X (W-7x)[20], and recently in China First Quasi-Axisymmetric Stellarator (CFQS)[21].

The EP-driven MHD instability[22, 23, 24, 25, 26] and the EP dynamic[27, 28, 29, 11] in Heliotron J have been mainly investigated with the experimental approach. These studies have already identified the types of the observed EP-driven MHD modes (EPM and GAE), and their effects on the EP transport. Recently, the stabilization of the EP-driven MHD mode by electron cyclotron resonance heating (ECRH) and electron cyclotron current drive (ECCD) was focused. The prospective suppression mechanism for the ECRH is the change in the collisional damping rate of the trapped electron[30, 25]. For the ECCD, the EP-driven MHD mode is suppressed in Heliotron J by the increase in the local magnetic shear. The stabilization by the increase in magnetic shear has also been reproduced by FAR-3D simulation, a Landau closure model[31]. However, the interaction between the EPs and the EP-driven MHD modes (EPM and GAE) has not yet been clarified. The clarification of these interactions can provide information on the role of each existing EP-SAW energy channel in Heliotron J. This information also links to the AE-induced transport behavior and the resulted EP pressure profile. In addition, the control of the EP-driven MHD instability by ECCD can also alter the EP-SAW resonance condition through the change in the rotational transform profile. The EP-SAW and SAW-SAW interactions in Heliotron J will be analyzed in this thesis.

Computer simulation is a powerful tool to investigate the EP-SAW and SAW-SAW interactions in the 3-dimensional plasma. Several simulation codes have been developed for these purposes: MEGA[32, 33, 34] (full-MHD hybrid simulation model), EUTERPE[35], and GTC[36] (gyrokinetic PIC code), NIMROD[37, 38] (a finite element hybrid MHD code), and FAR3D[39, 31] (a reduced-MHD equation with Landau closure model for energetic particle). They have already been utilized in both tokamak and stellarator/heliotron configurations. MEGA, a hybrid EP-MHD simulation code, is used to analyze the linear and nonlinear dynamics of the EP-driven MHD instabilities. MEGA employs a cylindrical coordinate for the bulk plasma; therefore, it does not restrict to the nested flux surface assumption. This code has been successfully validated to the DIII-D[40], JT-60U[41], and LHD[33, 42] experimental results. All of these devices are planar axis devices. It has not yet been applied to the helical-axis and low magnetic shear stellarator/heliotron configuration. Previously, the EP-driven MHD modes in Heliotron J during the linear growth phase were simulated by FAR3D, a Landau-closure model[31]; however, inconsistencies between the experiment and simulation were found. The major inconsistency is the amplitude of the $n/m = 1/2$ EPM and $n/m = 2/4$ GAE. In the experiment, the $n/m = 1/2$ EPM has a much higher amplitude than the $n/m = 2/4$ GAE; however, the $n/m = 2/4$ GAE was found to be more unstable than the $n/m = 1/2$ EPM in the FAR3D simulation. These inconsistencies need to be resolved with a more realistic model. One of the potential causes is the boundary condition. Normally, the internal mode like AE is simulated with the fixed boundary condition, where plasma is surrounded by the perfectly conducting wall. However, this assumption can have a stronger effect on the low-n MHD mode.[43, 44] due to larger mode width. The validity of this assumption can be worsened in Heliotron J due to its low magnetic shear. Therefore, the EP-driven MHD mode in Heliotron J can cause a finite plasma displacement at the LCFS even if the mode is localized in the middle of plasma ($r/a \approx 0.50$).

Since the current mainstream of the optimized stellarator/heliotron has a helical magnetic axis and also low magnetic shear, the success in the experimental validation provides the opportunity to reproduce the experimental observations and clarify the EP-SAW and SAW-SAW interactions in another low magnetic shear stellarator/heliotrons (e.g. W7-X and CFQS). This study will also equips us with the validity of the assumption and the simulation setup for the low magnetic shear stellarator/heliotron.

The objectives of this thesis are listed as follows:

1. To reproduce the experimentally observed EP-driven MHD mode in Heliotron J, a low shear helical-axis heliotron.

2. To analyze the role of the bulk plasma boundary condition on the modeling of the EP-driven MHD mode in Heliotron J.

3. To clarify the interaction between EP and shear Alfvén wave in Heliotron J.

4. To calculate the AE-induced EP transport in Heliotron J.

1.4 Thesis Framework

This thesis is organized as follows:

- Chapter 2 summarizes the basic physics of the EP-driven MHD instability in a toroidal magnetic confinement fusion device. This includes the plasma description, MHD wave, Alfvén eigenmode, EP-SAW interaction, and EP transport by instability.

- Chapter 3 provides a brief summary of Heliotron J. The parameters of the neutral beam injection (NBI) system in Heliotron J are presented along with the energy spectra of the EP energy distribution measured with CX-NPA. Lastly, the experimentally observed EP-driven MHD modes in Heliotron J are discussed.

- Chapter 4 describes a brief summary of the plasma simulation code for the EP-driven MHD instability simulation. The model utilized in the MEGA code will be presented.

- Chapter 5 shows the simulated EP-driven MHD modes in Heliotron J with MEGA. The EP redistributions in velocity and real spaces are discussed. The dependency of the mode properties on the initial EP velocity distribution is discussed. The discrepancies between the simulation results are also reported.

- Chapter 6 analyzes the role of the boundary condition on the modeling of the EP-driven MHD mode in Heliotron J. The discrepancy between the simulation and the experiment is resolved in this section. The interaction between the $n/m = 1/2$ EPM and the resonant EPs is analyzed.

- Chapter 7 is devoted to summary.

Chapter 2

Energetic Particle Driven Magneto-hydrodynamics Instabilities

The basic physics of the energetic particle (EP) driven MHD instability are discussed in this section. In section 2.1, the basic of plasma models are described. It starts from the kinetic description of the plasma to the fluid model. In section 2.2, the physics of the shear Alfvén wave in a uniform plasma are summarized. In section 2.3, the differences between the shear Alfvén gap mode and the energetic particle mode are introduced. In the last section, the interaction between energetic particle and shear Alfvén wave in tokamak and heliotron/stellarator configurations is discussed.

2.1 Plasma Description

The most fundamental description of the plasma is the *Klimontovich* and *Liouville* equations (Eq.2.1). They include the motion of each particle and their interactions in the $6\hat{\text{t}}\text{h}$ dimensional configuration and velocity spaces $(\vec{r}, \vec{v})$. The *Klimontovich* equation describes the time evolution of the particle density, while the *Liouville* equation describes the time of the system density. Due to the zero convective derivative, the particle (or system) density is conserved along the particle orbit.

$$\frac{dN(\vec{r},\vec{v},t)}{dt} = \{\frac{\partial}{\partial t} + \vec{v}\cdot\frac{\partial}{\partial \vec{r}} + \frac{e}{m}(\vec{E} + (\vec{v}\times\vec{B})\cdot\frac{\partial}{\partial \vec{v}}\}N(\vec{r},\vec{v},t) = 0 \tag{2.1}$$

$$\tag{2.2}$$

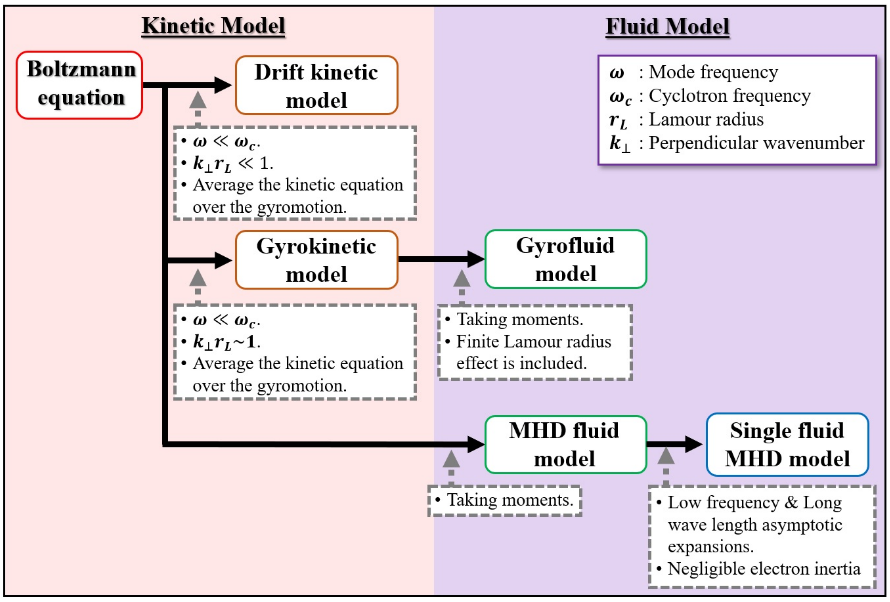

Figure 2.1: Summary of the plasma kinetic and fluid models.

The *Klimontovich* and *Liouville equation* contain a significant amount of information, and they are impractical to be solved. It can be simplified by performing an ensemble average over the large amount of the particles. This procedure introduces a *distribution function* $f(\vec{r}, \vec{v}, t)$. The *distribution function* $f(\vec{r}, \vec{v}, t)$ represents the number of particles within a phase space volume. The Boltzmann equation is obtained, where the LHS and RHS of eq.2.3 represent the collective behavior of the plasma and the collisional effects, respectively. If collision term is neglected (e.g. high temperature plasma), eq.(2.3) is called *Vlasov equation*.

$$\{\frac{\partial}{\partial t} + \vec{v} \cdot \frac{\partial}{\partial \vec{r}} + \frac{e}{m}(\vec{E} + (\vec{v} \times \vec{B}) \cdot \frac{\partial}{\partial \vec{v}}\} f(\vec{r}, \vec{v}, t) = (\frac{\partial f}{\partial t})_c \tag{2.3}$$

The plasma kinetic model (eq.2.3) can be further simplified by taking moments of the ion and electron distribution functions. The obtained results are called two fluid MHD equations. In the typical fusion plasma parameters, the length scale of the MHD mode is much longer than the Debye length, while the time scale of the MHD mode is much slower than the time scale of the plasma frequency. In this limit, the local charge imbalance between the ions and electrons can be neglected because electrons have sufficient time to follow ions. This allows us to assume the equivalent in the local ion and electron number densities ($n = n_i = n_e$). This condition is called the *quasi-neutrality condition*. Lastly, the displacement current in the Maxwell equation can also be neglected because of the quasi-neutrality condition (low frequency). By applying these approximations to the *two fluid MHD* *equations*, the contribution of the high-frequency and short-wavelength mode can be eliminated. The resulted equations are called *ideal MHD equations. Ideal MHD equations* are shown in Eqs.2.4-2.10.

$$\frac{\partial \rho}{\partial t} + \nabla \cdot (\rho \vec{v}) = 0 \tag{2.4}$$

$$\rho(\frac{\partial \vec{v}}{\partial t} + \vec{v} \cdot \nabla \vec{v}) = -\nabla P + \vec{J} \times \vec{B} \tag{2.5}$$

$$\frac{\partial P}{\partial t} + \vec{\cdot} \nabla P + \gamma P \nabla \cdot \vec{v} = 0 \tag{2.6}$$

$$\vec{E} + \vec{v} \times \vec{B} = 0 \tag{2.7}$$

$$\nabla \cdot \vec{B} = 0 \tag{2.8}$$

$$\nabla \times \vec{B} = \mu_0 \vec{J} \tag{2.9}$$

$$\frac{\partial \vec{B}}{\partial t} = -\nabla \times \vec{E} \tag{2.10}$$

- Continuity equation (Eq.2.4) implies mass conservation. In real experiment, source and loss terms, such as ionization, recombination, charge exchange, and diffusion can be incorporated at the right-hand-side (RHS) of the equation.

- Momentum equation (Eq.2.5) represents the 2 forces, which act on the plasmas: (1) pressure gradient and (2) electromagnetic force.

- Adiabatic equation (Eq.2.6) describes the time evolution of the plasma state with no heat loss. This is equivalent to the conservation of energy. Loss term, such as viscous loss, diffusion, and Ohmic heating can be introduced at the RHS of the equations.

- Generalized Ohms law is reduced to the form in Eq.2.7. Hall effect, electron diamagnetic effect and resistivity terms are neglected. Neglecting resistivity implies that the electric field parallel to the plasma current is zero.

- The last 3 equations (Eqs. 2.8-2.10) are the low-frequency approximation of the Maxwell equations. Eqs.2.8, 2.9, and 2.10 are the Gauss's law of magnetic field, Ampere circulation law, and Faraday's law of induction, respectively.

2.2 Magnetohydrodynamic wave

The low frequency waves described by the ideal MHD equations are (1) shear Alfvén wave, (2) fast magnetosonic wave, and (3) slow magnetosonic wave. The dispersion relation of these waves can be derived from the ideal MHD equations (Eqs.2.4-2.10) in an infinite homogeneous plasma with a uni-directional magnetic field. In this derivation, the magnetic field is represented by $\vec{B} = B_0\hat{k}$. To obtain the dispersion relation of these waves, the MHD plasma velocity ($\vec{v}_1$), density (ρ_1), pressure (p_1), electric field ($\vec{E}_1$) and magnetic field ($\vec{B}_1$) fluctuations are linearized. These field quantities are expanded to the first order as $x(\vec{r},t) = x_0(\vec{r}) + x(\vec{r},t)_1$ where the perturbed quantity is expressed by Eq.2.11. ω and $\vec{k}$ are angular mode frequency and angular wave number, respectively. The higher order terms (e.g. δx^2) are neglected. Due to the infinite homogeneous plasma assumption, the MHD equilibrium field quantities ($\vec{J}_0$, $\vec{v}_0$, $\vec{E}_0$, $\nabla\rho_0$, and ∇P_0) are zero. The linearized ideal MHD equations are shown in Eqs.2.12-2.18.

$$X_1(\vec{r},t) = Xexp[-i(\omega t - \vec{k}\cdot\vec{r})] \tag{2.11}$$

$$\frac{\partial\rho_1}{\partial t} + \rho_0\nabla\cdot\vec{v}_1 = 0 \tag{2.12}$$

$$\rho_0\frac{\partial\vec{v}_1}{\partial t} = -\nabla P_1 + \vec{J}_1\times\vec{B}_0 \tag{2.13}$$

$$\frac{\partial P_1}{\partial t} + \gamma P_0\nabla\cdot\vec{v}_1 = 0 \tag{2.14}$$

$$\vec{E}_1 + \vec{v}_1\times\vec{B}_0 = 0 \tag{2.15}$$

$$\nabla\cdot\vec{B}_1 = 0 \tag{2.16}$$

$$\nabla\times\vec{B}_1 = \mu_0\vec{J}_1 \tag{2.17}$$

$$\frac{\partial \vec{B}_1}{\partial t} = -\nabla \times \vec{E}_1 = 0 \tag{2.18}$$

This expression is substituted into the linearized continuity (Eq.2.12), energy (Eq.2.14), Ampere Circulation's Law (Eq.2.17), and Faraday's law (Eq.2.18). The substituted linear equations are shown in Eqs.2.19-2.22.

$$\omega\rho_1 = \rho_0(\vec{k}\cdot\vec{v}_1) \tag{2.19}$$

$$\omega P_1 = \gamma P_0(\vec{k}\cdot\vec{v}_1) \tag{2.20}$$

$$\omega\vec{B}_1 = -\vec{k}\times(\vec{v}_1\times\vec{B}_0) \tag{2.21}$$

$$\omega\mu_0\vec{J}_1 = -i\vec{k}\times[\vec{k}\times(\vec{v}_1\times\vec{B}_0)] \tag{2.22}$$

By eliminating ρ_1, P_1, $\vec{B}_1$, and $\vec{J}_1$ terms from the linearized momentum equation (Eq.2.5) with the expressions given in Eqs.2.19-2.22. The set of the linear equations with three velocity vector components are obtained (Eq.2.23).

$$\begin{gathered}(\omega^2 - k_\parallel^2 V_A^2)v_{1x} = 0\\ (\omega^2 - k_\perp^2 V_S^2 - k^2 V_A^2)v_{1y} - (k_\perp k_\parallel V_S^2)v_{1z}) = 0\\ -(k_\perp k_\parallel V_S^2)v_{1y} + (\omega^2 - k_\parallel^2 V_S^2)v_{1z} = 0\end{gathered} \tag{2.23}$$

By setting the determinant of the system of linear equations (Eq.2.23) to zero, three branches of the dispersion relation of the ideal MHD waves are obtained (Eq.2.24-2.25). Eq.2.24 is the dispersion relation for the shear Alfvén wave, while Eq.2.25 is the dispersion relation for the fast and slow magnetosonic waves. It is clear both the dispersion relations shown in Eqs.2.24-2.25 have a purely oscillation solution since the imaginary part of ω is zero. For Eq.2.25, α^2 term only exists within the $0 \geq \alpha^2 \geq 1$.

$$\omega^2 = k_\parallel^2 V_A^2 \tag{2.24}$$

$$\begin{gathered}\omega^2 = \tfrac{1}{2}k^2(V_A^2 + V_S^2)[1 \pm (1-\alpha^2)^{1/2}]\\ \alpha^2 = 4\tfrac{k_\parallel^2}{k^2}\tfrac{V_S^2 V_A^2}{(V_S^2+V_A^2)^2}\end{gathered} \tag{2.25}$$

Shear Alfvén wave (SAW) is a low frequency transverse electromagnetic wave (Eq.2.24). This wave propagates parallel to the magnetic field. According to Eq.2.23, $\vec{B}_1$ and $\vec{v}_1$ are both perpendicular to the equilibrium magnetic field (also $\vec{k}$). Lastly, the SAW is incompressible ($\nabla \cdot \vec{v}_1 = 0$). The restoring force of this wave is the magnetic tension due to the perturbation part of the perpendicular magnetic field. Differ from the SAW, the fast and slow magnetosonic waves are the compressible waves ($\nabla \cdot \vec{v}_1 \neq 0$). The fast and slow magnetosonic waves are differentiated by the plus and minus signs in Eq.2.25, respectively. The major difference between the fast and slow magnetoacoustic waves is the compression characteristics. The compression by the fast magnetoacoustic wave is mainly due to the magnetic field. In contrast, the compression caused by the slow magnetoacoustic wave is primarily due to the plasma compression.

2.3 Alfvén Eigenmode & Energetic Particle Mode

In the context of EP-driven MHD instability, the most common EP-driven MHD instability is the SAW that is driven unstable by resonant EPs. This instability can be observed in the magnetic confinement fusion plasma with energetic species (e.g. neutral beam injected particle and fusion-born alpha particle). In the toroidally magnetic confinement device, these EPs can resonate with the shear Alfvén wave through the fundamental and sideband resonances. The destabilization of the EP-driven MHD instability can enhance the EP transport which can reduce the EP heating efficiency. The transported EP can also damage the plasma-facing components. In the toroidally magnetic confinement fusion device, the periodicity constraints in the toroidal and poloidal directions limit the parallel wavenumber in the toroidal and poloidal directions to integers ("m" and "n" are for poloidal and toroidal mode numbers, respectively). To account for the poloidal and toroidal rotations of the magnetic field, the parallel wavenumber ($k_{\parallel}$) is represented by $(n - m\iota)/R$, where ι is a local rotational transform value. Any waves that follow the SAW dispersion relation (Eq.2.24) belong to the shear Alfvén continua.

In the magnetic confinement fusion plasma, there are radial variations in the rotational transform ($\iota/2\pi$), bulk plasma density (ρ_0), and magnetic field. This leads to the radial variation in the shear Alfvén continuum (SAC). The shear Alfvén wave at a different radial location has different phase velocities; therefore, the wave structure is dispersed and damped by this process. This damping is called continuum damping. Continuum damping is proportional to the radial derivative of the shear Alfvén continuum ($\gamma_d \propto d\omega/dr$). In the normal circumstance, the continuum damping rate exceeds the EP-driving rate ($\gamma_d > \gamma_h$). From this information, the destabilization of EP-driven MHD instability is possible if the shear

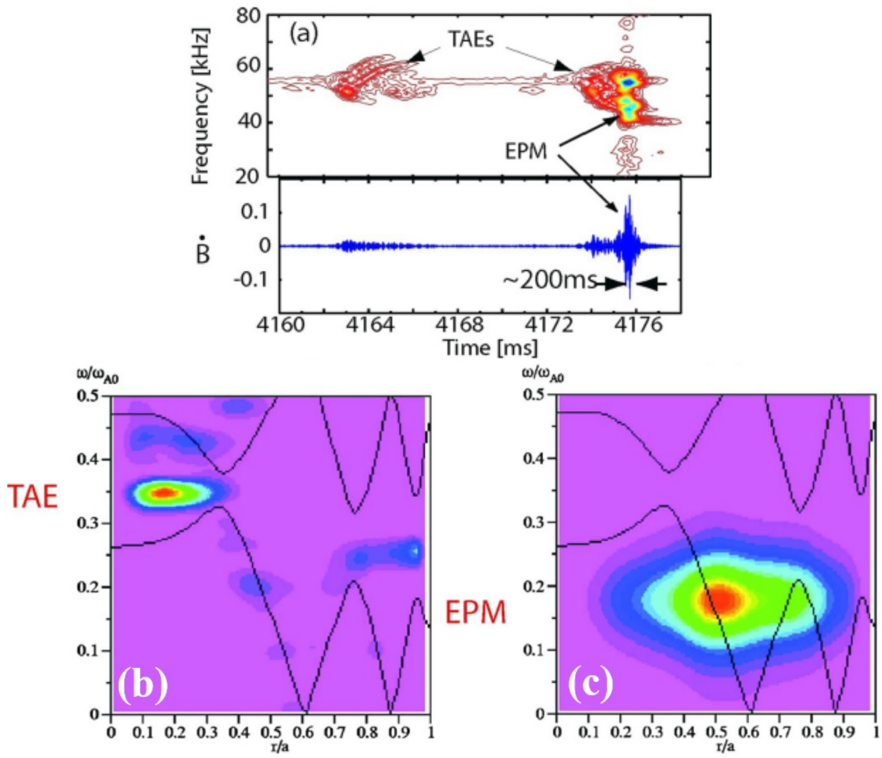

Figure 2.2: The simulation of the Alfvénic activity in the JT-60U beam injected discharge. Panel (a) shows the measured magnetic fluctuation that indicate the burst of the Alfvénic mode. Panels (b) and (c) show the simulation results of the EPM and TAE, respectively. The $n = 1$ shear Alfvén continua is plotted by the black solid line[45].

Alfvén continuum damping is minimized. The minimization of the continuum damping occurs within the shear Alfvén gap. It will be discussed in subsection 2.3.1. In addition to the shear Alfvén gap mode, the EP-driven MHD instability can also be excited in the region with finite continuum damping if the EP driving rate exceeds the continuum damping rate ($\gamma_h > \gamma_d$). This type of EP-driven MHD instability is called energetic particle mode (EPM)[46]. Differ from the shear Alfvén gap mode, EPM is not an eigenmode of the MHD plasma. Instead, it has a distinctive dispersion relation. This will be discussed in subsection 2.3.2. The example of the shear Alfvén gap mode (toroidal Alfvén eigenmode) and energetic-particle mode (EPM) is shown in figure 2.2. This figure shows the magnetic fluctuation caused by toroidal Alfvén eigenmode (TAE) and energetic-particle mode (EPM) in the JT-60U discharge[45]. In this discharge, the TAE and EPM frequencies are approximately 57.5 kHz and 45 kHz, respectively. The simulation results calculated by HMGC, the hybrid MHD gyro-kinetic code of this discharge are shown in panels (b) and (c). In panel (b), the TAE is located within the shear Alfvén continuum gap produced by the toroidal coupling, while the EPM lies in the shear Alfvén continuum.

2.3.1 Gap Mode

The minimization of the continuum damping exists within the SAC gap where $d\omega/dr \approx 0$. The destabilized EP-driven MHD mode within the SAC gap is also called as shear Alfvén gap mode. The shear Alfvén gap mode is the eigenmode of the MHD plasma (weakly damped wave). The SAC gap can cause by (1) the radial variation of the rotational transform profile, bulk plasma density, and magnetic field, and (2) the destructive interference between co-propagating and counter-propagating waves due to the periodic modulations in the shear Alfvén velocity through the toroidicity, ellipticity, and helicity of the equilibrium magnetic field. The former and the latter types are called coupling-type gap mode and extremum-type gap mode, respectively. The examples of the coupling-type gap mode are toroidicity-induced Alfvén eigenmode (TAE)[32, 47], ellipticity-induced Alfvén eigenmode (EAE), and helicity-induced Alfvén eigenmode (HAE)[48, 17, 49]. The examples of the extremum-type gap mode are the global Alfvén eigenmode (GAE) and reversed shear Alfvén eigenmode (RSAE). Some of the examples of the shear Alfvén gap modes are listed in Table 2.1.

Coupling Type Gap

Shear Alfvén can be induced by coupling between co- and counter-propagating waves. This coupling results from the periodic variation of shear Alfvén velocity along the magnetic field line. In the case of toroidal geometry, one revolution of the magnetic field line in poloidal direction experiences variation of magnetic field strength from high field side and low field side. In the toroidally asymmetric device (e.g. heliotron and stellarator), both toroidal and poloidal couplings exist. The destructive interference at the frequency crossing point between co- and counter-propagating waves with different poloidal and toroidal mode numbers are described by Eqs.2.26-2.27, respectively. At the frequency crossing point, ω_+ and ω_- are equal at the same radial location. In Eqs.2.26 and 2.27, n, m, ι, ν_B, μ_B, and N_{fp} are poloidal mode number, toroidal mode number, local rotational transform value, toroidal Fourier component of the magnetic field, poloidal Fourier component of the magnetic field, and number of equilibrium field period. By equating these two questions ($\omega_+ = \omega_-$), the required rotational transform value for the coupling of these two waves is obtained (Eq.2.28)[14, 50, 15]. For example, the toroidicity-induced shear Alfvén gap ($\mu_B/\nu_B = 1/0$) for the n/m mode will exists at the flux surface with $\iota = 2n/(2m+1)$. This suggests that the formation of the coupling type gap is more likely in the magnetic configuration with higher magnetic shear (high variation in the rotational transform in the radial direction). In figure 2.3, the rotational transform profiles of Heliotron J magnetic fields with and without counter-inductive current drive are shown. In the currentless equilibrium, Heliotron J magnetic field has a near zero magnetic shear. The difference in the variation in the magnetic shear has a strong influence of the shear Alfvén continua. The $N_f = +2$ shear Alfvén continua for the currentless and $I_p = -2.00$ kA MHD equilibria are shown in figures 2.4(a) and (b), respectively. In this figure, only the $n = 2$ shear Alfvén continua are labeled. It is apparent that the frequency crossings are apparent for the $I_p = -2.00$ kA. In figure 2.4(b), the $n/m = 2/4$ & 2/5 TAE gap, $n/m = 2/3$ & 2/5 EAE gap, $n/m = 2/3$ & 2/6 NAE gap, and $n/m = 2/2$ & 2/6 NAE gap are coupled at the flux surface with $\iota/2\pi$ of 0.444, 0.500, 0.444, and 0.500, respectively. These $\iota/2\pi$ values correspond to the $\iota/2\pi$ profile of the $I_p = -2.00kA$ shown in figure 2.3. The widths of the NAE gaps are narrower because the $\nu_B/\mu_B = 0/3$ and $\nu_B/\mu_B = 0/4$ Fourier components are infinitesimal when compared to the toroidicity ($\nu_B/\mu_B = 0/1$) and ellipticity ($\nu_B/\mu_B = 0/2$).

$$\omega_+ = \frac{n - m\iota}{R} v_A \tag{2.26}$$

$$\omega_- = -\frac{(n + \nu_B N_{fp}) - (m + \mu_B)\iota}{R} v_A \tag{2.27}$$

$$\iota = \frac{2n + \nu_B N_{fp}}{2m + \mu_B} \tag{2.28}$$

Extremum type gap

For the extremum type gap mode, the minimization of the continuum damping ($d\omega/dr \approx 0$) occurs due to the radial variation of the rotational transform value and MHD plasma density. The most common extremum type gap modes are global Alfvén eigenmode (GAE) and reversed-shear Alfvén eigenmode (RSAE). GAE is commonly observed in the low magnetic shear where the variation in the rotational transform is small; therefore, the formation of the coupling type gap mode is limited. Since extremum type gap mode does not require the coupling between two waves, the mode structure usually has a single toroidal and poloidal dominant harmonics.

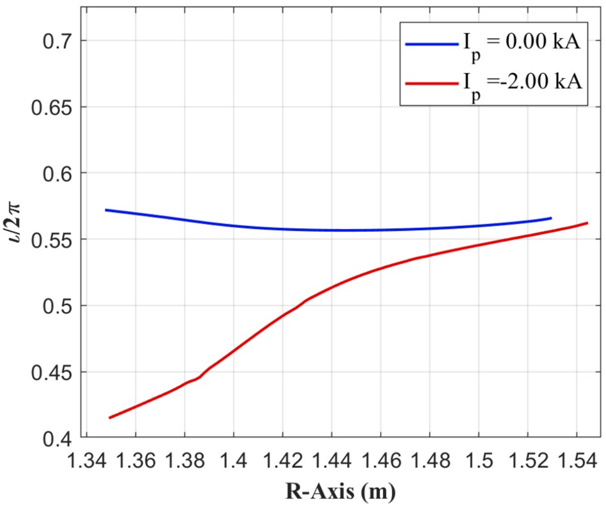

Figure 2.3: The comparison of the rotational transform ($\iota/2\pi$) profiles between the currentless and $I_p = -2.00$ kA MHD equilibria of Heliotron J.

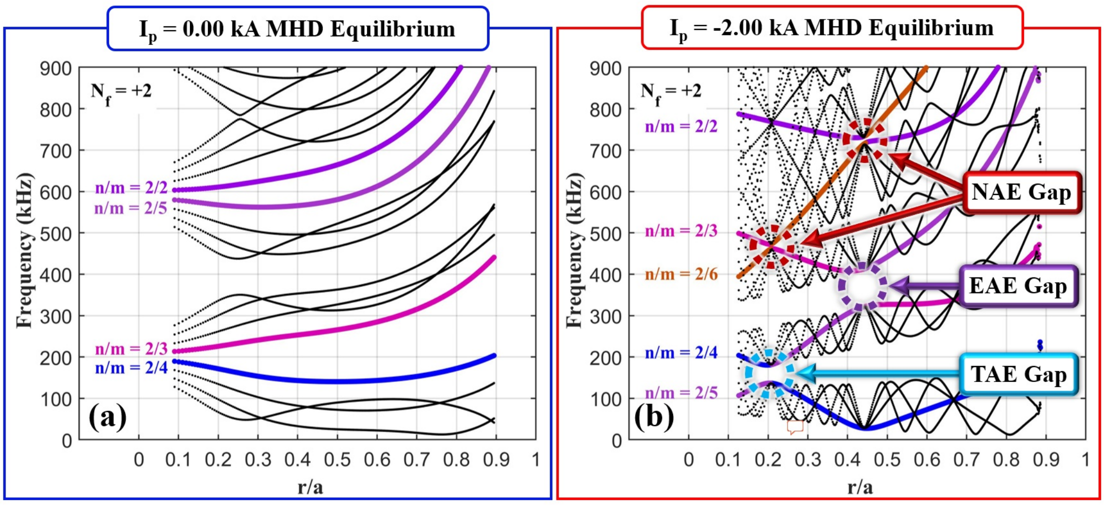

Figure 2.4: The comparison of the $N_f = +2$ shear Alfvén continua between the (a) currentless and (b) $I_p = -2.00$ kA MHD equilibria of Heliotron J.

2.3.2 Energetic Particle Mode (EPM)

From section 2.3, EPM is not an eigenmode of the MHD plasma. EPM can be destabilized in the region with finite continuum damping if the EP-driving rate is large. They are commonly observed in the plasma discharge with comparable EP pressure and bulk plasma pressure. The real frequency and the linear growth rate of the EPM strongly depend on the kinetic part of the EP distribution. In the experiment, EPM normally experiences strong frequency chirping during the nonlinear phase. This is due to a strong modification of the EP distribution by instability[51].

Name	Cause
Toroidicity-induced Alfvén eigenmode (TAE)	• Toroidicity (Coupling Type) • Poloidal coupling between "m" and "m+1."
Ellipticity-induced Alfvén eigenmode (EAE)	• Ellipticity (Coupling Type) • Poloidal coupling between "m" and "m+2."
Non-circularity-induced Alfvén eigenmode (NAE)	• Coupling Type Poloidal coupling between m and m + 3 and above.
Helicity-induced Alfvén eigenmode (HAE)	• Helicity (Coupling Type) • Coupling between two mode with different toroidal and poloidal mode numbers but belong to the same toroidal mode family.
Beta-induced Alfvén eigenmode (BAE)	• Compressibility (Coupling Type) • Upshift of continuum by acoustic wave coupling.
Global Alfvén eigenmode (GAE)	• Extremum type • Radial variation in the rotational transform profile and the density of MHD plasma.
Reversed-shear Alfvén eigenmode (RSAE)	• Extremum type • Exists at the extremum of the safe factor profile ($q = 1/\iota$).

Table 2.1: Brief summary of the shear Alfvén gap mode

2.4 Energetic Particle Dynamics and Interaction with Shear Alfvén Wave

2.4.1 Collisionless EP Guiding Center Drift Orbit

EP orbit does not localize on a single magnetic flux surface. Due to its high energy, the curvature drift and B drift of the EP can be sufficiently large. These two drifts cause EP to drift away from its initial flux surface. In addition, these guiding center drifts have a strong dependence on the EP velocity (square to the EP velocity). This drift is compensated by the rotational transform. There are many types of EP orbits (e.g. stagnation, potato, passing orbit, and trapped orbit). The most common types are the passing and trapped orbits. The guiding center orbits of the co-passing and counter-passing test particles with different kinetic energies are shown in figure 2.5. From this figure, all of the test particles are initially placed at R = 1.3 m and Z = 0.0 m. For the low velocity test particle (v_h/v_A = 0.10), the test particle is localized on the initial flux surface. As the velocity of the test particle increases, the deviation from the initial flux surface increases.

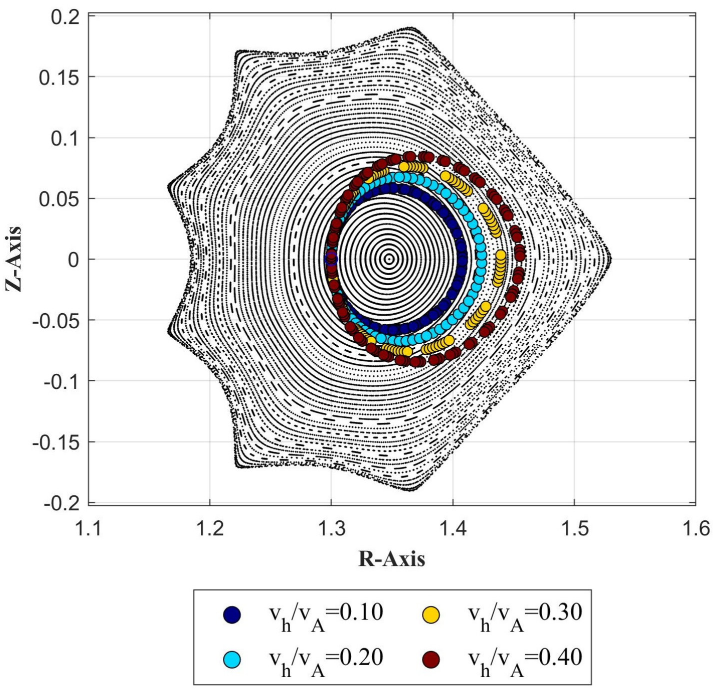

Figure 2.5: The orbits of the co-passing test particle in Heliotron J magnetic field. The test particles have velocities of $0.10v_{A0}$, $0.20v_{A0}$, $0.30v_{A0}$, and $0.40v_{A0}$. $v_{\|}/v$ ratio of these test particles are 0.80.

2.4.2 EP-SAW Interaction

The effectiveness of the EP-SAW interaction needs to be analyzed in both the view of the resonant particle orbit and the shape of the spatial and energy distribution function. In the view of the single particle orbit, EP mainly transfers energy to the SAW by interacting with the wave electric field. The EP-SAW energy transfer can be expressed by Eq.2.29. In the context of the SAW, the majority of the EP energy transfer is due to the interaction between the EP guiding center drift velocity and the perpendicular electric field of the SAW. Firstly, the

EP energy transfer through its gyromotion is averaged to zero because the EP gyrofrequency is much higher than the frequency of the SAW. Secondly, the parallel electric and magnetic fields are small. The dominant term for the EP-SAW interaction shown in Eq.2.29 is $e\vec{v}_d \cdot \vec{E}_\perp$.

$$\frac{dW}{dt} = e\vec{v} \cdot \vec{E} + \mu\frac{\partial B_\parallel}{\partial t} \approx e\vec{v}_d \cdot \vec{E}_\perp + ev_\parallel E_\parallel + \mu\frac{\partial B_\parallel}{\partial t} \approx= e\vec{v}_d \cdot \vec{E}_\perp \tag{2.29}$$

To have a non-zero net EP energy transfer, the EP needs to resonate with the SAW. This means that the resonant EP should periodically perceive the same phase of the SAW at the intersection point. The generalized EP-SAW resonance condition in stellarator/heliotron is shown in Eq.2.30[14, 15]. ω, m, j, μ_B, ω_θ, n, ν_B, N_{fp}, and ω_ϕ are mode frequency, poloidal mode number, order of resonance, poloidal mode number of the equilibrium magnetic field, poloidal orbit frequency, toroidal mode number, toroidal mode number of the equilibrium magnetic field, number of the equilibrium field period, and toroidal orbit frequency, respectively. From Eq.2.30, more EP-SAW resonances emerge as the number of the Fourier component of the equilibrium magnetic field increases. This suggests that the number of the EP-SAW energy channels is higher in the stellarator/heliotron than in the tokamak.

$$\omega - (m + j\mu_B)\omega_\theta - (n + j\nu_B N_{fp})\omega_\phi = 0, \tag{2.30}$$

In the realistic plasma, EPs with different values of kinetic energy, pitch angle, and spatial location exist. These EP population with different kinetic energy, pitch angle, and spatial location can be expressed by the distribution function. In the view of the kinetic effect, the EPs drive and damp instability through the inverse Landau damping and Landau damping effects, respectively. The instability driving and damping effects depend on the EP spatial ($\partial f_h/\partial r$), velocity ($\partial f_h/\partial v$) and pitch angle ($\partial f_h/\partial \Lambda$) gradient in the distribution function. In the spatially uniform EP profile, the EP can drive instability through the velocity gradient. If the EP-SAW resonance velocity is located in the region with $\frac{\partial f_h}{\partial v} > 0$ and $\frac{\partial f_h}{\partial v} < 0$, the EP-SAW resonance occurs at this resonance velocity will have a destabilization and stabilizing effects, respectively[52].

In the toroidal plasma experiment, the EP velocity distribution tends to have a slowing-down distribution function where $\partial f_h/\partial v < 0$; however, the destabilization of EP-driven MHD instability can be observed. This contradiction can be resolved by account the effect of the spatial gradient of EP distribution function.

The role of the EP spatial gradient can be explained through the conservation of $E^{'}$ of the EP in the toroidal axisymmetric magnetic configuration (e.g. tokamak). The particle energy (E) and the toroidal momentum (P_{ϕ}) are not conserved in a wave with ω and toroidal mode number n; however, the combination of these terms are conserved ($E^{'} = E - \omega P_{\phi}/n = Constant$)[53, 54]. Since particle interacting with a wave will move along the $E^{'} = Constant$ line, the energy gradient of the partial distribution function along this line can be expressed by Eq.2.31. The second term on the RHS of Eq.2.31 can be simplified to Eq.2.32. In case of the slowing-down EP velocity distribution, the first term of the RHS of Eq.2.31 will have a stabilizing effect ($\partial f/\partial v < 0$). The second term can have a destabilizing effect if $\frac{n\partial f}{\omega \partial P_{\phi}} > 0$. If $\frac{1}{e}\frac{1}{B_{\theta}}\frac{\partial f}{\partial r} > 0$, the destabilized mode will have $n/\omega > 0$. This suggests that the sign of electric charge of resonant particle (e), the sign of poloidal magnetic field (B_{ϕ}), and the sign of the spatial gradient of distribution function ($\partial f/\partial r$) determine the propagation direction of the mode. The perceived EP energy gradient by the $n = 4$ mode with frequency of 70 kHz is shown in figure 2.6. In the panels (a) and (b) of figure 2.6, the co-passing and cntr-passing EP distribution functions in E and P_{ϕ} spaces are shown. The EP spatial distribution is expressed in P_{ϕ}. The $E^{'} = Constant$ lines for $n = 4$ and $f = 70$ kHz mode are represented by white solid line. The perceived EP energy gradient by the $n = 4$ and $f = 70$ kHz mode for the co-passing and counter-passing EPs are shown in panel (c). The perceived EP energy gradient by the mode has a positive energy gradient $\partial f/\partial E > 0$[54].

$$\left.\frac{\partial f}{\partial E}\right|_{E'} = \left.\frac{\partial f}{\partial E}\right|_{P_{\phi}} + \left.\frac{n}{\omega}\frac{\partial f}{\partial P_{\phi}}\right|_{E} \tag{2.31}$$

$$\frac{n}{\omega}\frac{\partial f}{\partial P_{\phi}} \approx \frac{n}{R\omega}(\frac{1}{e})(\frac{1}{B_{\theta}})(\frac{\partial f}{\partial r}) \tag{2.32}$$

In addition to the velocity gradient and spatial gradient of the EP distribution function, the pitch angle gradient can also has an effect on the instability drive. The role of the pitch angle gradient ($\partial f/\partial \Lambda$) can be significant when the anisotropy in EP velocity distribution is large. The example of the plasma experiment with strong anisotropic EP velocity distribution is the plasma discharge with heated by parallel neutral beam injection (NBI). In this example, the majority of the EP population will have a low pitch angle value ($\Lambda = \mu_0 B_0/E$). The role of the EP pitch angle distribution function can be expressed by Eq.2.33. Assuming that the EP pitch angle distribution function has a Maxwellian-like distribution

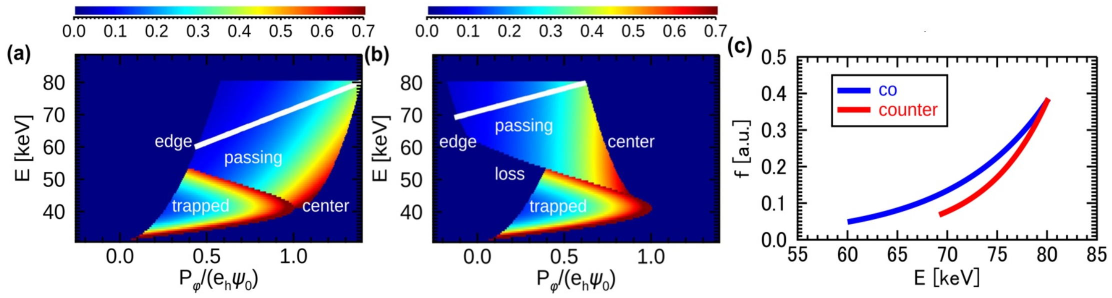

Figure 2.6: The EP velocity and spatial distribution functions for the (a) co-passing EP and (b) cntr-passing EP. The $E^{'} = Constant$ lines for the $70kHz$ for $n = 4$ mode are drawn in white in panels (a-b). The perceived EP distribution function by $E^{'} = Constant$ line for the co-passing and counter-passing EPs are shown in panel (c)[54]

(Eq.2.33), the energy gradient of the EP distribution function is represented by Eq.2.35. Λ_0 and $\Delta\Lambda$ are the center and the width of the pitch angle distribution function. Eq.2.35 suggests that the EP in the region with $\Lambda > \Lambda_0$ ($\Lambda < \Lambda_0$) will have a destabilization (stabilization) effect. The effect of pitch angle gradient is apparent for the $n = 0$ MHD mode such as energetic particle geodesic acoustic mode (EGAM). Since EGAM has $n = 0$, the instability drive by the spatial gradient in EP distribution function is zero (See Eq.2.31. Figure 2.7 shows the nonlinear simulation of EGAM calculated with MEGA[34]. Figure 2.7(a) shows the initial EP distribution in (E,Λ) space. "Area A" and "Area B" are the region in (E,Λ) phase space with $\Lambda > \Lambda_0$ and $\Lambda < \Lambda_0$, respectively. This suggests that the pitch angle gradient in "Area A" should be a destabilizing effect. The effect of pitch angle gradient is shown in panel (b). The EP energy transfer in "Area A" and "Area B" have negative (destabilizing) and positive (stabilizing) value, respectively. The positive energy transfer in the upper region of "Area A" can be explained by the weaker pitch angle gradient along the constant μ line. The role of $\frac{\partial f}{\partial E}\Big|_{\Lambda}$ becomes more dominant in this region.

$$\frac{\partial f}{\partial E} = \frac{\partial f}{\partial E}\bigg|_{\Lambda} + \frac{\partial f}{\partial \Lambda}\bigg|_{E}\frac{\partial \Lambda}{\partial E} \tag{2.33}$$

$$f(E,\Lambda) = f_E f_\Lambda = f_E exp[-\frac{(\Lambda-\Lambda_0)^2}{(\Delta\Lambda)^2}] \tag{2.34}$$

$$\frac{\partial f}{\partial E} = f_\Lambda \frac{\partial f_E}{\partial E} + \frac{2(\Lambda-\Lambda_0)}{\Delta\Lambda^2}(\frac{\mu B_0}{E^2}) f_v f_\Lambda \tag{2.35}$$

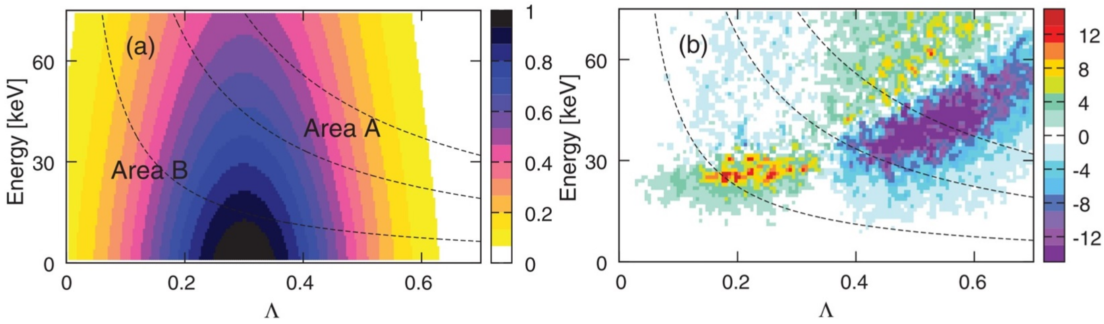

Figure 2.7: The simulation result of the EP energy redistribution by EGAM. Panel (a) shows the initial EP distribution function in (E,Λ) space. Panel (b) show the EP energy redistribution by EGAM in (E,Λ) space. The black dashed lines in panels (a-b) represent the constant magnetic moment (μ)[34].

Chapter 3

Heliotron J

3.1 Introduction

Heliotron J (L=1) is an advanced helical axis heliotron in Kyoto University, where L is the number of helical coil[19, 55]. It is designed based on quasi-isodynamic optimization. It has 4 toroidal field periods. The schematic view of Heliotron J device is shown in figures 3.1(a-b). The basic plasma and device parameters are shown on table 3.1. It was purposed to improve the compatibility between particle confinement and sufficient MHD stability. This was not achieved in Heliotron E (L=2)[56], its predecessor. In Heliotron E, the energy confinement time (τ_E) can be improved in the inward shift magnetic axis (2 cm) configuration[57]; however, this magnetic configuration experiences a wide magnetic hill region. Therefore, the plasma experiences stronger pressure-driven MHD instabilities in the high beta plasma. The magnetic well can be obtained in the outward magnetic axis shift configuration, but a higher transport-level was observed. In Heliotron J, this incompatibility is tackled by forming the vacuum magnetic well throughout the entire plasma volume and provide the external mean to minimize the $|B|$ ripple bottom[58]. The objectives of Heliotron J are [55]:

1. To achieve the compatibility between a good particle confinement and MHD stability.
2. To optimize the helical-axis heliotron configuration.
3. A controllable particle and power-handling scheme.

In this chapter, the Heliotron J magnetic field will be introduced in section 3.2. Section 3.3 will discuss about the EP dynamic in Heliotron J. Section 3.4 will summarize the identified EP driven MHD instabilities in the Heliotron J experiments.

Parameters	Values
Major Radius (R)	1.2 m
Minor Radius (a)	0.15-0.25 m
Plasma Volume	$< 1.0m^3$
Magnetic Field strength at the magnetic axis	¡ 1.5 T
Rotational Transform $\iota/2\pi$	0.5-0.6
Working Gas	Hydrogen and Deuterium

Table 3.1: Heliotron J plasma parameters

3.2 Magnetic Field of Heliotron J

The Heliotron J (HJ) magnetic field is divided into 2 sections: straight and corner sections. The corner and straight sections are indicated by the red and yellow circles in figure 3.1(b), respectively. The poloidal cross-section of the magnetic field intensity of the corner and straight section are shown in figures 3.1(c-d), respectively. The outer and inner black dotted lines represent the HJ vacuum vessel and the magnetic flux surfaces, respectively. The magnetic field of Heliotron J is optimized based on the quasi-isodynamic optimization concept. In this concept, the grad B and curvature drifts are minimized in the straight section of Heliotron J. In this section, the magnetic field line is almost straight (minimize curvature drift), and the magnetic field gradient in the major radius direction is almost constant (see figure 3.1(d)). The magnetic field of Heliotron J possesses 3 main properties: (1) vacuum magnetic well, (2) low magnetic shear, and (3) bumpy field. The profiles of these quantities are shown in figure 3.2. As already mentioned in chapter 1, the magnetic well is necessary to stabilize the pressure-driven MHD instabilities in the high beta plasma. Low magnetic shear is one of the concepts to mitigate the formation of the low order rational magnetic islands which can deteriorate the plasma confinement. Lastly, the bumpy field component is the external mean for controlling the mod B_{min} structure and poloidal drift. These 3 properties will be discussed in detail in the following subsections.

The dominant Fourier magnetic components ($\epsilon_{\mu_B\nu_B}$) of Heliotron J are helicity (ϵ_{11}), toroidicity (ϵ_{10}), and bumpy (ϵ_{01}), where μ_B, ν_B, and $\epsilon_{\mu_B\nu_B}$ are poloidal mode number, toroidal mode number, and the ratio between $B_{\mu_B\nu_B}/B_{00}$, respectively. These magnetic Fourier components are produced by the single helical coil ($L = 1$), the toroidal field coil A, the toroidal field coil B, and the three sets of poloidal field coils (PF). The $L = 1$ helical coil is utilized in Heliotron J because a vacuum magnetic well is difficult to achieve in the $L = 2$ helical coils system. The helical coil of Heliotron J was designed based on the helical coil winding law with

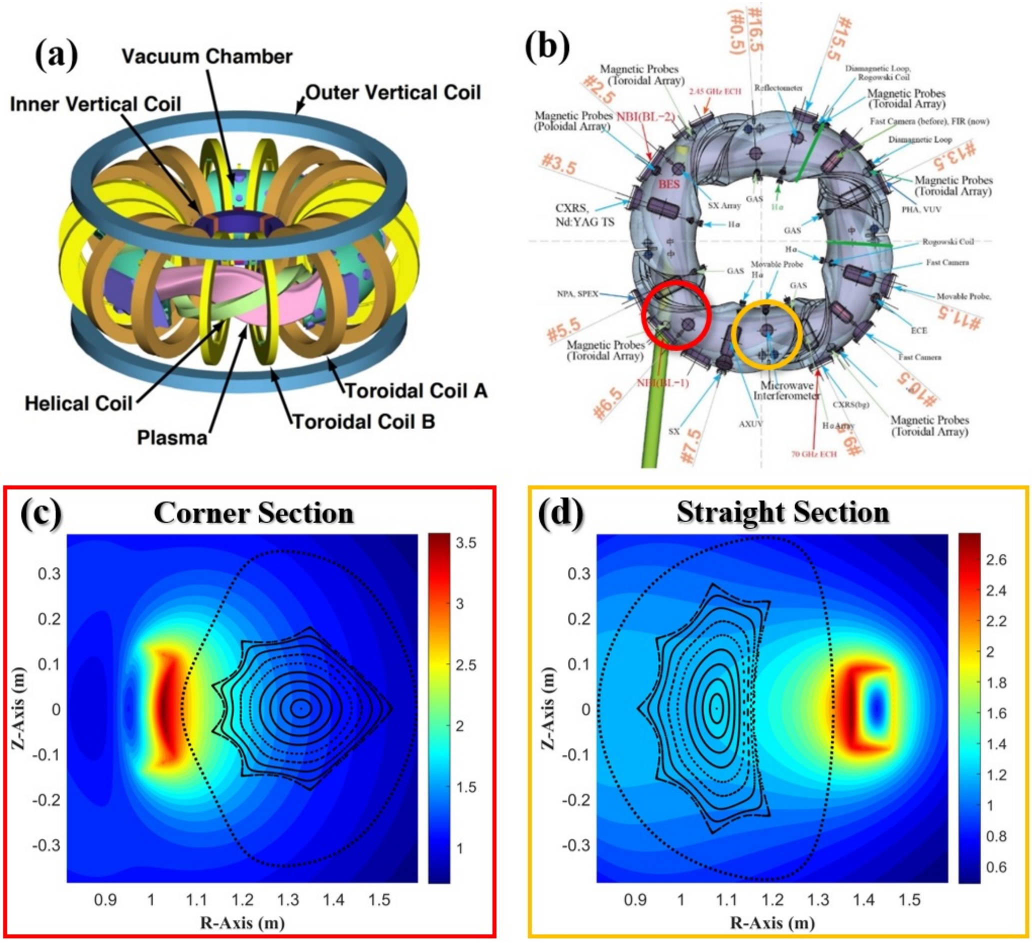

Figure 3.1: Schematic view of Heliotron J. The magnetic coils of Heliotron J consist of a helical continuous helical coil, toroidal field coil A, toroidal field coil B, inner poloidal coil, and outer poloidal coil. Panels (a) and (b) show the magnetic coils system and bird's-eye view, respectively. A schematic view of the neutral beam injection (NBI) system in Heliotron J is also shown in panel (b). In the normal (reversed) magnetic field configuration, the toroidal magnetic field is in the clockwise (counterclockwise) direction; therefore, the BL1 and BL2 are counter- and co-injections, respectively. The poloidal cross-section of the vacuum magnetic field strength at the corner and straight sections of Heliotron J for the standard (medium bumpiness) configuration is shown in panels (c-d), respectively. The corner and straight sections of Heliotron J are marked in panel (b) by the red and yellow circles, respectively. The Poincaré plot of the vacuum magnetic field is represented by the black markers.

the negative pitch modulation ($\alpha = -0.4$). The helical coil winding law is given by Eq.3.1[59]. The negative pitch modulation is selected (1) to generate the vacuum magnetic well throughout the confinement region and (2) to minimize the unfavorable bumpy component. The toroidal field coils A and B are used to control the bumpy component and the rotational transform ($\iota/2\pi$). Lastly, the poloidal field coils are utilized to control the plasma shape and position. Various magnetic

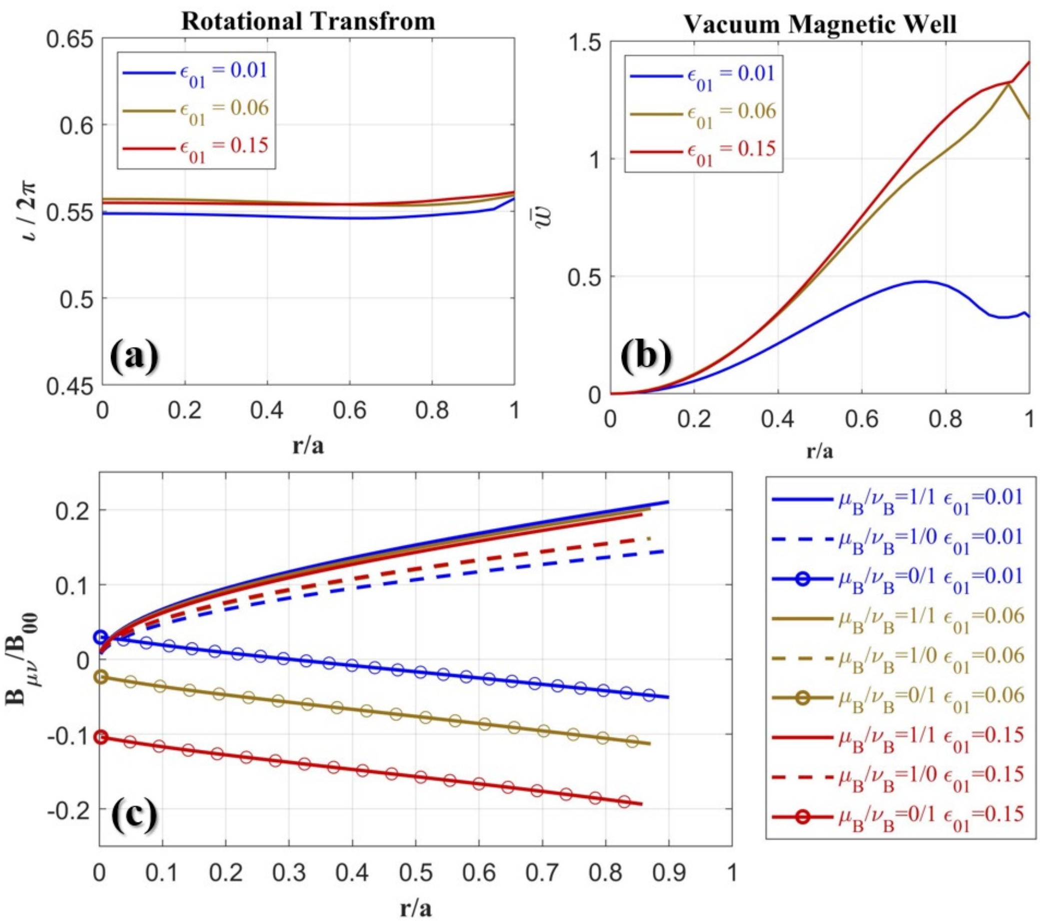

Figure 3.2: The rotational transform ($\iota/2\pi$), the vacuum magnetic well profiles, and the Fourier components of the Heliotron J vacuum magnetic field are shown in panels (a-c), respectively. These quantities are shown for the low ($\epsilon_{01} = 0.01$), standard ($\epsilon_{01} = 0.06$), and high bumpiness ($\epsilon_{01} = 0.15$) configurations. ϵ_{01} is the ratio between the bumpy Fourier component and the DC component of the magnetic field. The major difference is the bumpy component, which has the highest value in the high bumpiness configuration.

configurations can be created by adjusting the magnetic coil current. There are 3 main magnetic configurations of Heliotron J: low bumpiness ($\epsilon_{01} = 0.01$), medium bumpiness ($\epsilon_{01} = 0.06$), and high bumpiness ($\epsilon_{01} = 0.15$) configurations. The major differences between these configurations are the amplitude of the bumpy component.

$$\theta = \pi + (M/L)\phi - \alpha sin(M/L)\phi \tag{3.1}$$

Low Magnetic Shear

Magnetic shear is defined by a radial variation of rotational transform profile. Low magnetic shear is purposed to minimize the deterioration of the plasma confinement by low order rational magnetic surface. Low order rational surface is avoided by localizing rotational transform value in a region without low order rational surface. The rotational transform profiles of the vacuum magnetic field of Heliotron J for each magnetic configuration are shown in figure 3.2(a). In terms of MHD instability, the avoidance of low order rational surfaces can mitigate the destabilization of interchange mode[22]. For the EP-driven MHD instability, the formation of the coupling type gap modes, such as toroidal Alfvén eigenmode (TAE), ellipticity-induced Alfvén eigenmode (EAE), and helicity-induced Alfvén eigenmode (HAE) are unlikely because the limited range of rotational transform is unlikely to satisfy the coupling criteria. The commonly observed EP-driven MHD instabilities in low shear device is global Alfvén eigenmode (GAE) and energetic particle mode (EPM). Lastly, the radial width of the MHD instability in low shear stellarator/heliotron is relatively large.

Vacuum Magnetic Well

Due to the absence of the shear stabilization, the MHD stability against the pressure-driven MHD instability in Heliotron J is brought about by the vacuum magnetic well. The spatial profiles of the vacuum magnetic well for each magnetic configuration are shown in figure 3.2(b). The depths of the vacuum magnetic well of the low bumpiness, standard, and high bumpiness magnetic configurations are roughly 0.5%, 1.0%, and 1.5%, respectively.

Bumpiness

Bumpy field allows external control of the mod B_{min} structure and the radial magnetic field gradient. It is useful to improve trapped particle confinement by externally control the

1. Radial location and size of the mod B_{min}
2. Toroidal location of the mod B_{min}
3. Poloidal drift velocity.

This can be understood by investigating the orbit of deeply trapped particles. The mod B_{min} structure is utilized because it represents the orbit of the deeply trapped particle. It is derived from the conservation of longitudinal adiabatic invariant ($J_{\parallel}$). In the absence of the electric field, the $J_{\parallel}$ is represented by equation 3.2, where m, $v_{\parallel}$, ds, E, μ, and B_{min} are particle mass, parallel velocity, spatial step length along particle trajectory, particle energy, magnetic moment, and minimum magnetic field strength along magnetic field line. Since the energy is conserved, deeply trapped particle will follow B_{min} path ($E = \mu B_{min}$). To confine this deeply trapped particle, the mod $\mathrm{B_{min}}$ contour must be closed.

$$J_{\parallel} = m \oint v_{\parallel} ds \propto (E - \mu B_{min})^{\frac{1}{2}} \tag{3.2}$$

The closed mod $\mathrm{B_{min}}$ contour condition was studied by *M. Yokoyama et al, 2000*[59] in the helical axis heliotron configuration with the helicity (ϵ_h), toroidicity (ϵ_t), and bumpy (ϵ_b) field components. The radial dependence of the helicity and toroidicity are assumed by $\epsilon_h = \epsilon_{ha}(r/a)$ and $\epsilon_t = \epsilon_{ta}(r/a)$, respectively. ϵ_{ha}, ϵ_{ta}, and r/a are the helicity at the LCFS, toroidicity at the LCFS, and normalized radius, respectively. The expressions of mod $\mathrm{B_{min}}$ structure are shown in equations 3.3-3.6. Equation 3.3 describes the poloidal cross section of the mod $\mathrm{B_{min}}$ contour, where x and y are mod $\mathrm{B_{min}}$ horizontal position and mod $\mathrm{B_{min}}$ vertical position, respectively. This equation turns into elliptic equation if and only if the e^2, a square of elongation, term is positive. This implies $\epsilon_{ha} > \epsilon_{ta}$. The X_{dtp} and ρ^2_{dtp} determine the center of the mod $\mathrm{B_{min}}$ contour and its size, respectively. The mod $\mathrm{B_{min}}$ contour breaks if it intersects with the LCFS ($r/a = 0$) or $\rho_{dtp} = 0$. These two terms are affected by ϵ_{ha}, ϵ_{ta}, and ϵ_b; therefore, it can be externally adjusted through ϵ_b. The appropriate ϵ_b range for the closed mod $\mathrm{B_{min}}$ contour was derived based on the above conditions. As $\epsilon_{ta}/\epsilon_{ha}$ approaches 1, more negative ϵ_b is required to close the mod $\mathrm{B_{min}}$ contour. The introduction of the negative bumpy field ($\epsilon_b < 0$) can minimize the variation of the magnetic field ripple bottom. This process is also known as σ optimization[58].

$$(x - X_{dtp})^2 + e^2 y^2 = \rho^2_{dtp} \tag{3.3}$$

$$X_{dtp} = -\frac{\epsilon_{ha}\epsilon_b + \epsilon_{ta}(1 - \frac{E}{\mu B_{00})}}{\epsilon^2_{ha} - \epsilon^2_{ta}} a \tag{3.4}$$

$$e^2 = \frac{\epsilon^2_{ha}}{\epsilon^2_{ha} - \epsilon^2_{ta}} \tag{3.5}$$

$$\rho_{dtp}^2 = \frac{[(1-\frac{E}{\mu B_{00}})\epsilon_{ha} + \epsilon_b\epsilon_{ta}]^2}{(\epsilon_{ha}^2 - \epsilon_{ta}^2)^2} a \tag{3.6}$$

If the radial dependence of the bumpy field is included in the analysis, the mod B_{min} contour will not extend throughout the torus. Instead, it will be toroidally localized in a toroidal field period. The collisionless particle confinement significantly improves by the toroidally localized mod B_{min} contour. This is caused by the enhancement of the poloidal drift of particle in the closed mod B_{min} contour region, while the radial drift is unchanged.

3.3 Energetic Particles in Heliotron J

In Heliotron J, the EP is produced by the parallel neutral beam injection (NBI). The schematic view of the NBI system in Heliotron J is also shown in figure 3.1(b). There are two hydrogen NBI systems in Heliotron J (BL1 and BL2). In the normal magnetic field direction, the first NBI (BL1) is in the counter-injection, while the second NBI (BL2) is in the co-injection. In this context, the co-direction is defined as the direction of plasma current that increases the rotational transform ($\iota/2\pi$). The injected energy of the neutral beam in Heliotron J is 28 keV, which has the velocity of $\approx 0.38 v_{A0}$ for the deuterium plasma with the density and magnetic field strength of $1.0 \times 10^{19} m^{-3}$ and 1.25 T, respectively. Due to the helical axis, the pitch angle between the BL1 and BL2 beam lines and the local magnetic axis has a wide range. The injected EP pitch angles between the BL1 and BL2 beam lines and the local magnetic axis vary from 145° to 175° and 5° to 40°, respectively.

The EP velocity distribution in Heliotron J in the low beta plasma has been investigated by the charge-exchange neutral particle analyzer (CX-NPA). The deuterium plasma was heated by the combination of electron cyclotron heating (ECH) and neutral beam injection (NBI). The EP energy spectra in the standard configuration with the electron density (n_0) of $0.3 \times 10^{19} m^{-3}$ and $0.8 \times 10^{19} m^{-3}$ are shown in figure 3.3[60]. The unfilled markers represent the experimental measurement, while the solid lines represent the Fokker-Planck calculation results. According to the experimental results, the bump-on-tail structure were observed at the E, $E/2$, and $E/3$ components of the maximum neutral beam energy. The Fokker Planck calculation with $\tau_s \gg \tau_{cx}$ can reproduce the experimental observation, where τ_s and τ_{cx} are the slowing-down and charge exchange times, respectively. This indicates that the charge exchange loss rate is higher than the slowing down rate in the low beta plasma. The causes of the high charge exchange loss rate are the Heliotron J plasma size and the finite neutral particle penetration in the core region. The slowing-down time (τ_s) is reduced as the plasma density increases.

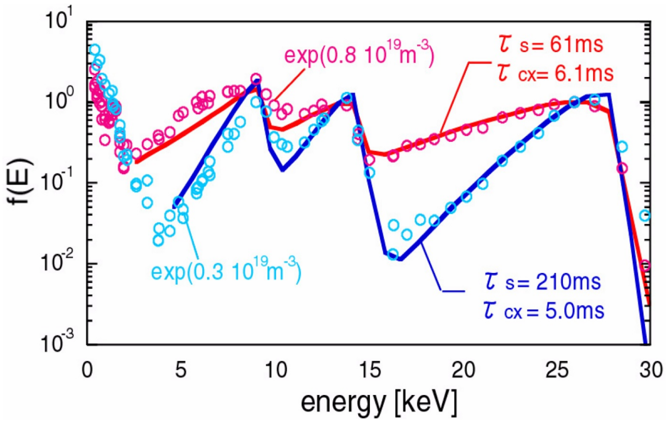

Figure 3.3: The measured EP energy spectra in the low beta ECH and NBI heated plasma discharge in the standard magnetic configuration[28, 60]

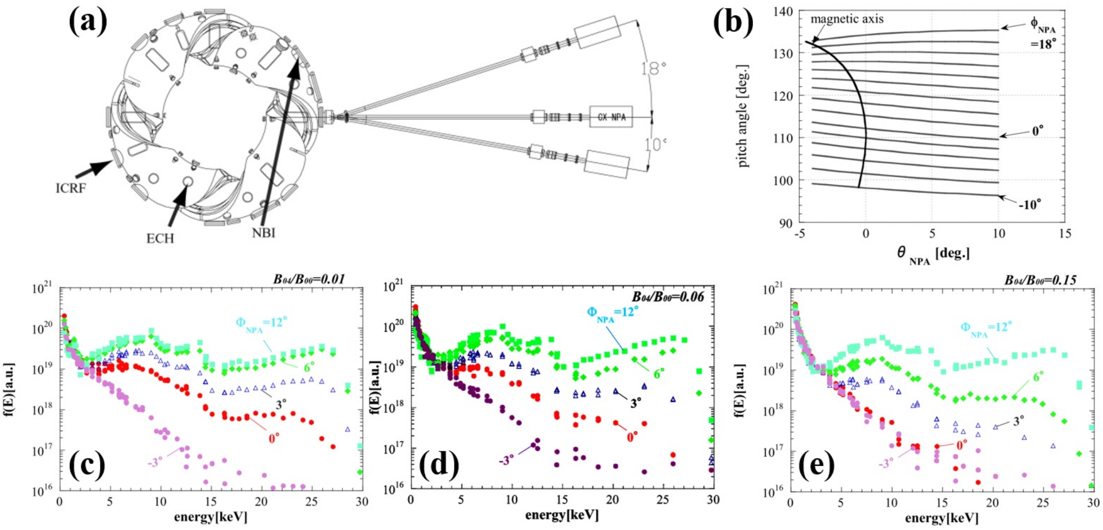

Figure 3.4: CX-NPA system in Heliotron J. Panel (a) shows the top view of the CX-NPA system, while panel (b) shows the detected particle pitch angle with respect to the poloidal (θ_{NPA}) and toroidal (ϕ_{NPA}) measuring angles, respectively. The measured CX-flux for low beta plasma in the low, standard, and high bumpiness configurations are shown in panels (c-e), respectively.[28].

The role of the bumpy component on the EP collisionless confinement was investigated by the charge exchange neutral participle analyzer (CX-NPA)[27, 28]. The CX-NPA system of Heliotron J is shown in figures 3.4(a-b). The detected EP pitch angle can be altered by varying the toroidal (ϕ_{NPA}) and poloidal (θ_{NPA}) measuring angles of the CX-NPA. The EP energy distributions measured with

CX-NPA for the low, standard, and high bumpiness configurations are shown in figures 3.4(c-e). This experiment was conducted in the low beta plasma condition ($n_0 = 0.8 \times 10^{19} m^{-3}$). The plasma was heated by ECH and co-injected NBI. From figures 3.4(c-e), the measured CX-flux at the $\phi_{NPA} = 3°$ and $6°$ measuring angles (equivalent to $115°$ and $125°$ pitch angles) are lower for the high bumpiness configuration. This was explained by the change in the loss cone shape due to the bumpy field. The decay times of the CX flux from these magnetic configurations were compared. The compared CX fluxes were measured at the $\phi_{NPA} = 12°$ angle because the CX flux at this angle is almost the same in all 3 magnetic configurations. The results showed that the decay time of the measured CX flux at the $\phi_{NPA} = 12°$ angle increases as the bumpy field intensity increases. The time evolution of the measured CX flux at the $\phi_{NPA} = 12°$ measuring angle for each magnetic configuration is shown in figure 3.5.

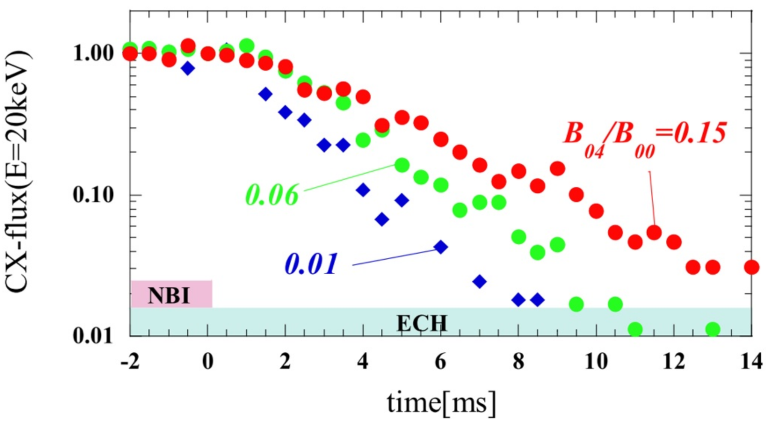

Figure 3.5: Time evolution of the measured CX flux for $20keV$ at the $\phi_{NPA} = 12°$ measuring angle for each magnetic configuration[28]. The blue, green, and red markers represent the measured results from the low bumpiness ($\epsilon_b = 0.01$), standard ($\epsilon_b = 0.06$), and high bumpiness ($\epsilon_b = 0.15$) configurations, respectively.

3.4 EP-driven MHD instabilities in Heliotron J

As mentioned above, the commonly observed EP-driven MHD modes in Heliotron J are EPM and GAE. These modes are destabilized by the NBI generated EPs. The destabilization by other species, such as energetic electrons, has not yet been observed and identified. For the low beta currentless MHD equilibria, the commonly observed EP-driven MHD modes are

1. n/m=1/2 Energetic particle mode (EPM)

2. n/m=2/4 Global Alfvén eigenmode (GAE).

These modes can be destabilized either by co- or counter-injected NBIs. The experimentally results for the low beta currentless plasma are presented in this section. The selected discharge is #61569[25]. This discharge was heated by both the ECH and the balanced NBIs where the plasma beta (β_0) at the magnetic axis is averagely around 0.37%. The magnetic configuration for this discharge is the low bumpiness ($\epsilon_b = 0.01$) configuration. The cross power spectrum density between the toroidal and poloidal magnetic probe signals of the#61569 discharge is shown in figure 3.6(a). Two coherent modes can be observed within the $83.4kHz < f < 95.0kHz$ and $136.7kHz < f < 148.4kHz$ ranges. According to the mode identification in Ref.[25], the coherent modes within the $83.4kHz < f < 95.0kHz$ and $136.7kHz < f < 148.4kHz$ frequency ranges are the $n/m = 1/2$ EPM and the $n/m = 2/4$ GAE, respectively. The $n/m = 1/2$ EPM has a chirping behavior which indicates a strong interaction with the shear Alfvén continuum (The linear growth rate and the damping rate are comparable). The time evolution of the line averaged density ($\overline{n}_0$), the plasma store energy (W_p), the net plasma current (I_p), the ECH signal, and the NBI signal are shown in figures 3.6(b-e), respectively. The net toroidal plasma current ($|I_p|$) is near zero. The line averaged density slowly increases until 260 ms. From 260 ms onward, the line averaged density remains constant. It can be seen that both the $n/m = 1/2$ EPM and the $n/m = 2/4$ GAE have a weak dependence on the line averaged density. This suggests that these two modes are located near the plasma edge because the change in the local density value in the edge region is much lower than the core region.

The spatial profiles of the $n/m = 1/2$ EPM and the $n/m = 2/4$ GAE are obtained from the density fluctuation profiles measured with the beam emission spectroscopy (BES) signal. The averaged density fluctuation (solid line with circular marker) within the $83.4kHz < f < 95.0kHz$ ($n/m = 1/2$) and $136.7kHz < f < 148.4kHz$ ($n/m = 2/4$) frequency ranges are shown in figures 3.7(a-b), respectively. The averaged density fluctuation is deducted by the background noise level. The coherence (purple dashed line) between the BES and the toroidal magnetic probe signals are also shown in these figures. In the $83.4kHz < f < 95.0kHz$ frequency range, two coherent modes are formed around $0.20 < r/a < 0.40$ and $0.60 < r/a < 0.80$. The later has a higher density fluctuation amplitude. For the $136.7kHz < f < 148.4kHz$ frequency range, the coherent mode has a much lower amplitude. The deficit between the averaged density fluctuation amplitude and the noise level is maximized around $r/a = 0.675$. This radial location also has a maximum coherence with the toroidal magnetic probe

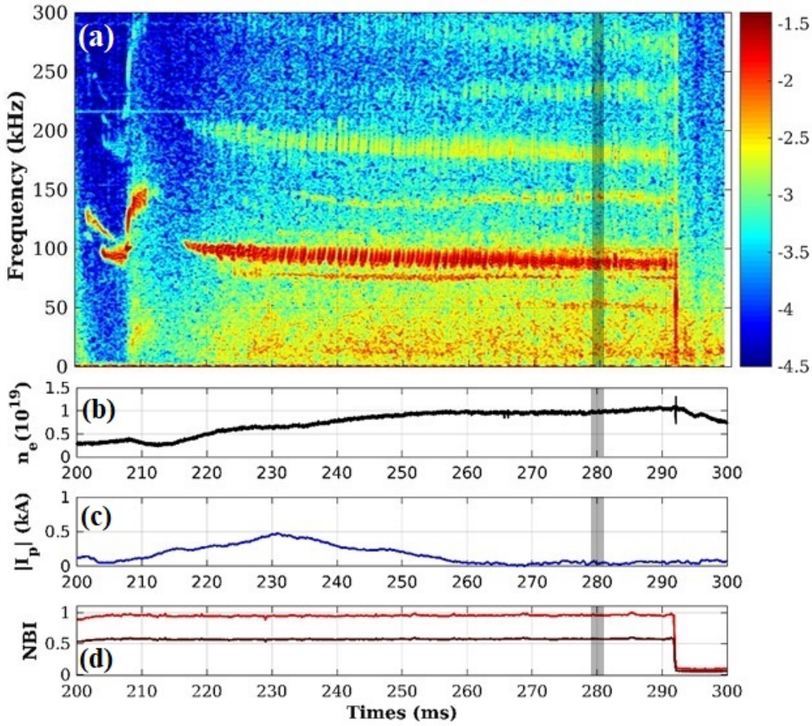

Figure 3.6: The time evolution of (a) the cross power spectrum density between toroidal and poloidal magnetic probes, (b) the line averaged density ($\overline{n}_0$), plasma store energy (W_p), the net plasma current (I_p), the ECH signal, and the NBI signal. These signals are from the #61569 Heliotron J experiment discharge, where the low bumpiness configuration is utilized[25, 61]

signal. The estimated toroidal mode numbers of the coherent modes within these frequency ranges is calculated from the phase difference between each toroidal Mirnov coil (figure 3.8). The toroidal mode number of the coherent modes within the $83.4kHz < f < 95.0kHz$ and $136.7kHz < f < 148.4kHz$ frequency ranges are $1 + i * N_{fp}$ and $2 + i * N_{fp}$, respectively, where i and N_{fp} are any arbitrary integer and Heliotron J toroidal field period, respectively. The radial location and the frequency of these coherent modes are compared to the calculated $N_f = 1$ and $N_f = 2$ shear Alfvén continua (see figure 3.9), where N_f is a toroidal mode family. These shear Alfvén continua are solved with the STELLGAP[18] code. The measured coherent modes agree with the $n/m = 1/2$ and $n/m = 2/4$ shear Alfvén continua.

In addition to the EPM and GAE, other EP-driven MHD modes were also observed and reported in the MHD equilibrium with finite plasma current. For example, the low frequency Alfvénic mode was observed in the MHD equilibrium with the finite plasma current driven by co-NBI injection (NBCD)[26]. This mode can only be observed when the plasma current exceeds $I_p > 1.00kA$. The candidate

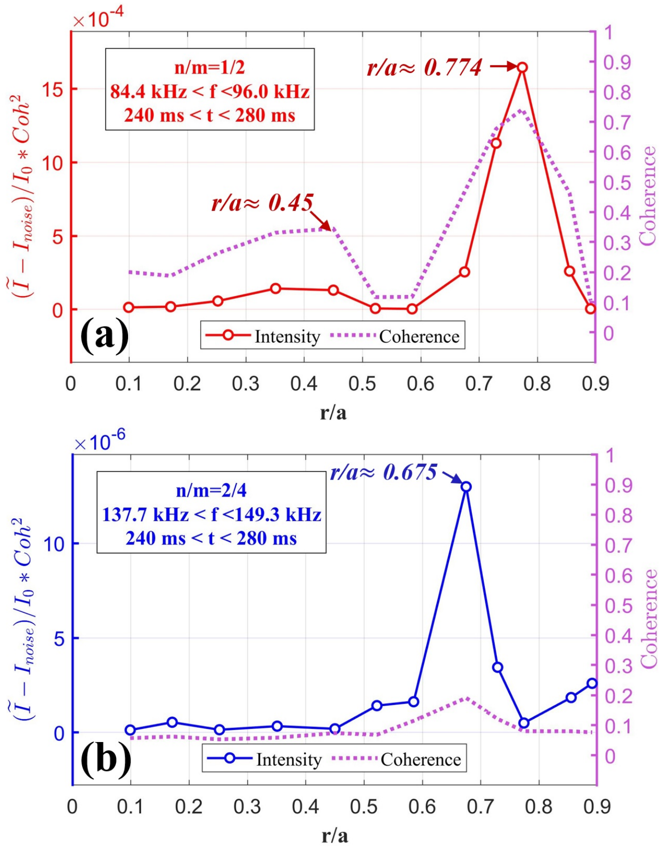

Figure 3.7: The average density fluctuation profile (solid line with unfilled circles) measured with the beam emission spectroscopy (BES) signal and the coherence (purple dashed line) of BES and the toroidal magnetic probe signals. The density fluctuation amplitude for the coherent mode is deducted by its noise level and then multiplied by its magnitude squared coherence. The density fluctuation amplitude for the coherent mode is referred to the left vertical axis, while the coherence is referred to the right vertical axis. The average density fluctuation profile and coherence are calculated within the (a) $83.4kHz < f < 95.0kHz$ and (b) $136.7kHz < f < 148.4kHz$ frequency ranges.

of the low frequency Alfvénic mode is the beta-induced Alfvén eigenmode (BAE); however, it is not in the scope of the thesis.

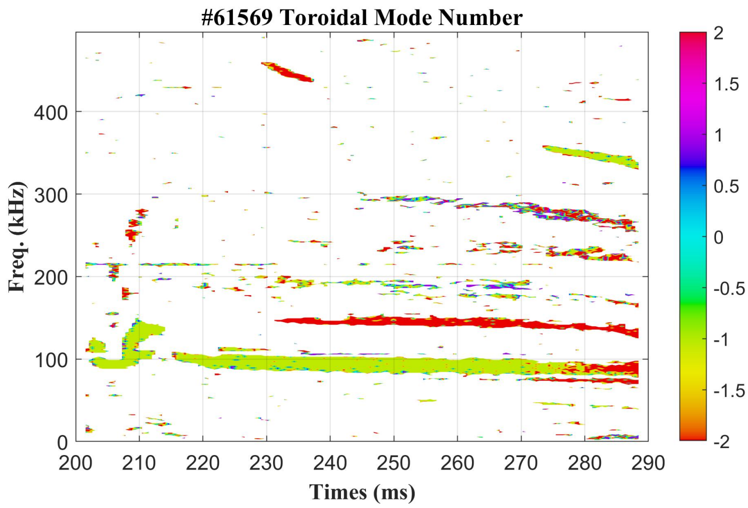

Figure 3.8: The estimated toroidal mode number "n" from the four toroidal Mirnov coils array. Any fluctuation that has a lower coherence than the threshold value is neglected.

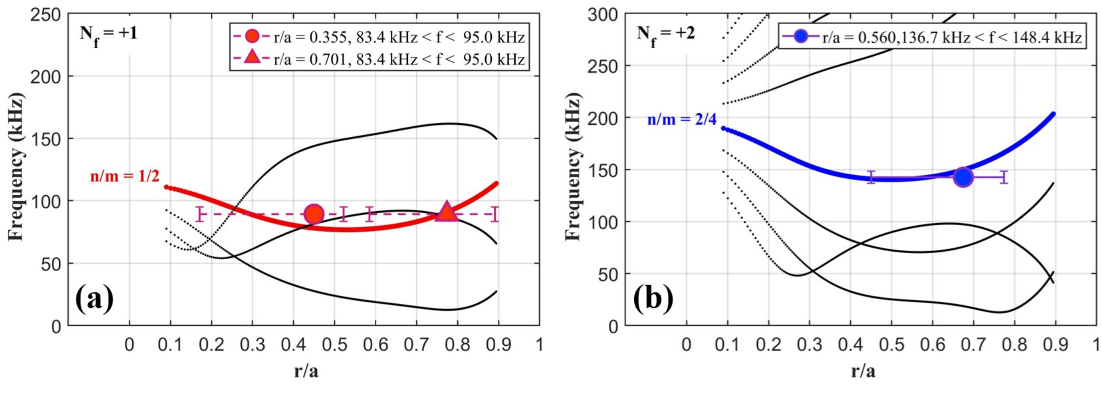

Figure 3.9: The shear Alfvén continua for (a) $n = +1$ and (b) $n = +2$ mode families for the $\beta_0 = 0.36\%$ currentless #61569 discharge of Heliotron J. The coherent modes within the $83.4kHz < f < 95.0kHz$ and $0.171 < r/a < 0.522$, the $83.4kHz < f < 95.0kHz$ and $0.585 < r/a < 0.891$, and the $136.7kHz < f < 148.4kHz$ and $0.45 < r/a < 0.774$ ranges are represented by the red circular, red triangular, and blue circular markers, respectively.

Chapter 4

Simulation Model

Plasma simulation is a powerful methodology to investigate complex physical phenomena that are arduous to be experimentally observed or explained by theory. In the field of the EP-driven MHD instability, plasma simulation has been proven to be effective for investigating the linear properties of Alfvén eigenmode, a saturation of Alfvén eigenmodes, nonlinear interaction of multiple modes, EP transport by AEs, and EP-SAW interaction in the three-dimensional toroidal fusion plasma geometry[31, 34, 47, 62, 63, 64, 65, 66, 67, 68, 69].

Plasma physical phenomena in magnetic confinement fusion plasma have wide ranges of characteristic time and length scales. Selecting an appropriate plasma model is essential to obtain good compatibility between the computational resource consumption and the theoretical representation. These can be achieved by neglecting excessive plasma information. Generally, the plasma model can be described by either kinetic or fluid models. The kinetic model contains much more plasma information than the fluid model; however, substantially larger computational resources are required. In contrast, the fluid model requires much lower computational resources, but at the expense of some plasma information. The brief summary of the plasma model has been given in figure 2.1. In this chapter, the existing computational codes for EP-driven MHD instability simulation are briefly summarized in section 4.1. MEGA, an EP-MHD hybrid simulation code, will be introduced in the section 4.2.

4.1 Computational Codes for EP-driven MHD Instability Simulation

Several computational codes have been developed to study the EP-driven MHD instability in a toroidal magnetic confinement fusion device. Depending on the targeted physics, the utilized models for bulk ion, bulk electron, and EP are varied. The summary of the existing computational codes for the study of EP-driven MHD mode is shown in Table 4.1 In this area, the hybrid simulation code, a combination of both kinetic and fluid models, is often utilized. In the hybrid simulation code, EPs (e.g. fusion produced α particle) are treated by the kinetic equations, while the bulk plasmas (thermal ion and electron) are treated by the fluid model. This means that the bulk plasma kinetic effects (e.g. thermal ion and electron Landau damping) are neglected. In some of the model, the thermal ion can also be treated kinetically. The energetic particle and the bulk plasma are coupled by the pressure or by the current density terms in the momentum equations. In this thesis, MEGA[32], a hybrid simulation code, is used. This code will be discussed more in detail in the following section.

Simulation Code	**Ion**	**Electron**	**EP**
MEGA[47]	Nonlinear single fluid MHD	Nonlinear single fluid MHD	Drift Kinetic
GTC[36]	Gyrokinetic	Adiabatic fluid electron	Gyrokinetic
FAR3D[39, 31]	Reduced MHD	Reduced MHD	Landau Closure Model

Table 4.1: Brief summary of the simulation codes and the utilized equations for bulk ion, bulk electron, and EP species.

4.2 MEGA Code

MEGA is an EP-MHD hybrid simulation code that uses nonlinear magnetohydrodynamic (MHD) equations for bulk plasma and drift kinetic equation for EP [32, 40]. The bulk plasmas and the EPs are coupled through the plasma current density. These equations are solved as an initial value problem where the initial condition is MHD equilibrium. Since MEGA lacks the kinetic description of the bulk ion and electron, the bulk plasma kinetic effects (e.g. ion and electron Landau dampings) are excluded. The time integration is carried out by 4^{th} order Runge-Kutta, which is an explicit method. The time evolution of the marker weight can be described either by the δf or $full - f$ method. This depends on the choice of the EP particle source and sink. In the simulation without the consideration of the EP particle source and sink, the δf method is preferred since numerical noise is lower. The $full - f$ method has a higher numerical noise; therefore, it will only be used when the particle source and sink are considered in the simulation.

4.2.1 MHD equations

The single fluid MHD equations in MEGA are shown as follows:

$$\frac{\partial \rho}{\partial t} = -\nabla \cdot (\rho \vec{v}) + \nu_n \Delta(\rho - \rho_{eq}) \ . \tag{4.1}$$

$$\begin{aligned} \rho \frac{\partial \vec{v}}{\partial t} = & \quad -\rho(\vec{v} \cdot \nabla)\vec{v} - \nabla P + (\vec{J} - \vec{J}_h) \times \vec{B} \\ & -\nabla \times (\nu\rho(\nabla \times \vec{v})) + \tfrac{4}{3}\nabla(\nu\rho\nabla \cdot \vec{v}) \ . \end{aligned} \tag{4.2}$$

$$\begin{aligned} \frac{\partial P}{\partial t} = & \quad -\nabla \cdot (P\vec{v}) - (\gamma - 1)P\nabla \cdot \vec{v} \\ & +(\gamma - 1)[\nu\rho\omega^2 + \tfrac{4}{3}\nu\rho(\nabla \cdot \vec{v})^2 \\ & +\eta\vec{J} \cdot (\vec{J} - \vec{J}_{eq})] + \nu_n \Delta(P - P_{eq}) \ . \end{aligned} \tag{4.3}$$

$$\frac{\partial \vec{B}}{\partial t} = -\nabla \times \vec{E} \ , \tag{4.4}$$

$$\mu_0 \vec{J} = \nabla \times \vec{B} \ , \tag{4.5}$$

$$\vec{E} = -\vec{v} \times \vec{B} + \eta(\vec{J} - \vec{J}_0) \ . \tag{4.6}$$

$$\vec{\omega} = \nabla \times \vec{v} \ . \tag{4.7}$$

Eqs.4.1-4.6 are the continuity, momentum, energy, Maxwell-Faraday, Ampére's circulation law, and generalized Ohm's law equations, respectively. The μ_0, γ, η, ν, ν_n, and $\vec{\omega}$ in these equations are vacuum magnetic permeability, adiabatic constant, resistivity, artificial viscosity coefficient, artificial diffusion coefficients, and vorticity respectively. The subscript "eq" represents equilibrium variable. These dissipation coefficients are used to maintain numerical stability by dissipating the small-scale structures into heat through Eq.(4.3)[70]. They are assumed to be constant throughout the plasma.

The contribution of EPs to the bulk plasma can be found in the third term on the RHS of the momentum equation [Eq.(4.2)] in terms of EP current density ($\vec{J}_h$). The deduction of the EP current density ($\vec{J}_h$) from the total plasma current density ($\vec{J}$) is equivalent to the bulk plasma current density. The EP current density ($\vec{J}_h$) is obtained through the first-order velocity moment integration of the EP distribution [Eq.(4.15)]. In this equation, the contribution from the EP $E \times B$ drift is neglected due to the quasi-neutrality condition. This model is valid only if the EP density is negligible when compared to the bulk plasma density.

4.3 EP drift kinetic equations

EP dynamic is described by the drift kinetic approximation[71] where the contribution from the fast gyration is neglected. The guiding center drift equations for EP are given by

$$\vec{v}_h = \vec{v}_\parallel^* + \vec{v}_{\nabla B} + \vec{v}_E \ , \tag{4.8}$$

$$\vec{v}_\parallel^* = \frac{v_\parallel}{b_\parallel^*}[\vec{b} + \rho_\parallel \nabla \times \vec{b}] \ , \tag{4.9}$$

$$\vec{v}_{\nabla B} = -\mu \frac{\nabla B \times \vec{B}}{Z_h e B^2 b_\parallel^*} \ , \tag{4.10}$$

$$\vec{v}_E = \frac{\vec{E} \times \vec{B}}{B^2 b_\parallel^*} \ , \tag{4.11}$$

$$b_\parallel^* = 1 + \rho_\parallel \vec{b} \cdot (\nabla \times \vec{b}) \ , \tag{4.12}$$

$$\rho_\parallel = \frac{m_h v_\parallel}{Z_h e B} \ , \tag{4.13}$$

$$m_h \frac{dv_\parallel}{dt} = (\vec{b} + \rho_\parallel \nabla \times \vec{b}) \cdot (Z_h e \vec{E} - \mu \nabla B) \ , \tag{4.14}$$

where $v_\parallel, \mu, m_h$, and $Z_h e$ are EP's parallel velocity, magnetic moment (adiabatic invariant), mass, and electric charge, respectively. The guiding center drift of EP includes parallel velocity, curvature drift, grad-B drift, and $E \times B$ drift. In this model, the inertia drift (polarization drift) is neglected, since the variation of the electric field with respect to time is negligible for the particle dynamics when compared to the other terms. The EP current density $\vec{J}_h$ is obtained from the 1^{st} order velocity moment integration of guiding center velocity

$$\vec{J}_h = \ Z_h e \int (\vec{v}_\parallel^* + \vec{v}_{\nabla B}) f_h(\vec{r}, v, \Lambda, t) d^3 v$$

$$-\nabla \times \int \mu \vec{b} f_h(\vec{r}, v, \Lambda, t) d^3v \ , \tag{4.15}$$

where $v = \sqrt{v_{\|}^2 + 2\mu B/m_h}$, $\Lambda = 2\mu B_0/m_h v^2$, and B_0 is the magnetic field strength at the plasma center. In Eq.(4.15), $E \times B$ drift is neglected due to quasi-neutrality, and the second term on the RHS represents the magnetization current.

The δf method is employed in this thesis. The equilibrium marker distribution is initially distributed uniformly in phase space $(R, \phi, z, v, v_{\|}/v)$, where R, ϕ, z are cylindrical coordinates. Under this condition, the number of physical particles that are presented by a single marker is proportional to the product of the equilibrium distribution function and the Jacobian of phase space $J = 2\pi R v^2$. The normalization factor α can be obtained from Eq.(4.16) while the time evolution of the marker weight (w_i) is calculated by Eq.(4.16).

$$\frac{1}{2}\int (P_{h\|0} + 2P_{h\perp 0}) dV = \alpha \sum_{i=1}^{N} J_i (\frac{1}{2} m_h v_{i\|}^2 + \mu_i B(\vec{r}_i)) f_{h0}(\vec{r}, v, \Lambda, t)$$

$$\frac{dw_i}{dt} = \ -\alpha J_i \Big[\delta \vec{v}_h \cdot \nabla f_{h0} + \left(\tfrac{d\vec{v}}{dt}\right)\left(\tfrac{\partial f_{h0}}{\partial v}\right) + \left(\tfrac{d\Lambda}{dv}\right)\left(\tfrac{\partial f_{h0}}{\partial \Lambda}\right) \Big]$$

Lastly, $P_{h\|}$ and $P_{h\perp}$ are calculated from 2nd velocity moment integration and particle weight,

$$P_{h\|} = P_{h\|0} + \sum_{i=1}^{N} w_i m_h v_{\|i}^2, \tag{4.16}$$

$$P_{h\perp} = P_{h\perp 0} + \sum_{i=1}^{N} w_i \mu_i B(\vec{r}_i). \tag{4.17}$$

The initial EP distribution (f_{h0}) is assumed to be separable and given by

$$f_{h0} = f_{hs}(\vec{r}) f_{hv}(v) f_{h\Lambda}(\Lambda) \ , \tag{4.18}$$

where $f_{hs}(\vec{r})$, $f_{hv}(v)$, and $f_{h\Lambda}(\Lambda)$ are the equilibrium spatial, velocity, and pitch-angle EP distribution functions. In this simulation, the EP spatial distribution term $f_{hs}(\vec{r})$ is proportional to the EP equilibrium pressure profile. The velocity and pitch-angle distribution terms $f_{hv}(v)$ and $f_{h\Lambda}(\Lambda)$ are given by

$$f_{hv}(v) = (v^3 + v_c^3)^{\left(\frac{\tau_{sd}}{3\tau_{cx}}-1\right)} \mathrm{erfc}\left(\frac{v - v_0}{\Delta v}\right) \ , \tag{4.19}$$

$$f_{h\Lambda}(\Lambda) = \exp\left[\frac{-(\Lambda - \Lambda_0)^2}{\Delta\Lambda^2}\right] \ , \tag{4.20}$$

where v_c, v_0, τ_{sd}, τ_{cx}, Λ_0, and $\Delta\Lambda$ are critical velocity, neutral beam injection (NBI) velocity, slowing-down time and charge exchange time, center and width of pitch angle distribution, respectively. The velocity distribution term can be controlled by adjusting the $\frac{\tau_{sd}}{\tau_{cx}}$ ratio[72]. As τ_{cx} approaches infinity, the velocity distribution term is reduced to the slowing-down distribution.

4.4 Computational and Numerical Methods

In MEGA code, the particle-in-cell (PIC) method[73, 74, 75] is utilized for simulating the EP contributions. In this method, the particle position and velocity are continuous in phase space, while their macroscopic quantities (e.g. density, pressure, and current density) are calculated on the stationary grids. In MEGA, the EP guiding center motion is treated individually by Eqs.4.8-4.14. The electric and magnetic fields acting on the energetic particle are obtained from the MHD equations (Eqs. 4.4 and 4.6). The EP density, pressure, and current density are calculated from the moment integration.

The selection of the numerical method is important to compatibility between the numerical accuracy and the computational resources consumption. The time integration of both EP guiding center and MHD equations are calculated explicitly by the 4^{th} Runge-Kutta method. The calculation scheme of the 4^{th} Runge Kutta method is shown in Eqs.4.21 and 4.22. The right hand side of the MHD equations (Eqs.4.1-4.4) and the EP guiding center orbit equations (Eqs.4.8 and 4.12) are equivalent to "y" in Eqs.4.21. The δt is the time integration step size.

$$\begin{aligned} y_{n+1} &= y_n + \tfrac{1}{6}(k_1 + 2k_2 + 2k_3 + k_4) \\ t_{n+1} &= t_n + dt \end{aligned} \tag{4.21}$$

$$\begin{aligned} k_1 &= f(t_n, y_n)dt \\ k_2 &= f(t_n + \tfrac{1}{2}\Delta t, y_n + \tfrac{1}{2}k_1)\Delta t \\ k_3 &= f(t_n + \tfrac{1}{2}\Delta t, y_n + \tfrac{1}{2}k_2)\Delta t \\ k_4 &= f(t_n + dt, y_n + k_3)dt \end{aligned} \tag{4.22}$$

The spatial derivative terms in the MHD equations and the energetic particle guiding center orbit equations are approximated by the 4^{th} finite difference method. Let the field quantity (e.g. magnetic field) and grid width denote by "f" and "Δx", respectively, the 1^{st} and 2^{nd} order spatial derivatives at the $i-th$ grid point are represented by Eq.4.23.

$$\begin{aligned} f_i^{'} &= \tfrac{1}{12\Delta x}(-f_{i+2} + 8f_{i+1} - 8f_{i-1} + f_{i-2}) \\ f_i^{''} &= \tfrac{1}{12\Delta x^2}(-f_{i+2} + 16f_{i+1} - 30f_i + 16f_{i-1} - f_{i-2}) \end{aligned} \tag{4.23}$$

To obtain the converged results, the integration time step width (Δt), the spatial grid size (Δx), and the wave phase velocity (u) must satisfy the Courant-Friedrichs-Lewy condition[76]. The Courant-Friedrichs-Lewy condition is given by Eq.4.24. The constant "C" is a constant with an order of units. It depends on the used numerical method.

$$C \gg v\frac{\Delta t}{\Delta u} \tag{4.24}$$

$$\tag{4.25}$$

Chapter 5

Hybrid Simulation of Alfvén eigenmode in Heliotron J Plasma

5.1 Introduction

The EP-driven MHD instabilities in Heliotron J, a low magnetic shear helical-axis heliotron, has been experimentally investigated and clarified[22, 77, 23, 24, 78, 25, 79]. These studies were mainly based on the experimental measurement by the magnetic probe, density fluctuation, and scintillator lost ion probe signals. The simulation results such as MHD equilibrium, shear Alfvén continua, and electron cyclotron heating (ECH) deposition profile were utilized to support the experimental observation. These results have clarified the radial structure, time evolution, and the EP transport behaviors of the observed EP-driven MHD modes. Due to the low magnetic shear, the spatial structures of the EP-driven MHD modes in Heliotron J have a global structure. They showed that the EP-driven MHD instabilities in Heliotron J can be suppressed by the application of the electron cyclotron resonance heating (ECRH) and the non-inductive electron cyclotron current drive (ECCD). The main suppression mechanism by the application of ECCD is the increase in the local magnetic shear. The suppression of the EP-driven MHD instability by the increase in the local magnetic shear is also reproduced by FAR-3D code[39], the Landau closure model; however, the inconsistency between the experimental and simulation results in terms of the linear growth rate was observed. In addition, the EP finite orbit width effect is also neglected. This can be a potential problem in Heliotron J since the EP velocity distribution function in Heliotron J has a bump-on-tail tail structure.

Previously, the interaction between EPs and the EP-driven MHD modes in Heliotron J has not yet been thoroughly investigated. Since Heliotron J magnetic field consists of the helicity ($\mu_B/\nu_B = 1/1$), toroidicity ($\mu_B/\nu_B = 1/0$), and bumpy ($\mu_B/\nu_B = 0/1$) Fourier components, the additional resonances can potentially increase the energy transfer between EPs and MHD instabilities in Heliotron J[14, 15] and cause the formation of new toroidally asymmetric gap modes[17, 18]. The clarifications of the role of each resonance, the EP redistribution, and the interaction between shear Alfvén waves are indispensable for the development of the EP-driven MHD instability mitigation methods. The interaction between the EPs and the EP-driven MHD modes in Heliotron J will be investigated by MEGA, an EP-MHD hybrid simulation code. In this chapter, the low beta currentless discharge of Heliotron J is selected in order to simplify the calculation since the plasma current profile (I_p) cannot be measured in Heliotron J. In the high beta plasma and non-zero plasma current discharge, the formation of the lower order magnetic islands is possible. This can increase the calculation complexity because the width of the magnetic island in a lower magnetic shear device is relatively large[80, 81, 82]. The rotational transform of the Heliotron J vacuum magnetic for the low bumpiness, standard, and high bumpiness configurations are averagely around $\iota = 0.55$; therefore, the potential low order rational surfaces in the co- and counter-directions are $n/m = 1/2$ and $n/m = 4/7$, respectively.

5.2 Experimental Data

The selected discharge is #61569[25]. The information about this discharge was shown in section 3.4. This discharge was selected because the bootstrap current was minimized. In addition to the low plasma beta, the bootstrap current was found to be minimized in the low bumpiness magnetic configuration[83]. Due to the minimization of the bootstrap current, the net toroidal plasma current around the $260ms < t < 300ms$ time range is near zero. This simplifies the MHD equilibrium calculation because the net-zero flat plasma current profile assumption can be utilized. The MHD equilibrium results will be discussed in section 5.3.1.

5.3 Simulation setups

5.3.1 MHD equilibrium

The bulk plasma density and temperature profiles for #61569 discharge at t = 280 ms are shown in figure 5.1. This timing was selected because the net plasma current exhibited the minimum value (See figure 3.6c). The electron density and temperature were measured with Thomson scattering, while the bulk ion temperature was measured with change exchange recombination spectroscopy (CXRS). The ion density is assumed from the quasi-neutrality condition. The plasma beta (β_0) at the magnetic axis was 0.36%. The MHD equilibrium is calculated from the bulk plasma pressure profile, where the contribution of the EP anisotropic pressure is neglected. With the balanced NBI, low bootstrap current, and low plasma beta, zero net plasma current is an appropriate assumption for the MHD equilibrium calculation. Toroidal plasma rotation was neglected in this calculation, which is regarded as reasonable for the balanced beam injection case. The Poincaré plot, the rotational transform profile, and the magnetic field Fourier components of the MHD equilibrium are shown in figures 5.2(a-c), respectively. From the Poincaré plot and the rotational transform profile, no formation of low-order magnetic islands is observed.

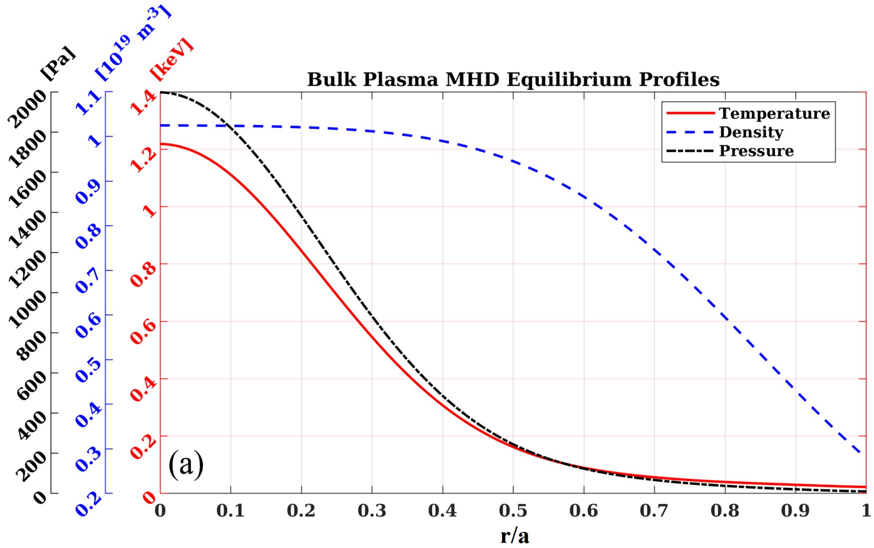

Figure 5.1: The fitted equilibrium bulk plasma density, temperature, and pressure profiles at $t = 280$ ms for the Heliotron J experiment #61569.

5.3.2 EP initial distribution function

In section 3.3, the EP velocity distribution function in the low density plasma was found to be a bump-on-tail distribution function[28]. This is caused by the substantial charge exchange loss ($\tau_{sd}/\tau_{cx} > 1$) between EPs and neutral particles, where τ_{sd} and τ_{cx} are slowing-down time and charge-exchange times, respectively. Slowing-down (τ_{sd}) and charge-exchange times (τ_{cx}) depend on both plasma density and temperature. In a higher density plasma, τ_{cx} will be longer, and the

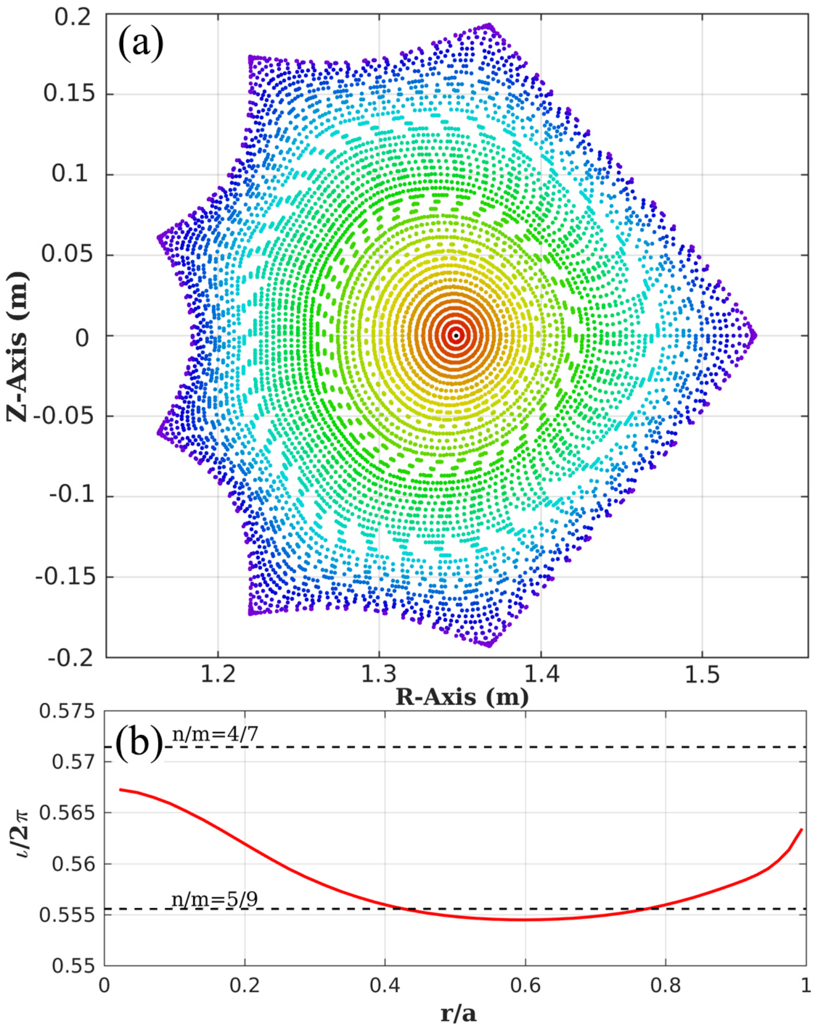

Figure 5.2: (a) Poincaré plot of the MHD equilibrium magnetic field for Heliotron J low bumpiness configuration with $\beta_0 = 0.36\%$ and (b) equilibrium rotational transform profile. The magnetic Fourier components of the equilibrium magnetic field are shown in panel (c).

transient from a bump-on-tail velocity distribution function to a slowing-down velocity distribution function can be observed. In this study, the bump-on-tail and slowing-down anisotropic velocity distribution functions are utilized to investigate the dependency of the EP-driven MHD instability on the EP velocity distribution function. The ratio of slowing-down time to charge-exchange time τ_{sd}/τ_{cx} in Eq.(4.19) is assumed to be 0 and 4 for the slowing-down and the bump-on-tail velocity distribution functions, respectively. Following the parallel neutral beam injection, the majority of the EPs are passing particles; therefore, $\Lambda_0 = 0.05$ is utilized in eq.4.20. $\Delta\Lambda = 0.25$ is assumed in order to maintain a wide distribution function. The assumed EP initial velocity distribution functions are shown in figures 5.3(a-b). The white solid lines in these figures represent constant magnetic moment (μ). Since magnetic moment is an adiabatic invariant, the EP that interacts with shear Alfvén wave will moves along the constant magnetic moment line. The effective $\frac{\partial f_{h0}}{\partial v}$ and $\frac{\partial f_{h0}}{\partial \Lambda}$ for EP are evaluated by $\frac{\partial f_{h0}}{\partial v}$ and $\frac{\partial f_{h0}}{\partial \Lambda}$ along the constant μ line. For the initial EP spatial distribution function, it is set by complementary error function, such that the spatial gradient is finite at the mode location measured with the beam emission spectroscopy[25] ($0.45 \leq r/a \leq 0.95$). The EP pressure (β_{h0}) at the magnetic axis is assumed to be 0.18%, which is half the bulk plasma beta.

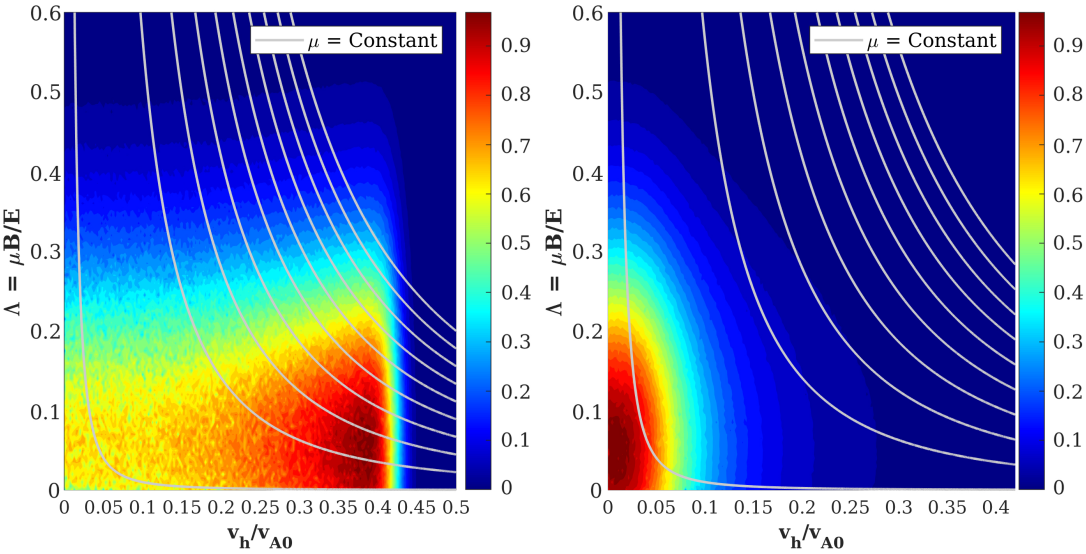

Figure 5.3: Equilibrium EP distribution function in (v, Λ) space for (a) bump-on-tail distribution function ($\frac{\tau_{sd}}{\tau_{cx}} = \infty$) and (b) slowing-down distribution function ($\frac{\tau_{sd}}{\tau_{cx}} = 4$) with $\Lambda_0 = 0.05$ and $\Delta\Lambda = 0.25$. White lines represent μ =constant.

5.3.3 Simulation parameters

In this calculation, two sets of grid resolution (R, ϕ, Z) are utilized in this study, which are (160,640,160) and (256,640,256), respectively. The finer grid is for the convergence test in section 5.4.5. The coarse grid resolution (160,640,160) is higher than the utilized value in LHD case[33] because many grids are located outside the Heliotron J vacuum vessel. The dimensions of the simulation domain are set such that the entire vacuum vessel is included. The simulation domain is (0.818 m $< R <$ 1.582 m, $0 < \phi < 2\pi$, 0 m $< Z <$ 0.762 m). The dissipation coefficients in eq.4.1-4.6 are introduced to maintain numerical stability. These coefficients allow small-scale incoherent structures to be realistically dissipated as heat[70]. For the dissipation coefficients, $5\times10^{-7}v_{A0}R_0$ is used for viscosity and diffusion coefficients, and $5\times10^{-7}\mu_0 v_{A0}R_0$ for resistivity. The values of these dissipation coefficients are higher than the experimental values to maintain numerical stability. For example, the calculated Spitzer resistivity in the core region is $4.65\times10^{-9}\mu_0 v_{A0}R_0$. It is lower than the assumed value by roughly 10^2. The number of utilized computational markers in the simulations is 1.8483×10^7, which is equivalent to 2 markers per cell on average.

5.4 Simulation Results

The MEGA was conducted for both the slowing-down and the bump-on-tail EP velocity distribution functions. For both cases, Alfvén eigenmodes (AEs) with $n/m = 2/4$ and $n/m = 1/2$ mode numbers are observed. The $n/m = 2/4$ and $n/m = 1/2$ modes are the dominant and recessive modes, respectively. From the kinetic analysis of the EP redistribution in velocity space, these modes are driven by the sideband resonances between EP and the shear Alfvén wave through the toroidicity-induced resonances. According to the $n/m = 1/2$ and $n/m = 2/4$ shear Alfvén continua, these modes are located near the extremum of the shear Alfvén continua; therefore, both simulated modes are global Alfvén eigenmodes (GAEs). These modes correspond to the peak of the calculated coherence between BES and toroidal Mirnov coil near $r/a \approx 0.4$ shown in figures 3.7(a-b). The only major difference between these two EP velocity distribution functions is the linear growth rate; therefore, only the spatial profile and time evolution of the coherent modes of the bump-on-tail velocity redistribution are discussed in sections 5.4.1-5.4.2. The EP redistribution in velocity and spatial spaces will be discussed in section 5.4.3.

5.4.1 Spatial profile and time evolution and of Alfvén eigenmodes

n/m = 2/4 Mode

The spatial structure of the radial MHD velocity of the EP-driven MHD modes in real space is shown in figure 5.4. The poloidal cross-section of the radial MHD velocity at the corner ($\phi = 0°$) and straight ($\phi = 90°$) sections are shown in panels (b) and (c), respectively. The poloidal structure of the EP-driven MHD

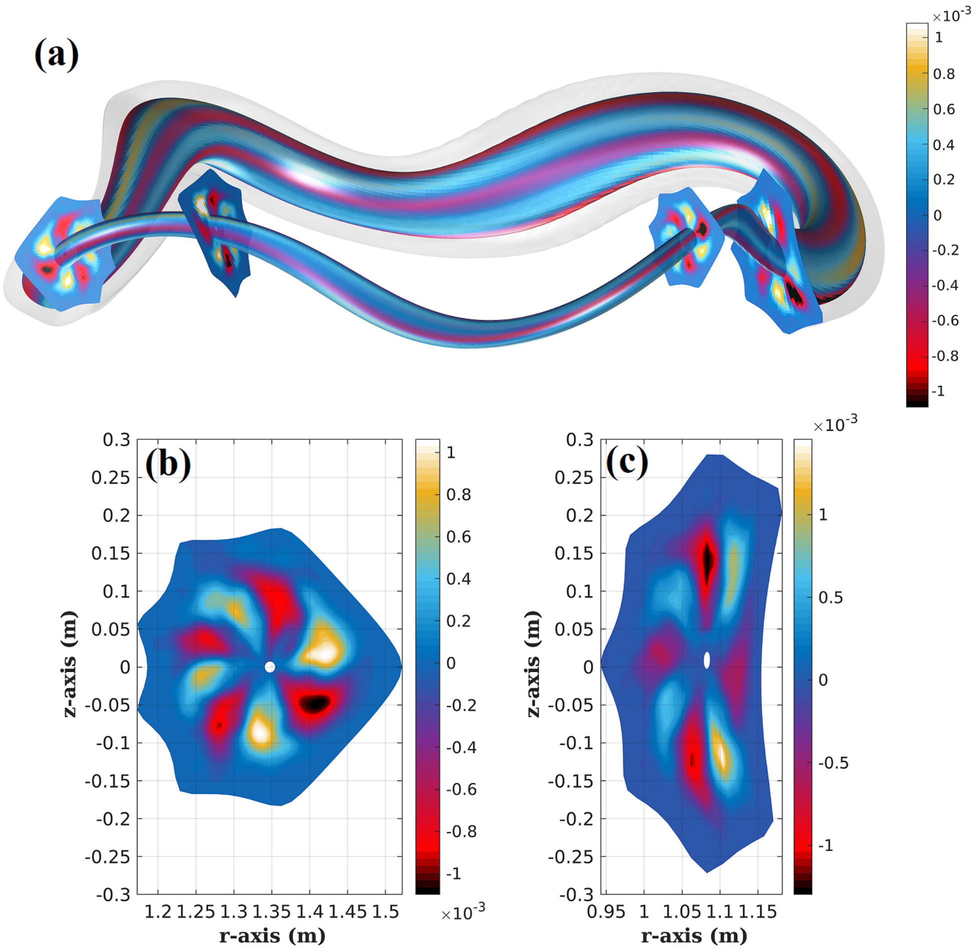

Figure 5.4: (a) Three dimensional profile of radial MHD velocity of Alfvén eigenmode at $t = 0.178$ ms in the Heliotron J plasma. Panels (b) and (c) show radial MHD velocity on poloidal cross-sections at (b) corner section and (c) straight section.

mode between the corner and straight sections are significantly different from each other. The spatial profile of the EP-driven MHD mode is complex in real space; therefore, it is efficient to analyze the spatial profile and the time evolution of the EP-driven MHD mode in the Boozer coordinates[84] system. The radial MHD velocity spatial profiles were analyzed during the linear growth phase ($t = 0.193$ ms). Only the top eight dominant harmonics are shown in figures 5.5(a-b). Only the top 3 components are labeled for clarity. From both figures 5.4 and 5.5, the most dominant harmonic is the $n/m = 2/4$ mode. The $n/m = 2/4$ mode has a single dominant harmonic, which is expected for GAE. Due to the low magnetic shear, the $n/m = 2/4$ GAE spatial profile extends from the core to the edge region. The second and third dominant harmonics are the $n/m = 2/3$ and $n/m = 2/5$. The amplitude of other toroidal mode numbers which belong to the $n = +2$ toroidal mode family are negligibly small (e.g. $n = -6, -2, 6, 10$). This indicates that the coupling of the harmonics with the same toroidal mode number through the toroidicity Fourier component ($\mu_B/\nu_B = 0/1$). The coupling with the different toroidal mode numbers through helicity ($\mu_B/\nu_B = 1/1$) and bumpiness ($\mu_B/\nu_B = 0/1$) have minor effects. The time evolution of the $n/m = 2/4$ radial MHD velocity harmonic at the location of maximum amplitude ($r/a = 0.50$) is shown in figure 5.6(a). Dark solid line, blue solid line, and dashed solid line are denoted by logarithmic, cosine, sine components, respectively. The cosine and sine components are referred to the left y-axis, while the logarithmic amplitude is referred to the right y-axis. The linear growth and the saturation of the instability can be seen. The measured linear growth rate (γ/ω_A) is 1.823×10^{-2}. Figure 5.6(b) shows the frequency evolution of n/m = 2/4 harmonic. The average frequency during the linear growth phase is 165 kHz, which is closed to the GAE frequency $140kHz$ observed in the experiment.

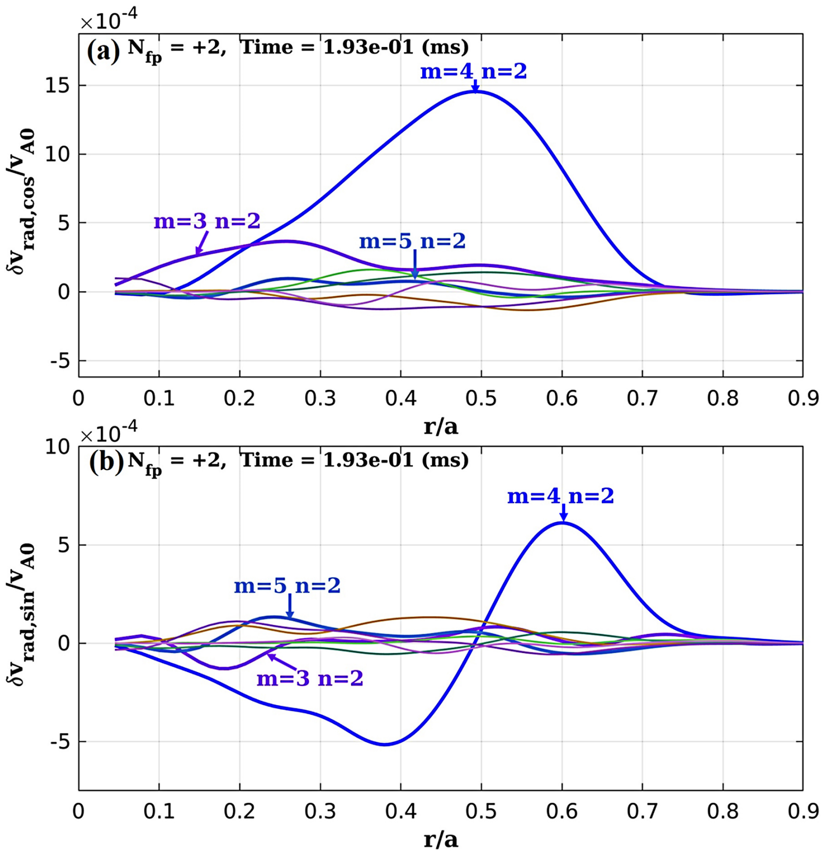

Figure 5.5: Spatial profiles of the (a) cosine and (b) sine components of radial MHD velocity harmonics at $t = 0.193$ ms. The first 3 dominant harmonics were drawn with bold solid line, and only the first 3 dominant harmonics were labeled.

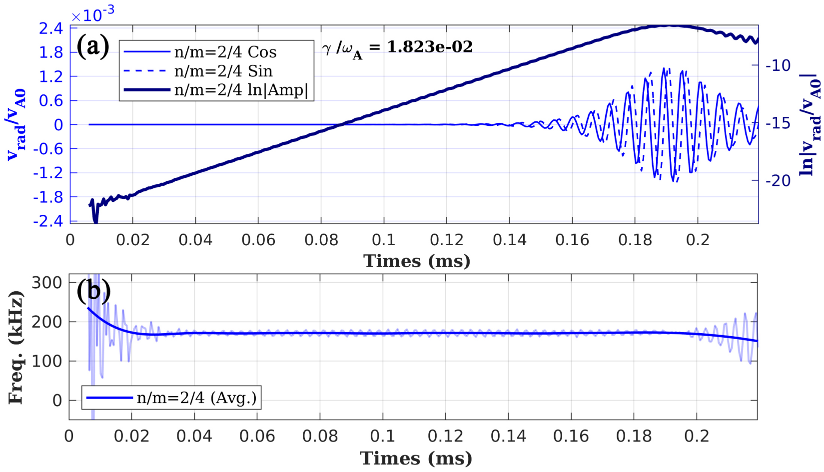

Figure 5.6: An overview of the time evolution of $n/m = 2/4$ radial velocity harmonics at $r/a = 0.5$. The upper row (a) shows the logarithmic amplitude, sine and cosine components of the mode, while the bottom row (b) shows the frequency evolution.

$\mathbf{n/m = 1/2}$ Mode

From the cross power spectral density and the beam emission spectroscopy signals in figures 3.6(a) and 3.7(a), the $n/m = 1/2$ EPM at $0.30 < r/a < 0.40$ and $0.60 < r/a < 0.70$ ranges are observed. The structure of the $n/m = 1/2$ mode is apparent when considering only the $n = +1$ toroidal mode family. The spatial profile of radial velocity for $n = +1$ toroidal mode family and the time evolution of $n/m = 1/2$ mode are shown in figure 5.7. In figure 5.7(a-b), the $n/m = 1/2$ mode showed linear growth with the frequency of around $f = 100.3$ kHz during $0.02 - 0.06$ ms (indicated by black dashed rectangle). The frequency of this $n/m = 1/2$ mode is closed to the experimental results in figure 3.6(a). After 0.06 ms, the $n/m = 1/2$ mode was obscured by the numerical noise from $n/m = 2/4$ GAE. The linear growth rate (γ/ω_A) of this $n/m = 1/2$ mode is 6.993×10^{-3}, which is lower than the linear growth rate for $n/m = 2/4$ GAE by roughly 2.6 times for the bump-on-tail velocity distribution function. Due to the significant difference in the linear growth rate between $n/m = 1/2$ mode and $n/m = 2/4$ GAE, it is difficult to analyse $n/m = 1/2$ mode. The spatial profile of the $n/m = 1/2$ mode shown in figure 5.7(c) has a single dominant poloidal harmonic. To improve the clarity of the $n/m = 1/2$ mode, the $n = +1$ toroidal mode filter is applied on the calculated $\delta P_{h\|}$ and $\delta P_{h\perp}$. In this filter, only the perturbations within the $n = +1$ toroidal mode family (e.g. $n = +13, +9, +5, +1, -3, -5$, and -9) are considered. Due to the helical geometry of Heliotron J, this filter performs Fourier decomposition along the toroidal and poloidal directions

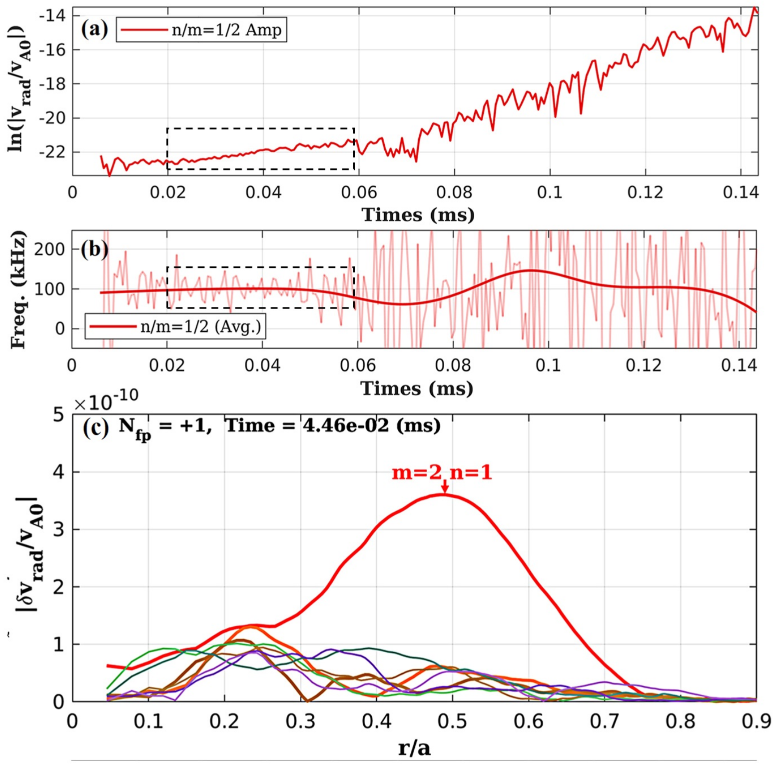

Figure 5.7: Time evolution of (a) the logarithmic amplitude and (b) frequency of n/m $= 1/2$ radial velocity harmonic at $r/a = 0.5$, and (c) the amplitude of the radial MHD velocity spatial profile for $n = +1$ toroidal mode family at $t = 4.46 \times 10^{-2}$ ms. The black dashed rectangle on (a-b) indicate $t = 4.46 \times 10^{-2}$ ms and also the interval where linear growth can be clear observed.

of Boozer coordinate. The utilization of this filter consumes high computational resources because perturbed EP pressure must be interpolated from cylindrical to Boozer grid and vice versa. The filter results are shown in figures 5.8-5.9. The peak location of the mode is at $r/a = 0.50$ or radial velocity harmonic profile in figure 5.9, while the frequency of this mode is in $f = 86.8 - 106.8$ kHz range.

5.4.2 Identification of the Alfvén eigenmodes

In this subsection, the spatial profile and the frequency of the calculated $n/m = 2/4$ and $n/m = 1/2$ modes during their linear growth phases are compared with the shear Alfvén continua. The frequency and spatial width of the $n/m = 1/2$ and $n/m = 2/4$ modes are plotted as the black horizontal line in figures 5.10(a-b), respectively. For both the $n/m = 2/4$ and $n/m = 1/2$ modes, their frequencies are close to the extremum of the $n/m = 2/4$ and the $n/m = 1/2$ continua, respectively. Along with their single poloidal dominant harmonics and global structures, it is

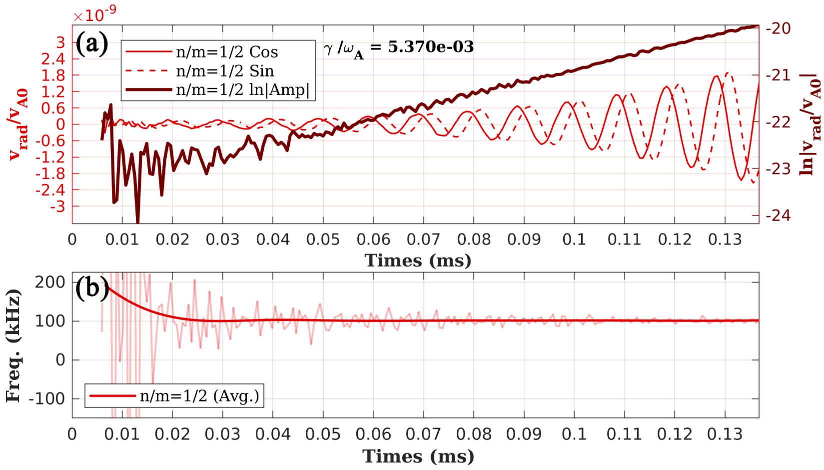

Figure 5.8: An overview of the time evolution of $n/m = 1/2$ radial velocity harmonics at $r/a = 0.5175$. The upper row (a) shows the logarithmic amplitude, sine and cosine components of the mode, while the bottom row (b) shows the frequency evolution.

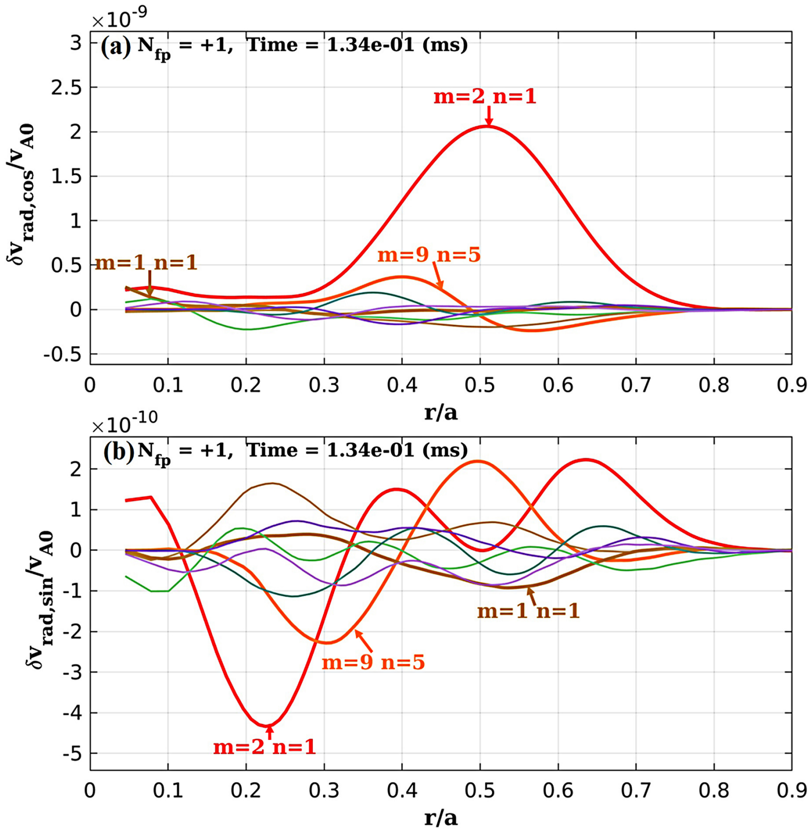

Figure 5.9: Spatial profiles of the (a) cosine and (b) sine components of radial MHD velocity harmonics at $t = 0.134$ ms for $n = +1$ toroidal mode family. The first 3 dominant harmonics were drawn with bold solid line, and only the first 3 dominant harmonics were labeled.

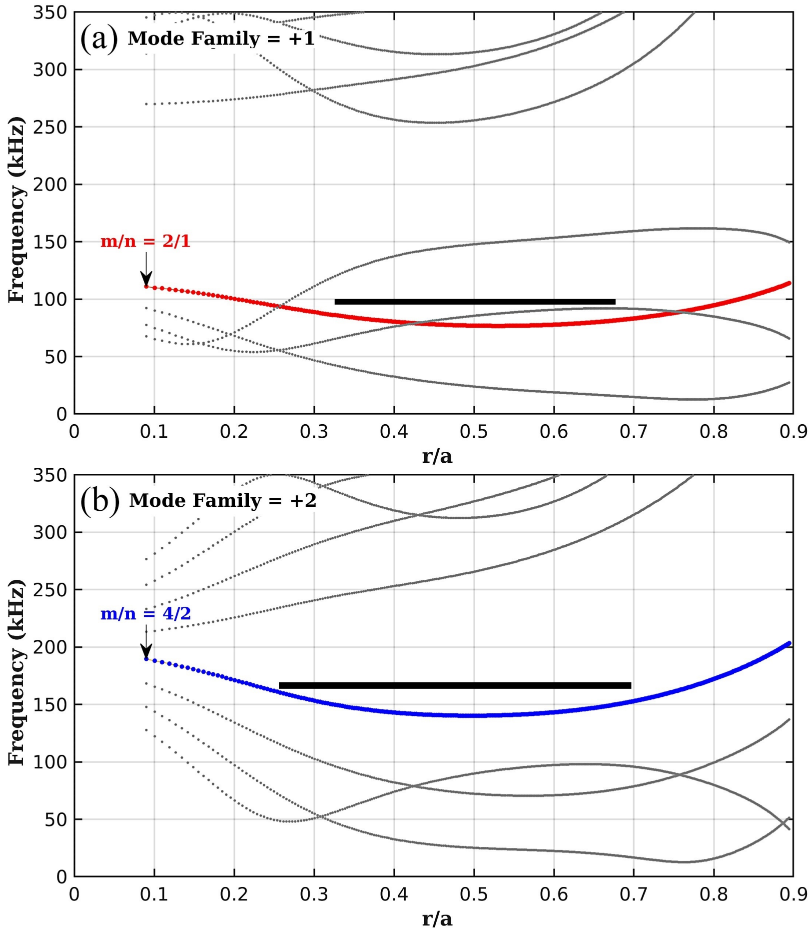

Figure 5.10: The shear Alfvén continua for (a) $n = +1$ and (b) $n = +2$ mode families for the $\beta_0 = 0.36\%$ currentless MHD equilibrium of Heliotron J in the low bumpiness configuration. The black horizontal lines in (a-b) indicate the average $n/m = 1/2$ and $n/m = 2/4$ Alfvén eigenmode frequencies in the MEGA simulation.

reasonable to conclude that these modes are GAE. From the results, the frequency in the MEGA simulation is located just above the minimum of the continua. According to the theoretical prediction, GAE (NGAE) is expected to be observed below (above) the minimum (maximum) of the shear Alfvén continuum[50]. This discrepancy might arise from the grid conversion from cylindrical coordinates to Boozer coordinates.

For the comparison with the experiment, the radial location $r/a = 0.50$ and frequency $165kHz$ of the $n/m = 2/4$ GAE in the simulation are close to that observed in the experiment (See figure 3.6, $r/a = 0.55 - 0.65$ and $f = 140kHz$)[25]. Good agreement is found for the power spectrum density of the magnetic probes signal and density fluctuation signal from beam emission spectroscopy[25](figures

3.6 and 3.7(b)). For the $n/m = 1/2$ GAE, this mode corresponds to the weak density fluctuation at $r/a \approx= 0.4$ within the $83.4kHz < f < 95.0kHz$ frequency range as shown in figure 3.7(a). The strong density fluctuation of the $n/m = 1/2$ EPM at $r/a \approx= 0.70$ is not reproduced in this calculation. To reproduce the $n/m = 1/2$ EPM at $r/a \approx= 0.70$, the EP spatial gradient at the plasma edge ($0.60 < r/a < 0.80$) and beta were increased to significantly higher values ($\beta_{h0} = 0.36\%$), but no destabilization of the $n/m = 1/2$ EPM at the plasma edge was observed. This indicates that the $n/m = 1/2$ EPM at the plasma edge requires more realistic model.

5.4.3 EP Velocity Redistribution by GAEs in Heliotron J plasma

Since Heliotron J magnetic field is composed of both the toroidal symmetric and toroidal asymmetric Fourier components, the number of available EP and shear Alfvén wave energy channels is higher than the tokamak. In this analysis, the simulated EP perturbed distribution function ($|\delta f_h|$) in velocity space is compared with the calculated EP-SAW resonant velocity from the generalized resonance condition (Eq. 5.1) for stellarator/heliotron[14, 15]. ω, m, j, μ_B, ω_θ, n, ν_B, N_{fp}, and ω_ϕ are mode frequency, poloidal mode number, order of resonance, poloidal mode number of the equilibrium magnetic field, poloidal orbit frequency, toroidal mode number, toroidal mode number of the equilibrium magnetic field, number of the equilibrium field period, and toroidal orbit frequency, respectively. Eq.(5.1) is simplified with the far-passing particle approximation ($\omega_\phi = \frac{v_\phi}{R_0}$ and $\omega_\theta = \frac{v_\phi \iota}{R_0}$) and $v = \frac{v_{||}}{\sqrt{1-\Lambda}}$ relation, where Λ is the ratio of EP perpendicular kinetic energy to total EP kinetic energy. The considered magnetic Fourier components are toroidicity, helicity, and bumpy. The simulated EP perturbed distribution function for the bump-on-tail and slowing distribution functions are shown in figures 5.11(a-b) and (c-d), respectively. The calculated resonant velocities for the toroidicity, helicity, and bumpy-induced resonances are represented by the orange, blue, and green dashed lines, respectively. The gray solid lines are the constant magnetic moment.

$$\omega - (m + j\mu_B)\omega_\theta - (n + j\nu_B N_{fp})\omega_\phi = 0, \tag{5.1}$$

For the bump-on-tail velocity distribution function (figure 5.11(a-b)), the redistributions are stronger in the high velocity region. The majority of the redistributions (resonant layers) correspond to the EP-SAW interactions via the high velocity toroidicity-induced resonances. In the $v_h/v_{A0} < 0.40$ range, the positive $\partial f_{h0}/\partial v$ exists and can potentially increase the EP drive. For the Landau damping,

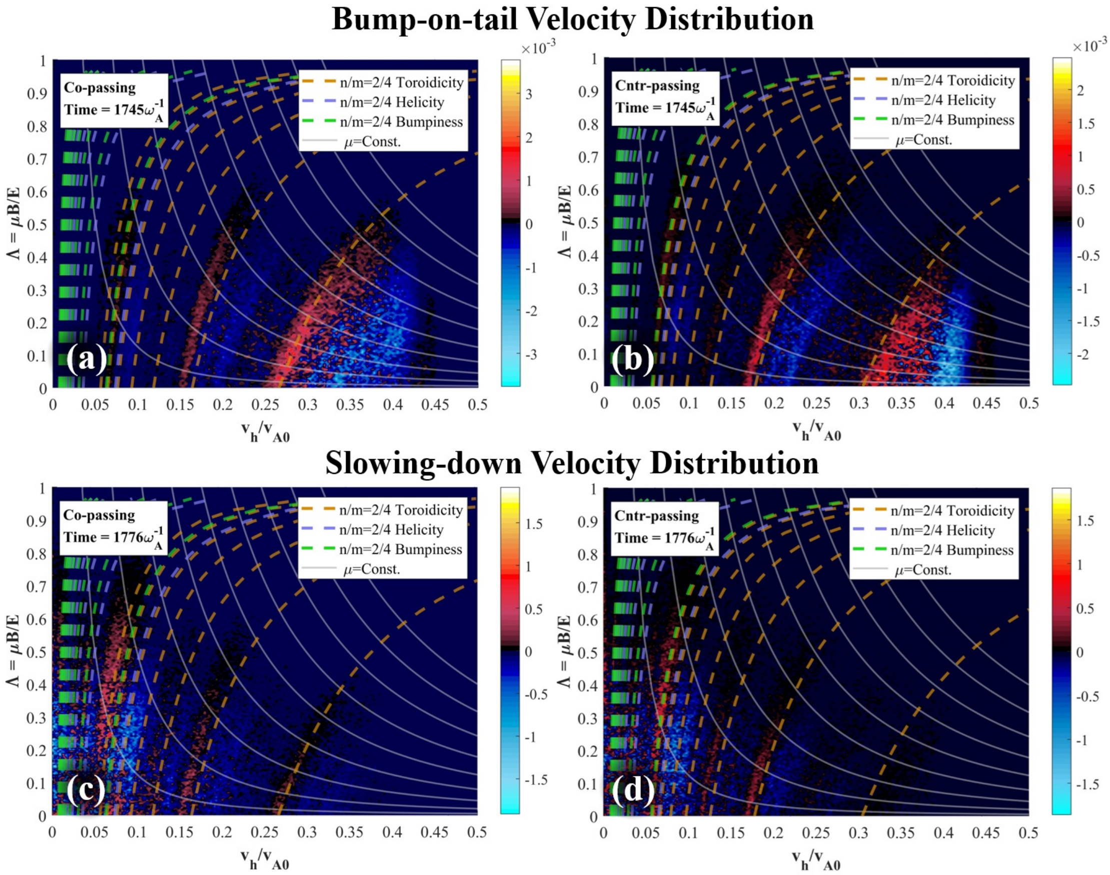

Figure 5.11: The EP velocity redistribution by the $n/m = 2/4$ GAE. The EP velocity redistribution is divided into co-passing (a and c) and counter-passing (b and d) particles. The EP velocity redistributions for the bump-on-tail and slowing-down distribution functions cases are shown in panels (a-b) and (c-d), respectively. The $n/m = 2/4$ helicity and toroidicity and bumpy-induced resonant velocity curves are plotted by the orange, blue, and green dashed lines, respectively. The white solid lines represent the constant magnetic moment lines.

it can be observed in the $v_h/v_{A0} > 0.40$ range. This is due to the sharp negative $\partial f_{h0}/\partial v$. The effect of the toroidally asymmetric resonances can be observed in the low velocity region. They are densely packed in the $0.00 < v_h/v_{A0} < 0.10$ range. Their effect is apparent in the $0.05 < v_h/v_{A0} < 0.10$ ranges for both co-passing and counter passing particles. In this range, the toroidicity, helicity, and bumpy-induced resonance layers are adjacently located. This results in the stronger redistribution than the $0.10 < v_h/v_{A0} < 0.15$ range, where only there is only a toroidicity-induced resonance.

For the slowing-down velocity distribution function (figure 5.11(c-d)), the majority of the redistributions (resonant layers) occur in the low velocity region. In this case, the role of the low velocity toroidal asymmetric resonances becomes more significant. Their additional contribution can potentially balance the negative $\partial f_{h0}/\partial v$ in the slowing-down distribution function.

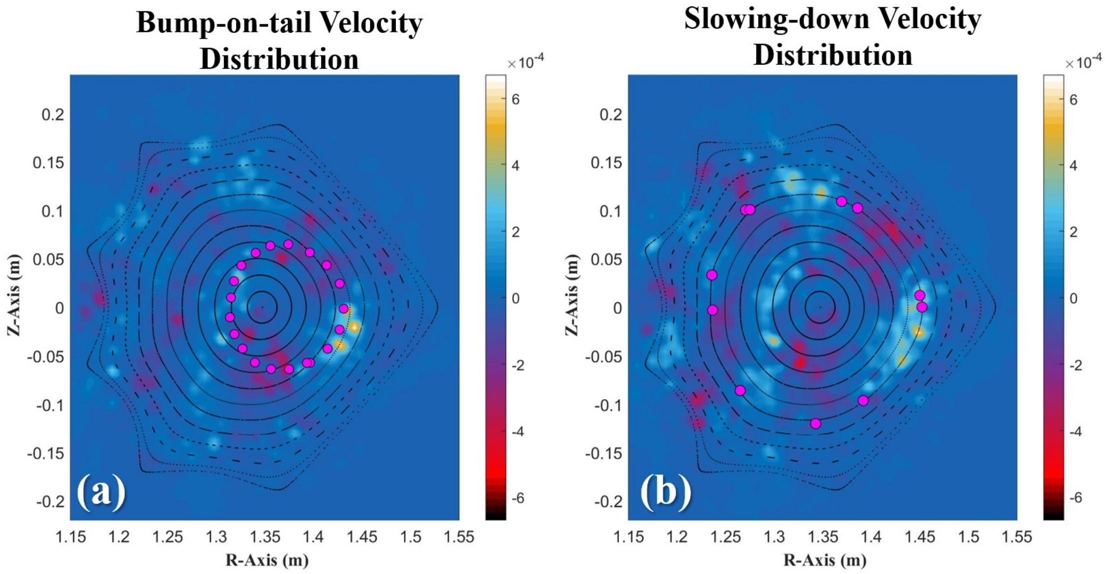

Figure 5.12: The perturbed EP parallel pressure ($\delta P_{h,\|}$) by the $n/m = 2/4$ GAE for the (a) bump-on-tail and the (b) slowing-down velocity distributions. The purple-filled circles represent the orbit of the resonant EP during the linear phase. The picked resonant particles are the EP with the largest value of $|\delta f_h|$.

The perturbed EP parallel pressure ($\delta P_{h,\|}$) also reflects the role of the initial EP velocity distribution function. $\delta P_{h,\|}$ for the bump-on-tail and slowing-down velocity distributions are shown in figures 5.12(a-b), respectively. In these figures, the orbit of the resonant EP with the largest value of $|\delta f_h|$ is plotted during the linear phase (magenta filled circles). The selected resonant EPs are the high velocity co-passing EP within the $0.25 < v_h/v_{A0} < 0.40$ range and the low velocity co-passing within the $0.05 < v_h/v_{A0} < 0.10$ range for the bump-on-tail and slowing-down distribution functions, respectively. In the bump-on-tail case, the largest $\delta P_{h,\|}$ is along the path of the high velocity co-passing resonant EP. The $\delta P_{h,\|}$ along this path has the poloidal structure ($m+j\mu_B$) of 2 which is close to the $n/m = 2/4$ GAE poloidal mode number [85]. This EP poloidal resonance number corresponds to the high velocity $n/m = 2/4$ toroidicity-induced resonance for co-passing EP ($0.25 < v_h/v_{A0} < 0.40$) in figures 5.11(a & c). According to the resonance condition, the resonant velocity for $m + j\mu_B = 3$ locates at $v_h/v_{A0} \approx 0.70$. Since, the majority of the EP velocity redistributions for the bump-on-tail case are caused by the $m + j\mu_B = 2$ resonance, $\delta P_{h,\|}$ in the other parts of the poloidal cross section are fairly small for the bump-on-tail velocity distribution function. In the slowing-down velocity distribution function case, $\delta P_{h,\|}$ in the other part becomes more apparent.

The time evolution of the logarithmic amplitude of the $n/m = 2/4$ and $n/m = 1/2$ GAEs for bump-on-tail and slowing-down velocity distribution functions are compared and shown in figures 5.13(a-b), respectively. The solid and dashed lines represent the time evolution for the bump-on-tail and the slowing-down velocity distribution functions, respectively. These results show that the linear growth rate (γ/ω_A) and the saturation amplitude for both the $n/m = 2/4$ and $n/m = 1/2$ GAEs are comparable to each other. It is noted that logarithmic amplitude $n/m = 1/2$ GAE (see figure 5.13(b)) for bump-on-tail distribution function has lower amplitude than that of the slowing-down distribution function, despite having a higher linear growth rate. This results from the lower initial amplitude.

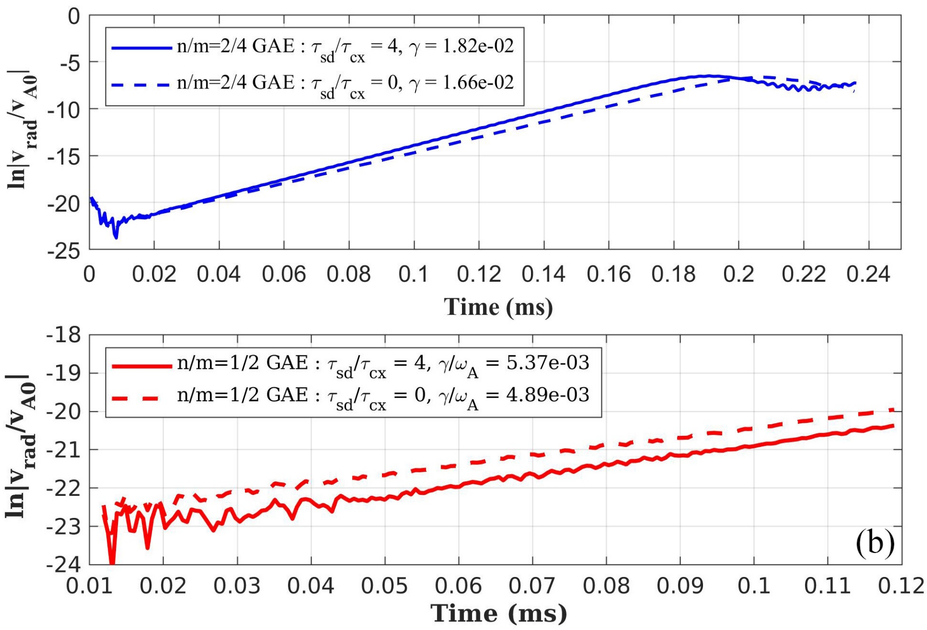

Figure 5.13: Comparison of the time evolution of (a) $n/m = 2/4$ and (b) $n/m = 1/2$ radial MHD velocity harmonic between the bump-on-tail (solid line) and the slowing-down (dashed line) equilibrium EPs distribution functions.

5.4.4 EP Spatial Redistribution by GAEs in Heliotron J plasma

The dependence of the EP spatial redistribution (transport) on the equilibrium EP velocity distribution function is analyzed. The EP density and parallel pres-

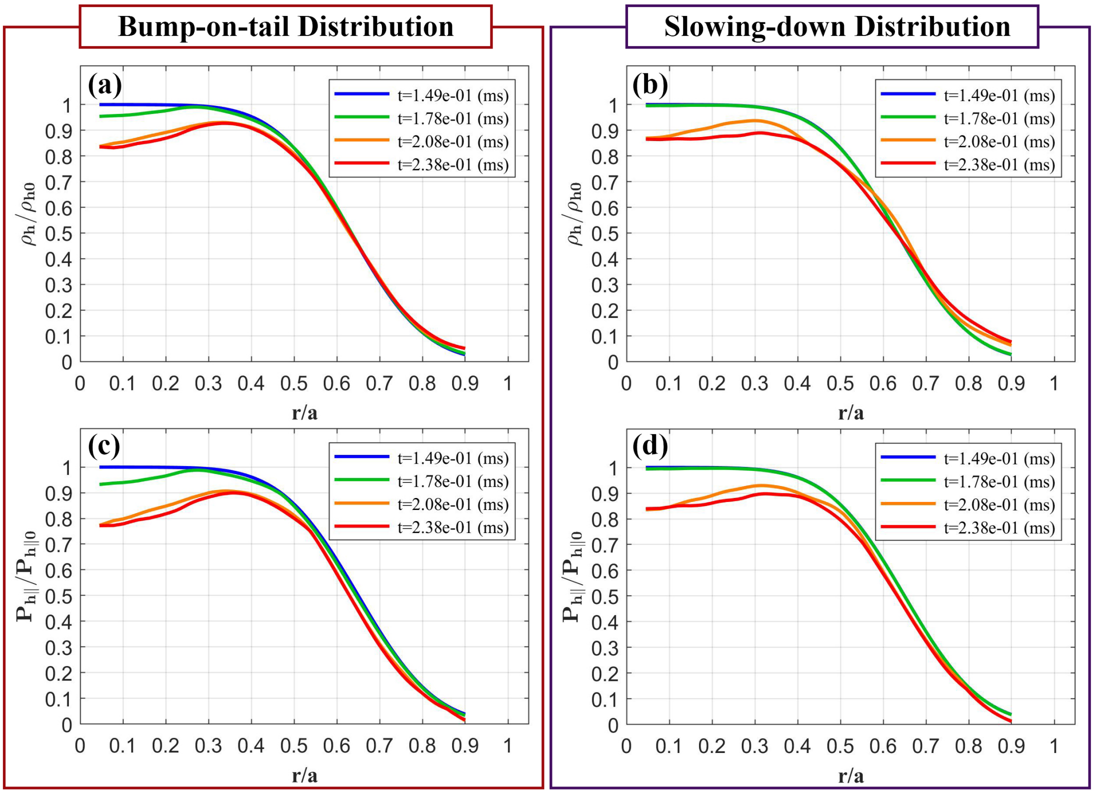

Figure 5.14: Time evolution of the EP density (a-b) and parallel pressure (c-d) profiles. (a) and (c) are the profiles for the bump-on-tail distribution function, while (b) and (d) are for the slowing-down distribution function. These profiles are normalized by equilibrium EP density and parallel pressure at the axis. The nonlinear phases start from t $\geq$ 0.193 ms and t $\geq$ 0.207 ms for the bump-on-tail and slowing down distribution functions, respectively.

sure profiles before and after the saturation of the $n/m = 2/4$ GAE are shown in figure 5.14 for the bump-on-tail and slowing-down distribution functions. It shows that the redistributed EP spatial profiles are dependent on the equilibrium velocity distribution functions. For the bump-on-tail velocity distribution function, the large reduction $(17-20\%)$ of the EP parallel pressure is observed. This results in the hollow EP density and pressure profiles[12, 86]. The cause of the hollow redistributed profile is the large orbit width of the high velocity resonant EP. The orbit of the resonant EP with the largest value of $|\delta f_h|$ for the bump-on-tail velocity distribution function case is shown in figure 5.15(a). The markers with different colors are the same EP but at different times. The blue marker represents the linear growth phase. As time progresses, the EP orbit transients from the blue (linear growth) to the red (nonlinear). This indicates that the high velocity resonant EPs transit the core region. These particles are transported by the ExB kick to the edge region. This results in the reduction of the EP density and pressure in the core region. In the edge region $(r/a > 0.7)$, the redistributed

EP pressure profile (figures 5.14(c-d)) is lower than the initial value. This is due to the finite energy transfer from the EP to the $n/m = 2/4$ GAE. In contrast, the redistributed EP density (figures 5.14(a-b)) in the edge region is higher than the initial value. For the slowing-down velocity distribution function, the flat redistributed EP density and pressure spatial profiles are observed. This supports the previous explanation where the majority of the EPs are the low velocity particles, which have smaller orbit widths. They are localized near the mode location as shown in figure 5.15(b). In addition, the EP equilibrium distribution function (f_{h0}) of the high velocity resonant EPs, which transit the core region, are lower; therefore, the high velocity EP contributions to the spatial profile redistribution is lower for the slowing-down case.

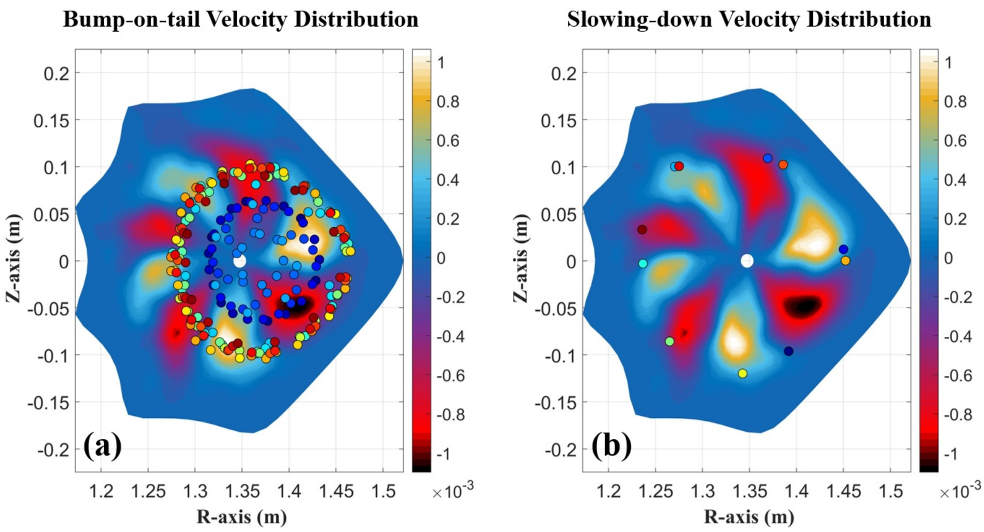

Figure 5.15: The Poincaré plot of the resonant co-passing EP with the largest value of $|\delta f_h|$ interacting with the $n/m = 2/4$ GAE. The resonant EP for the bump-on-tail and slowing velocity distribution functions are shown in panels (a) and (b), respectively. The resonant EP orbit is represented by the colored markers. The color of each marker represents time. The blue marker represents the linear growth phase. As time progresses, the EP transients from the blue (linear growth) to the red (nonlinear).

5.4.5 Numerical Convergence

Numerical convergence has been investigated with different grid resolutions. Since Heliotron J is a helical-axis device, under cylindrical grid coordinate system, many grids will represent the vacuum region; therefore, more concern is on the poloidal grid resolution. The convergence test is performed with (r,ϕ,z) = (256,640,256), a finer grid resolution. The comparison between these 2 grid resolutions are shown on Fig.5.16. The linear growth rate for (r,ϕ,z) = (160,640,160) and (256,640,256) cases are $\gamma/\omega_A = 1.82 \times 10^{-2}$ and $\gamma/\omega_A = 1.95 \times 10^{-2}$. The difference of the linear growth is less than 10%; therefore, (r,ϕ,z) = (160,640,160) is sufficient for the simulation of the $n/m = 1/2$ and $n/m = 2/4$ modes in Heliotron J.

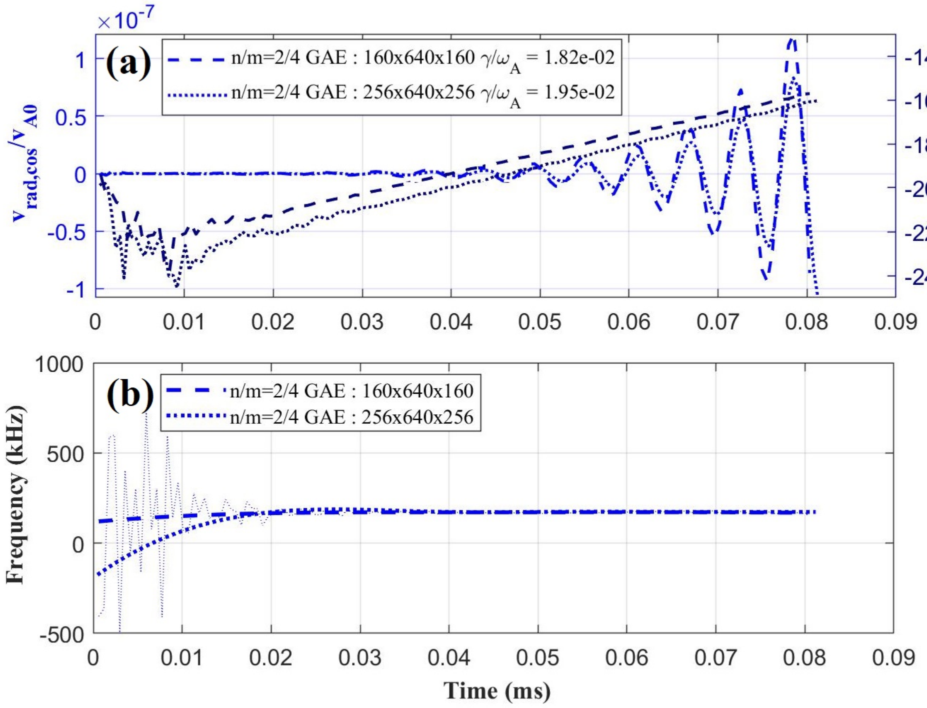

Figure 5.16: Comparison of the time evolution of n/m = 2/4 GAE (cosine, logarithmic amplitude and frequency) with two different poloidal grid resolutions (r,ϕ,z) = (160x640x160) and (256,640,256). Panel (a) shows the comparison between the time evolution of the cosine component and the logarithmic amplitude of the radial MHD velocity for two grid resolutions. The linear growth rates for these two resolutions are labeled in the legend. Panel (b) shows the time evolution of the mode frequency.

5.5 SUMMARY

The nonlinear simulations of EP-driven MHD instabilities in a helical-axis heliotron plasma were calculated for the first time with the kinetic-MHD hybrid simulation code MEGA. The GAE with $n/m = 2/4$ was successfully reproduced with the MEGA simulation based on the experimental bulk plasma temperature and density profiles. The frequency and the spatial location of the $n/m = 2/4$ GAE observed in the simulation are consistent with the experimental measurements. While the inconsistency on the radial location and the linear growth rate of the $n/m = 1/2$ mode between simulation and experiment ($n/m = 1/2$ EPM) was observed.

For the $n/m = 2/4$ GAE, we found that the 3-dimensional spatial profile of the GAE is primarily composed of $n = 2$ harmonics while the contributions from the other toroidal mode numbers of the $n = +2$ mode family such as $n = -2$ and 6 are weak. This indicates that the coupling of harmonics with the same toroidal mode numbers through toroidicity is dominant for the GAE spatial profile, and the couplings with the different toroidal mode numbers through helicity and bumpiness have minor effects. The EP transport by instabilities was calculated, where the dependency of the EP spatial profile on the equilibrium velocity distribution function was observed. The nonlinear evolution of the GAE for the bump-on-tail and the slowing-down distribution functions of EPs were compared and found to be comparable to each other.

The $n/m = 1/2$ GAE was found with a lower linear growth rate than that of the $n/m = 2/4$ GAE. The $n = +1$ toroidal mode family filter needs to be applied to observe the clear oscillation of the $n/m = 1/2$ GAE. This result is similar to the previous FAR3D simulation [31] in terms of the relative linear growth rate. This suggests that more realistic parameters and assumptions are necessary. The spatial location of the $n/m = 1/2$ GAE is different from that of the $n/m = 1/2$ EPM inferred from the experimental measurements. The possible candidate for the $n/m = 1/2$ GAE is the weak density fluctuation at $r/a = 0.45$ shown in figure 3.7(a).

We have also demonstrated that MEGA can simulate the EP-driven MHD instability in the Heliotron J. MEGA can be a useful tool for the numerical study of the interaction between EPs and MHD waves and the wave-induced EP transport in optimized heliotrons with helical-axis. The detailed analysis of the interaction between EPs and shear Alfvén waves through $\nu_B = 0$ (e.g. toroidicity) and $\nu_B \neq 0$ (e.g. helicity)-induced resonances was also reported.

Chapter 6

The Effects of the Boundary Condition on the Modelling of Energetic Particle Driven MHD modes in Heliotron J by Hybrid MHD-EP Model

6.1 Introduction

Previously the EP-driven MHD modes were simulated by MEGA, an EP-MHD hybrid simulation code; however, the $n/m = 1/2$ EP mode (EPM) at $r/a \approx 0.70$ was not reproduced. Even at the unrealistically high EP pressure and spatial gradient, destabilization of the $n/m = 1/2$ EPM was not observed. Due to the low magnetic shear of Heliotron J, low-n MHD instabilities, such as the $n/m = 1/2$ EPM and the $n/m = 2/4$ GAE, potentially have a large radial extend. It is possible that even a low-n MHD instability at the middle of the plasma ($0.40 < r/a < 0.50$) can cause a finite radial displacement at the LCFS. In the field of EP-driven MHD instability simulation, it is normally assumed that the plasma is surrounded by the perfectly conducting wall. In this context, this assumption is called the "fixed boundary" condition. Under this assumption, the plasma displacement at the LCFS is set to zero. The fixed boundary condition was also applied in our previous work in chapter 5[61]. Under this boundary condition, only the $n/m = 2/4$ and the weak $n/m = 1/2$ global Alfvén eigenmodes (GAEs) at $0.40 < r/a < 0.50$ were reproduced. The $n/m = 1/2$ EPM at $r/a > 0.70$, which is the most unstable mode, was not reproduced by any means. This $n/m = 1/2$ EPM can likely cause the finite plasma displacement at the LCFS. This statement is supported by (1) the location of the mode, (2) the low toroidal mode number, and (3) the low magnetic shear of Heliotron J. Under these explanations, the fixed boundary condition is not valid for the modeling of any low-n MHD instabilities in Heliotron J, a low magnetic shear device. The plasma displacement at the LCFS induced by the EP-driven MHD instability can be considered with the free boundary condition. With this boundary condition, the perfectly conducting wall is placed at the actual location of the Heliotron J vacuum vessel. The vacuum region is introduced between the plasma and the perfectly conducting wall regions. The MHD plasma on the plasma-vacuum boundary can be displaced from the equilibrium position by the MHD instability.

The role of the free boundary condition on the toroidal Alfvén eigenmode (TAE) stability was investigated by EY Chen *et al*[43] with AEGIS, an ideal MHD analysis code. Their results show that the frequency of the ideal MHD mode decreases with the increase of the perfectly conducting wall distance from the LCFS. The stability of the eigenmode is affected by the change in the continuum damping through the frequency shift. In the strongly shaped plasma, the effects of the free boundary condition are enhanced. The contribution of the EP kinetic in the free boundary simulation was studied by S.X. Yang *et al*[44] with MARS-K, a hybrid MHD-EP code on HL-2A plasma[87]. In contrast to Ref.[43], the resistive wall assumption was utilized in place of the perfectly conducting wall assumption. It showed that the linear growth rate of the TAE increased as the distance between the LCFS and resistive wall position (w_{wall}) increased. However, at a certain distance, the linear growth rate converged to the "no wall limit" value, where further increment in w_{wall} has no significant effect. The effects of the free boundary condition in stellarator/heliotron configurations have not yet been studied. Since Heliotron J has low magnetic shear and strongly shaped plasma, the boundary condition can have a significant impact on low-n MHD instabilities.

6.2 Simulation setups

The referred experimental discharge and the MHD equilibrium are the same as chapter 5. The major differences are on the EP initial distribution function and the boundary conditions. For the cylindrical grid resolution, $(R, \phi, Z) = (160, 640, 160)$ is utilized in this study. It was confirmed in chapter 5 that (R, ϕ, Z) $= (160, 640, 160)$ is sufficient for the modelling of low-n MHD instabilities in Heliotron J. The simulation domain is (0.818 m $< R <$ 1.582 m, $0 < \phi < 2\pi$, 0 m $< Z <$ 0.762 m).

6.2.1 Boundary conditions

The simulation domain is divided into 3 regions: (1) plasma, (2) vacuum, and (3) perfectly conducting wall. The comparison between the fixed and free boundary simulation domains is shown in figures 6.1(a-b), respectively. These figures show the poloidal cross-section of the plasma resistivity, where the black solid line with circular marker indicates the perfectly conducting wall. The perfectly conducting wall in the free boundary simulation corresponds to the actual Heliotron J vacuum vessel. The plasma resistivity (η) in the plasma, vacuum, and perfectly conducting wall regions are $5 \times 10^{-7}\mu_0 v_{A0} R_0$, $1 \times 10^{-4}\mu_0 v_{A0} R_0$, and 0.00, respectively. In the fixed boundary simulation (figure 6.1(a)), only the plasma and the perfectly conducting wall exist, while the vacuum region is introduced only in the free boundary simulation (see figure 6.1(b)). Under these simulation setups, the plasma displacement in the fixed and free boundary simulations is set to zero at the LCFS and the vacuum-wall interface, respectively. In the free boundary simulation, the plasma at the plasma-vacuum interface (LCFS) can be freely displaced by instability.

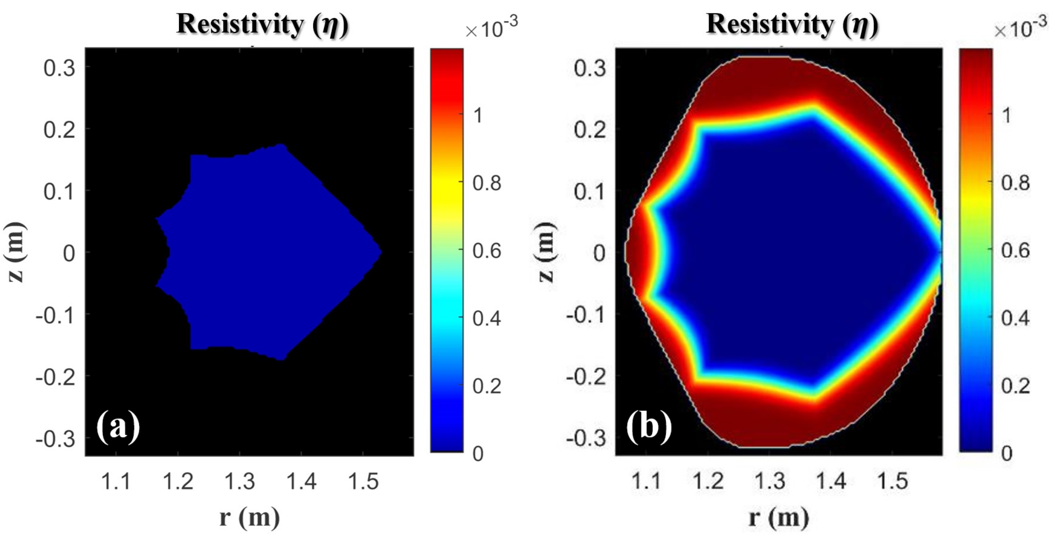

Figure 6.1: The poloidal cross-sections of the plasma resistivity (η) for the fixed (a) and free (b) boundary simulations. The domains can be classified into 3 regions: vacuum vessel (perfectly conducting wall), vacuum, and plasma. These regions are represented by red, black, and blue colors, respectively. At the vacuum-plasma interface of the panel (b), the gradient of the plasma resistivity exists.

6.2.2 Initial EP distribution

In the study of the EP-driven MHD mode with the free boundary simulation, the initial EP distribution function (∇f_{h0}) was modified from chapter 5 to maintain numerical stability and clarify the free boundary effect. In this chapter, the standard value of the EP beta ($\beta_{h0,0}$) at the magnetic axis is reduced from $\beta_{h0,0} = 0.18\%$[61] to $\beta_{h0,0} = 0.11\%$. The reason is that the calculated linear growth rate from the free boundary simulation is much higher than the fixed boundary result. This will be shown in the following section. In addition, this reduction makes the simulation parameters more realistic. For the initial EP spatial distribution, two different spatial profiles are utilized. They are shown in figure 6.2(a) as $\nabla f_{h0,r60}$ and $\nabla f_{h0,r50}$. The maximum EP spatial gradient ($\nabla f_{h,0}$) for $\nabla f_{h0,r50}$ and $\nabla f_{h0,r60}$ are placed at the middle ($r/a \approx 0.50$) and the edge ($r/a \approx 0.60$) of the plasma, respectively. For the $\nabla f_{h0,r50}$ case, the maximum EP spatial gradient is located at the extremum of both the $n/m = 1/2$ and $n/m = 2/4$ shear Alfvén

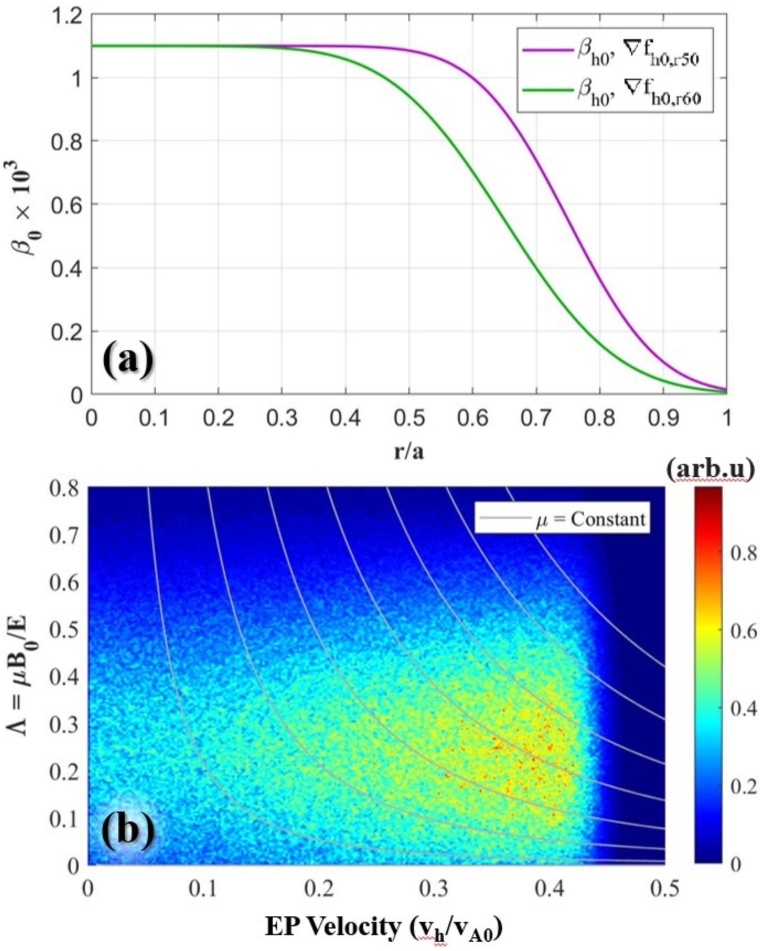

Figure 6.2: (a) Initial EP spatial and (b) velocity distributions. White lines in panel (b) represent μ =constant.

continua. This distribution ($\nabla f_{h0,r50}$) will be utilized only in the section 6.3. The free boundary effect and its dependency on the mode number can be easily investigated. For $\nabla f_{h0,r60}$, the maximum EP spatial gradient (∇f_{h0}) corresponds to the radial position of the experimentally observed $n/m = 1/2$ EPM. This case will be discussed in section 6.4 where the experimentally observed $n/m = 1/2$ EPM will be reproduced. Lastly, only the bump-on-tail velocity distribution will be investigated in this chapter. Since the role of the EPs in different regions of the velocity space has been clarified in chapter 5. This initial EP velocity distribution is shown in figure 6.2(b).

6.3 $\nabla f_{h0,r50}$: Effect of Boundary Condition on the Properties of EP-driven MHD mode in Heliotron J

In this section, the roles of the boundary condition on the linear properties of the EP-driven MHD mode are investigated. The utilized EP initial spatial distribution (f_{h0}) is the $\nabla fh0, r50$ case shown in figure 6.2(a), where the sharp EP spatial gradient is placed at the extremum of both the $n/m = 1/2$ and $n/m = 2/4$ shear Alfvén continua. Both the $n/m = 1/2$ and $n/m = 2/4$ GAEs are expected to be simultaneously destabilized under this setup. Since both modes are located nearly at the same radial location, the dependency of the free boundary effect on the mode number can be investigated. The comparison of the linear properties of the $n/m = 1/2$ and $n/m = 2/4$ GAEs between free and fixed boundary conditions is discussed in subsection 6.3.1. The dependencies of the linear growth rate (γ/ω_A), the frequency, and the radial location of the EP-driven MHD mode on the perfectly conducting wall location are discussed in subsection 6.3.2. Lastly, the underlying effect of the free boundary condition will be clarified in subsection 6.3.3.

6.3.1 Effect on spatial profile, linear growth rate, and frequency

The radial MHD velocity (δv_{rad}) profiles from the fixed and free boundary simulations are shown in figures 6.3(a-b) and (c-d), respectively. The black dashed line represents the EP pressure. The amplitude of the radial MHD velocity and the EP pressure are referred to the left and right vertical axes, respectively. The time evolution of the $n/m = 1/2$ and $n/m = 2/4$ radial MHD velocity harmonics are shown in figures 6.4(a-b), respectively. For the fixed boundary simulation, only the $n/m = 2/4$ GAE emerges as the dominant mode (figure 6.3(b)). This mode has an averaged frequency of 158.85 kHz. The linear growth rate (γ/ω_A) of the $n/m = 2/4$ GAE is 4.237×10^{-3}. This result is similar to the previous results in section 5.4[61]. According to section 5.4.1, the $n/m = 1/2$ GAE can only be observed with the application of the $n_f = +1$ toroidal mode family filter. The radial width and the frequency of the $n/m = 2/4$ GAE from the fixed boundary simulation are compared to its shear Alfvén continuum. It is denoted by the unfilled triangles in figure 6.5(b).

Significant differences are observed in the free boundary simulation. In the free boundary simulation, the $n/m = 1/2$ GAE emerges as the dominant mode instead of the $n/m = 2/4$ GAE. The coherent structure of the $n/m = 2/4$ GAE is still observable but at a lower amplitude. Both the $n/m = 1/2$ and the $n/m = 2/4$ GAEs have a global structure and a single dominant poloidal harmonic. They are located at the same radial location ($r/a \approx 0.50$) which correspond to the extremum of both the $n/m = 1/2$ and $n/m = 2/4$ shear Alfvén continua (see figure 6.5). This information is sufficient to conclude that these two modes are GAEs. The radial width and the frequency of the $n/m = 1/2$ and $n/m = 2/4$ GAEs from the fixed boundary simulation are compared to their shear Alfvén continua. They are denoted by the filled triangles in figures 6.5(a-b). In terms of the spatial profile, the free boundary simulation yields a broader mode spatial profile. The location of the mode peak is also slightly shifted radial outward. This is apparent from the comparison of the fixed and free boundary simulation results of the $n/m = 2/4$ GAE. In terms of the time evolution, the increases in γ/ω_A for both the $n/m = 1/2$ and the $n/m = 2/4$ GAEs in the free boundary simulation are observed. The linear growth rates for the $n/m = 1/2$ and $n/m = 2/4$ GAEs increase from $\gamma/\omega_A =$ "Unobservable" to $\gamma/\omega_A = 1.032 \times 10^{-2}$ and from $\gamma/\omega_A = 4.237 \times 10^{-3}$ to $\gamma/\omega_A = 7.379 \times 10^{-3}$, respectively. The change in γ/ω_A is higher for the $n/m = 1/2$ GAE than the $n/m = 2/4$ GAE. This indicates that the effect of the free boundary condition is stronger for a low-n MHD mode where mode width decreases as the mode number increases. It is also supported by the fact that both of these modes are located at the same radial location.

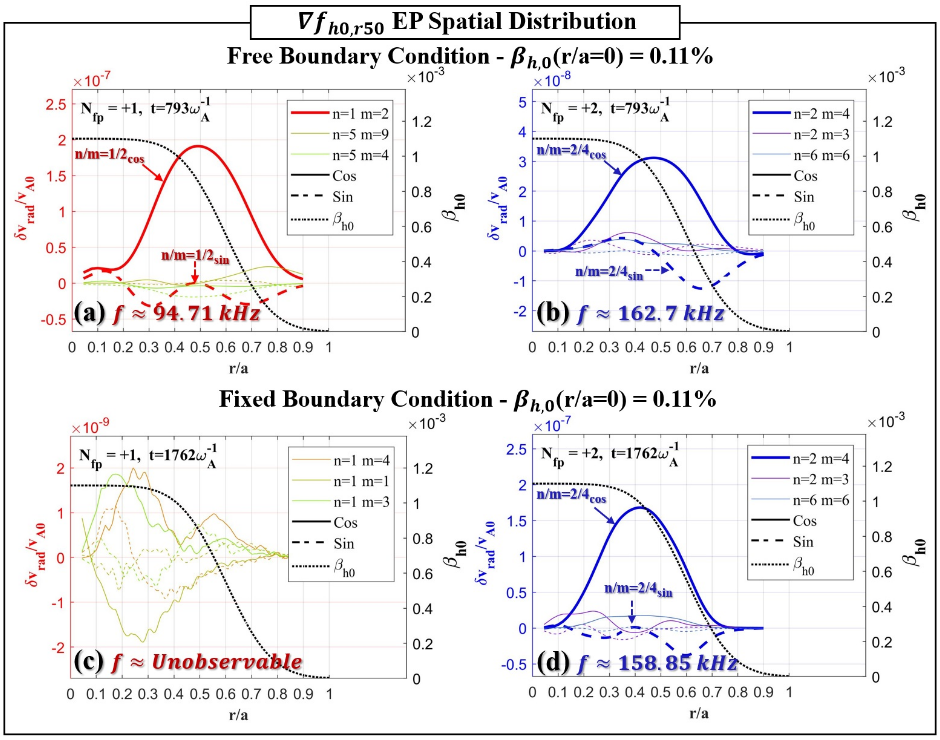

Figure 6.3: The spatial profiles of radial MHD velocity harmonic for the fixed and free boundary "$\nabla f_{h0,r50}$" simulations. The simulation results for the free and fixed boundary cases are shown in panels (a-b) and (c-d), respectively. Panels (a) and (c) show $N_f = +1$, and panels (b) and (d) show $N_f = +2$ toroidal mode families.

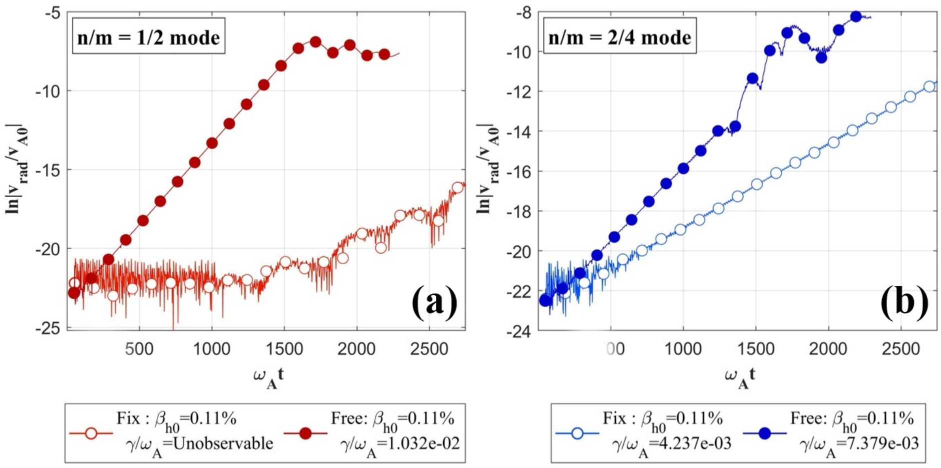

Figure 6.4: The time evolution of the logarithmic amplitude of radial MHD velocity harmonic for "$\nabla f_{h0,r50}$" at the location of maximum amplitude. Panels (a) and (b) represent the $n/m = 1/2$ and the $n/m = 2/4$ modes, respectively. The fixed and free boundary simulation results are denoted by the unfilled and filled markers, respectively. For the case where linear growth of the mode cannot be observed, γ/ω_A is set to "Undefined".

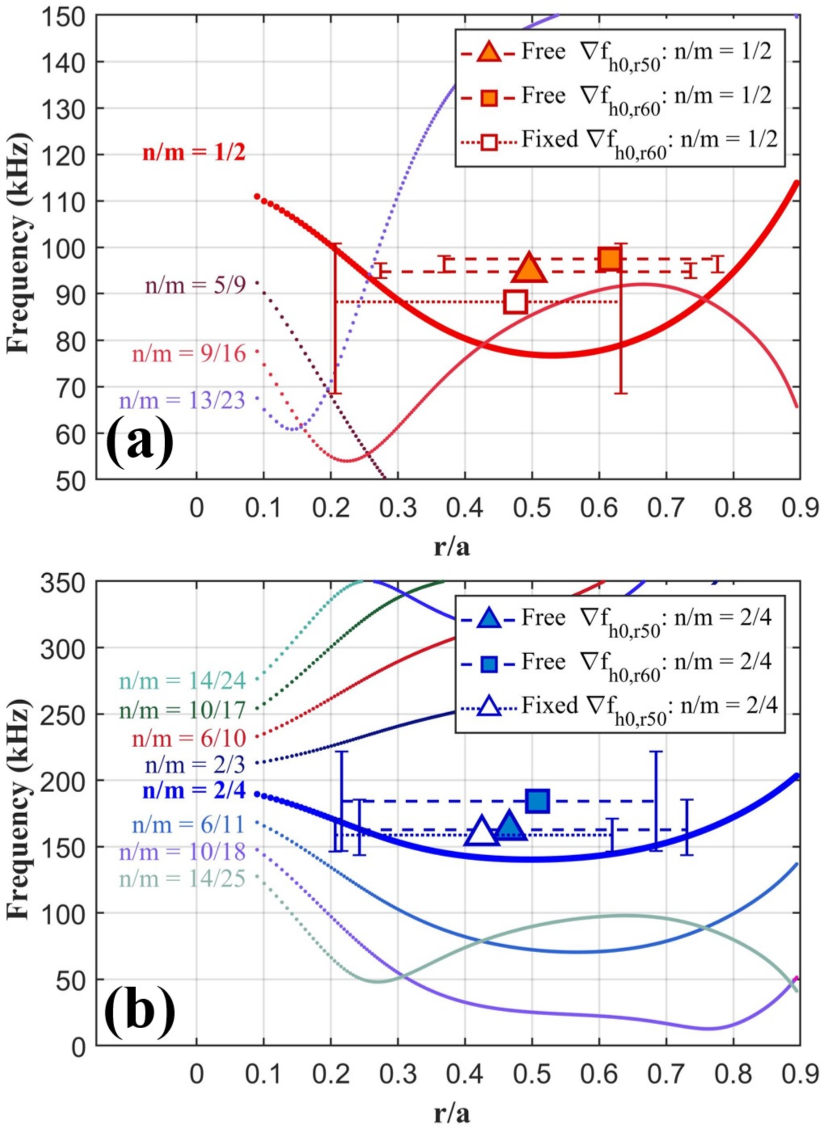

Figure 6.5: The shear Alfvén continua for the low beta ($\beta_{b0} = 0.37\%$) currentless plasma of Heliotron J: (a) $n_f = +1$ and (b) $n_f = +2$ toroidal mode families. The $\nabla f_{h0,r50}$ and $\nabla f_{h0,r60}$ are represented by the triangle and square, respectively. The frequencies and spatial locations of the $n/m = 1/2$ and the $n/m = 2/4$ modes for the free and fixed boundary simulations are represented by the filled and unfilled markers, respectively. The large and small markers represent the radial location of the peak and the edge of the radial MHD fluctuation profile, respectively. The vertical solid lines represent the deviation of the calculated frequency.

6.3.2 Dependency on perfectly conducting wall position

In this section, the dependency of the linear growth rate, the frequency, and the radial location of the EP-driven MHD mode on the perfectly conducting wall position will be investigated. The set of artificially perfectly conducting walls with different radial location is created. These artificially created walls are based on the LCFS and the actual Heliotron J vacuum vessel. The radial step size between each artificially created conducting wall is based on the poloidal direction with respect to the magnetic axis. These artificially created walls are denoted by the averaged perfectly conducting wall distance from the LCFS ($\overline{w}_{wall}$). It is averaged because of the non-uniformity of Heliotron J plasma geometry. These walls are shown in figure 6.6. The lower and the upper limits of $\overline{w}_{wall}$ are $0.00m$ and $0.125m$, respectively. $\overline{w}_{wall} = 0.00m$ represents the normal fixed boundary condition where the plasma is surrounded by the perfectly conducting wall. For $\overline{w}_{wall} = 0.125m$, the boundary takes shape of the actual Heliotron J vacuum vessel (Similar to the free boundary results in section 6.3.1). During this scan, the normalization factor for the EP initial distribution function is kept constant.

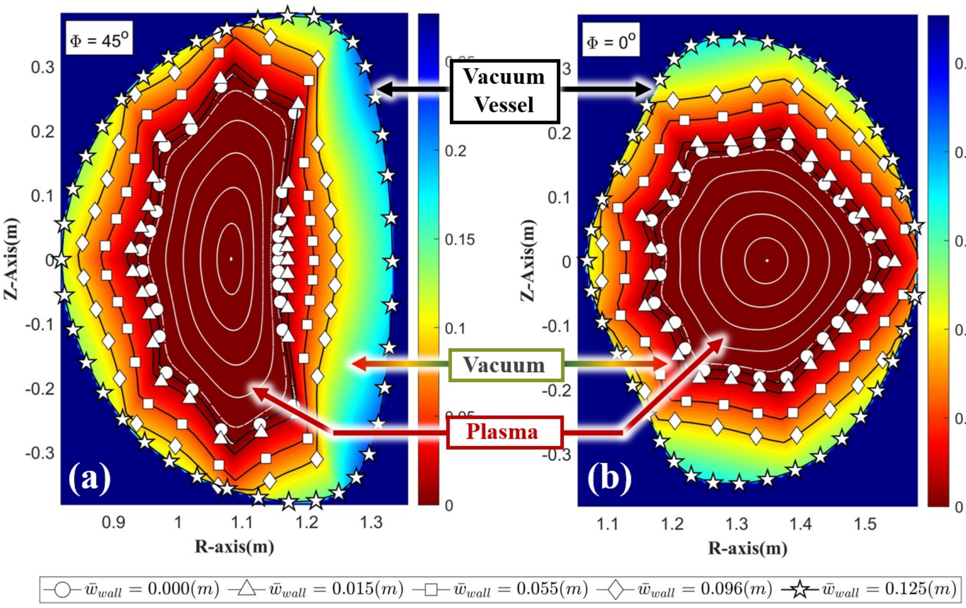

Figure 6.6: The scanned artificially created perfect conducting walls. Panels (a) and (b) show the poloidal cross-sections at the straight and corner sections, respectively. The scanned walls are differentiated by their averaged distance between the wall and LCFS ($\overline{w}_{wall}$). The $\overline{w}_{wall} = 0.00m$, $0.0015m$, $0.055m$, $0.096m$, and $0.125m$ walls are denoted by circular, triangular, square, diamond, and star markers, respectively. The contour also represents the local distance between the wall and LCFS. The white solid lines in the plasma region represent the magnetic flux surfaces.

The dependency of γ/ω_A on $\overline{w}_{wall}$ is shown in figure 6.7(a). For the small $\overline{w}_{wall}$, γ/ω_A of all coherent modes increase with $\overline{w}_{wall}$. After the finite increase in $\overline{w}_{wall}$, γ/ω_A approaches the "no wall limit" value. The zero linear growth rate for the $n/m = 1/2$ GAE at $\overline{w}_{wall} = 0.00$ m indicates that the linear growth is not observable. This means either the mode linear growth rate is lower than the total damping rate or the mode linear growth is obscured by the numerical noises from other faster-growing modes. In figure 6.7(a), the increase in γ/ω_A for the $n/m = 1/2$ GAE is higher than the $n/m = 2/4$ GAE. The stronger dependency for the $n/m = 1/2$ GAE is due to the lower mode number.

The dependency of the mode frequency is shown in figure 6.7(b-c). The slight increases of the mode frequencies with respect to $\overline{w}_{wall}$ are observed. This contradicts with the results in Ref.[43, 44]. For the $n/m = 1/2$ mode, it can be explained by the outward radial shift of the mode. According to figure 6.7(d), as $\overline{w}_{wall}$ increases the peak location of the modes moves closer to the LCFS and settle at the "no-wall limit." According to the $n/m = 1/2$ shear Alfvén continuum, the frequencies of these shear Alfvén continua slightly increase as the modes move away from their extrema. However, this explanation does not valid for the $n/m = 2/4$ GAE. In addition, the change in the frequency with respect to radial position for both the $n/m = 1/2$ and $n/m = 2/4$ shear Alfvén continua cannot fully cover the change in the frequency of the $n/m = 1/2$ and $n/m = 2/4$ GAEs in the free boundary simulation.

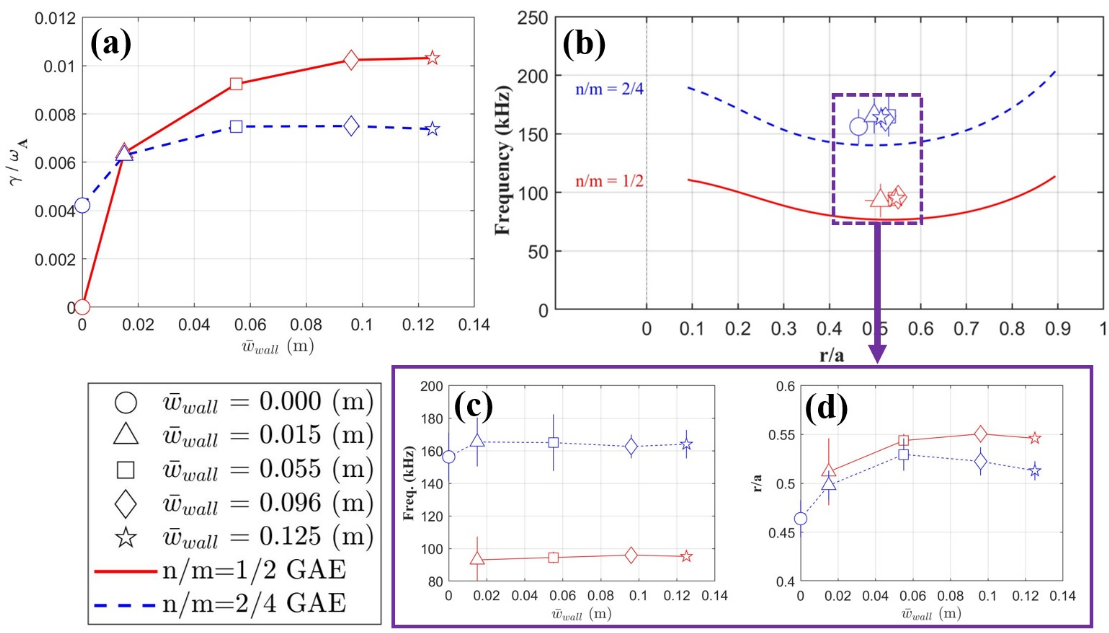

Figure 6.7: The dependency of the linear properties of the $n/m = 1/2$ and $n/m = 2/4$ GAEs on $\overline{w}_{wall}$. (a) linear growth rate, (b) the comparison between the mode frequency and the peak location of the mode with the $n/m = 1/2$ and $n/m = 2/4$ shear Alfvén continua, (c) the mode frequency, and (d) the radial location of the mode.

6.3.3 Effect on EP driving and MHD dissipation rates

The presented results in subsections 6.3.1 and 6.3.2 indicate that the boundary condition at the LCFS has a significant impact on the spatial profile and γ/ω_A of the low-n MHD instability in Heliotron J. However, the underlying mechanism of the enhancement in γ/ω_A in the free boundary simulation has not yet been clarified. To clarify the underlying physical mechanism of the free boundary condition effects, The differences in the EP driving (γ_h) and MHD dissipation (γ_d) rates between the fixed and free boundary simulations are analyzed. These 2 values can be calculated from the EP energy transfer ($-d\Delta E_h/dt$) and the MHD thermal fluctuation energy ($d\Delta E_T/dt$) rates. These rates are normalized by the total Alfvén eigenmode energy (ΔE_{AE}). These values are calculated by the spatial integration of the EP energy transfer, MHD kinetic energy, and MHD thermal en-

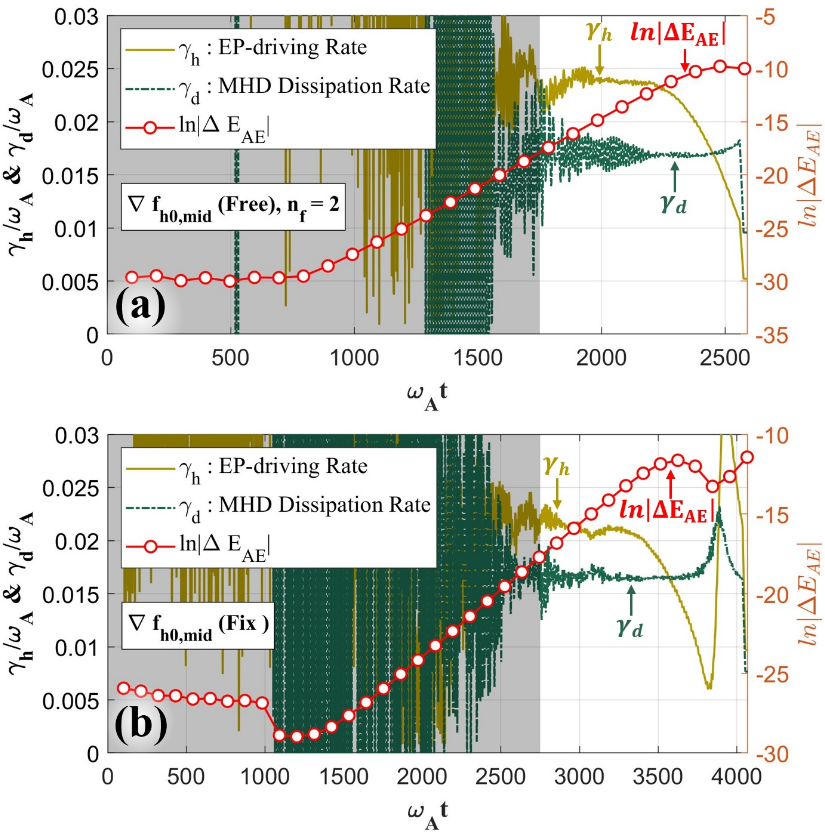

Figure 6.8: The time evolution of γ_h (yellow solid line), γ_d (green dash-dotted line), and ΔE_{AE} (red solid line with unfilled circles). γ_h and γ_d are referred to the left vertical axis, while ΔE_{AE} is referred to the right vertical axis. The simulation results for the free and fixed boundary $\nabla f_{h0,r50}$ cases are shown in panels (a-b), respectively. For the free boundary $\nabla f_{h0,r50}$ case, $n_f = +2$ toroidal mode filter is applied.

ergy throughout the simulation domain. The normalized $-d\Delta E_h/dt$ and $d\Delta E_T/dt$ are proportional to the EP driving rate (γ_h) and the MHD dissipation rate (γ_d), respectively. In this analysis, only the $n/m = 2/4$ GAE in the $\nabla f_{h0,r50}$ case was analyzed because the linear growth of the $n/m = 2/4$ GAE is observable in both the free and fixed boundary simulations. The contribution of the $n/m = 1/2$ GAE from the free boundary simulation must be filtered out for the free boundary case because its contribution can affect the calculated γ_h and γ_d. The free boundary $\nabla f_{h0,r50}$ case is re-simulated with the $n_f = +2$ toroidal mode filter. The results are shown in figure 6.8. γ_h (yellow solid line) and γ_d (green dash-dotted line) are referred to the left vertical axis. The logarithmic time evolution of ΔE_{AE} (red solid line with filled circles) is also shown. It is referred to the right vertical axis. It can be seen that the Alfvén eigenmode saturates when γ_h is equal to γ_d ($\omega_A t \approx 2450$). The major difference between the free and fixed boundary simulations is γ_h. As expected, the boundary condition has a weak effect on the MHD part of the Alfvén eigenmodes because they are internal modes. This suggests that the free boundary condition enhances the EP and shear Alfvén wave interaction. The EP driving rate (γ_h) is enhanced through the broadening of the mode spatial profile. This allows more EPs to interact with the shear Alfvén wave, and thus, γ_h increases. The outward radial shift of the mode can also enhance γ_h if the high velocity resonant EPs can efficiently interact with the mode in the peripheral region. This will be further verified in section 6.4.3 by the kinetic analysis of the EP redistribution in spatial and velocity spaces. In addition, the strong EP spatial gradient also exists in the peripheral region for this simulation.

6.3.4 Effect of Resistivity (η_{vac}) in the Vacuum Region

In the free boundary simulation setup, the plasma resistivity (η_{vac}) is assumed to be higher than the plasma region (η). In subsection 6.3.1, η and η_{vac} are $5.00 \times 10^{-7}\mu_0 v_{A0} R_0$ and $1.00 \times 10^{-4}\mu_0 v_{A0} R_0$, respectively. The validity of this assumption is investigated in this subsection. The spatial profiles and the time evolution of the $n/m = 1/2$ and $n/m = 2/4$ GAEs presented in subsection 6.3.1 are compared with the free boundary simulation results with $\eta_{vac} = 5.00 \times 10^{-7}\mu_0 v_{A0} R_0$. Since Alfvén eigenmode and EPM are the internal mode, it is expected that the linear properties of the $n/m = 1/2$ and $n/m = 2/4$ GAEs will have a weak dependence on η_{vac}. The simulation results are shown in figure 6.9. The $\eta_{vac} = 1.00 \times 10^{-4}\mu_0 v_{A0} R_0$ and $\eta_{vac} = 5.00 \times 10^{-7}\mu_0 v_{A0} R_0$ cases are represented by solid line with and without unfilled circles, respectively. The difference in the linear growth rate and the spatial profile between these two cases are infinitesimal. This figure implies that the linear properties of the $n/m = 1/2$ and $n/m = 2/4$ GAEs have a very weak dependence on η_{vac}.

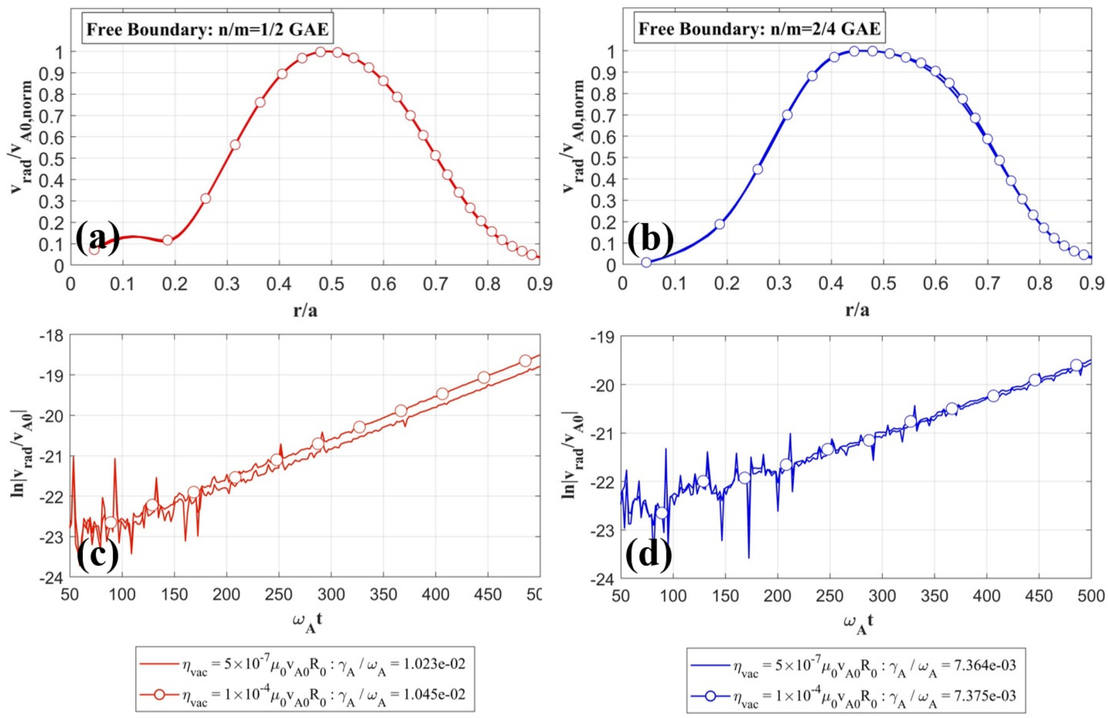

Figure 6.9: The comparison of the effect of η_{vac} on the linear properties of the $n/m = 1/2$ and $n/m = 2/4$ GAEs calculated with the free boundary simulation. Panels(a) and (b) show the normalized spatial profile of the $n/m = 1/2$ and $n/m = 2/4GAEs$, respectively. Panels (c) and (d) shows the time evolution of the $n/m = 1/2$ and $n/m = 2/4$ GAEs, respectively. The solid line with and without unfilled circles represent $\eta_{vac} = 1.00\times10^{-4}\mu_0 v_{A0} R_0$ and $\eta_{vac} = 5.00\times10^{-7}\mu_0 v_{A0} R_0$, respectively.

6.4 $\nabla f_{h0,r60}$: Modeling of the $n/m = 1/2$ EPM at the plasma edge by the free boundary simulation

Section 6.3 has shown that the free boundary simulation can significantly affect the linear growth rate of the peripheral EP-driven MHD mode through the change in the EP-SAW interaction. The $n/m = 1/2$ GAE can be easily destabilized as the dominant mode under this setup. To reproduce the experimentally observed $n/m = 1/2$ EPM at the peripheral region, $\nabla f_{h0,r60}$ is utilized in place of $\nabla f_{h0,r50}$. The spatial profile and the time evolution of the $n/m = 1/2$ EPM will be discussed in subsection 6.4.1. In subsection 6.4.2, the simulated bulk plasma density fluctuation profile ($\delta\rho$) will be compared with the density fluctuation measured with BES. The kinetic analysis and the EP redistribution by the $n/m = 1/2$ EPM and the $n/m = 2/4$ GAE will be presented in subsection 6.4.3. Lastly, the frequency chirping of the $n/m = 1/2$ EPM will be investigated and compared with experiment.

6.4.1 Spatial profiles and time evolution of the $n/m = 1/2$ EPM

The spatial profile of the radial MHD velocity for the $N_f = +1$ and $N_f = +2$ modes calculated by the free boundary simulation are shown in figures 6.10(a-b), respectively. Similar to section 6.3, the utilized EP beta at the magnetic axis (β_{h0}(r/a=0)) is 0.11%. The $n/m = 1/2$ mode is observed as the dominant mode with the frequency of 97.46 kHz. The peak location of the $n/m = 1/2$ mode is

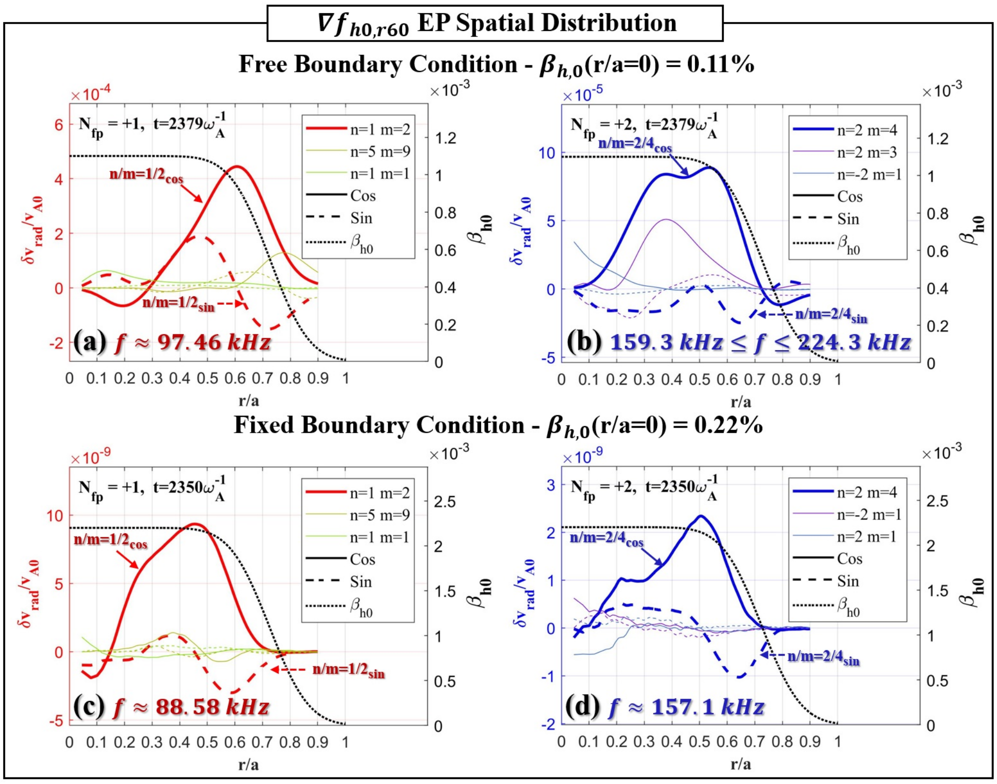

Figure 6.10: The spatial profiles of radial MHD velocity harmonic for the fixed and free boundary $\nabla f_{h0,r60}$ simulations. The simulation results for the free and fixed boundary cases are shown in panels (a-b) and (c-d), respectively. For the fixed boundary simulation, β_{h0}(r/a=0)= 0.22% is utilized. Panels (a) and (c) show $N_f = +1$, and panels (b) and (d) show $N_f = +2$ toroidal mode families.

located around $r/a = 0.60$, which corresponds to the region with the highest EP spatial gradient. This $n/m = 1/2$ mode is potentially an EP mode (EPM), which is supported by its radial location and frequency. Firstly, its radial location does not peak at the extremum of the $n/m = 1/2$ shear Alfvén continuum ($r/a = 0.50$), but adjacent. Secondly, its linear frequency (97.46 kHz) is higher than the fixed boundary case (88.58 kHz). Lastly, this mode has a finite sin component which suggests the strong interaction with the shear Alfvén continuum. Therefore, it is sufficient to conclude that this $n/m = 1/2$ mode is an EPM. For the $N_f = +2$, the coherent structure of the $n/m = 2/4$ mode can only be observed after the saturation of the $n/m = 1/2$ mode (nonlinear phase). This indicates that the $n/m = 2/4$ mode is destabilized by the redistributed EP spatial distribution at $r/a \approx 0.50$. The radial MHD velocity of the $n/m = 1/2$ and $n/m = 2/4$ modes are plotted at the time when the $n/m = 2/4$ mode has the maximum amplitude. Similar to the $n/m = 2/4$ GAE in section 6.3, this $n/m = 2/4$ mode is also located at the extremum of the $n/m = 2/4$ shear Alvén continuum. The linear frequency of the $n/m = 2/4$ mode cannot be accurately measured because it is obscured due to the significant difference between the $n/m = 1/2$ and $n/m = 2/4$ modes. The estimated linear frequency of the $n/m = 2/4$ mode fluctuates between 140 kHz and 210 kHz; therefore, the linear frequency of the $n/m = 2/4$ mode is written as "Unobservable" in figure 6.10(b). The radial location and the frequency of the $n/m = 1/2$ EPM and the $n/m = 2/4$ mode are also compared with the $n/m = 1/2$ and $n/m = 2/4$ shear Alfvén continua in figures 6.5(a-b), respectively.

The role of the boundary condition is also discussed for the $\nabla f_{h0,r60}$ case. The fixed boundary simulation is simulated with β_{h0}(r/a=0.0d0)=0.11%. No EP-driven MHD mode is destabilized with this EP beta value (The simulation results are not shown). In order to destabilize the $n/m = 1/2$ and $n/m = 2/4$ mode in the fixed boundary simulation, β_{h0}(r/a=0) increases from 0.11% to 0.22%. The radial MHD velocity profiles for the $N_{fp} = +1$ and $N_{fp} = +2$ modes calculated by the fixed boundary simulation are shown in figures 6.10(c-d), respectively. Under this higher β_{h0} value, the destabilized $n/m = 1/2$ and $n/m = 2/4$ modes are observed at $r/a \approx 0.50$. Due to their radial locations and their single poloidal dominant harmonic structures, these $n/m = 1/2$ and $n/m = 2/4$ modes are classified as GAEs. This suggests that these 2 GAEs are not destabilized by the strong EP spatial gradient at $0.60 < r/a < 0.70$ but by the weak EP spatial gradient at $r/a = 0.50$. The frequencies of the $n/m = 1/2$ and $n/m = 2/4$ modes are 88.58 kHz and 157.1 kHz, respectively.

The time evolution of the logarithmic amplitude of the $n/m = 1/2$ and the $n/m = 2/4$ radial MHD velocity logarithmic amplitudes are shown in figures 6.11(a-b), respectively. The solid line with filled and unfilled squares represents the time evolution of the free and fixed boundary results, respectively. The linear growth rates are shown in the legend. The calculated linear growth rate of the EP-driven MHD mode with the free boundary simulation is significantly higher than the fixed boundary simulation, despite having lower β_{h0}(r/a=0). These results imply that the peripheral $n/m = 1/2$ EPM cannot be destabilized by the fixed boundary simulation even if the unrealistically high β_{h0} is utilized.

The presented $n/m = 1/2$ EPM and the $n/m = 2/4$ GAE have relatively large mode widths. Their presence can potentially cause the modification of the magnetic field. The Poincaré plot of the magnetic field modified by the $n/m = 1/2$ EPM and the $n/m = 2/4$ GAE is shown in figure 6.12. Panels (a) and (b) show the Poincaré plot of the modified magnetic field during the linear and nonlinear growth phases, respectively. During the linear phase, the differences between the initial and modified magnetic surfaces are infinitesimal. The shape of the LCFS can be retained during the linear growth phase. The modification of the magnetic field is apparent during the nonlinear phase when the mode amplitude is sufficiently large. The reconnections of the magnetic field line are observed. The two magnetic island chains in the middle of the plasma have a poloidal number of 9. This corresponds to the $\iota/2\pi = 5/9$ rational surfaces at $r/a \approx 0.40$ and 0.75 (See figure 5.2). Since the large-amplitude fluctuation caused by MHD mode does not have

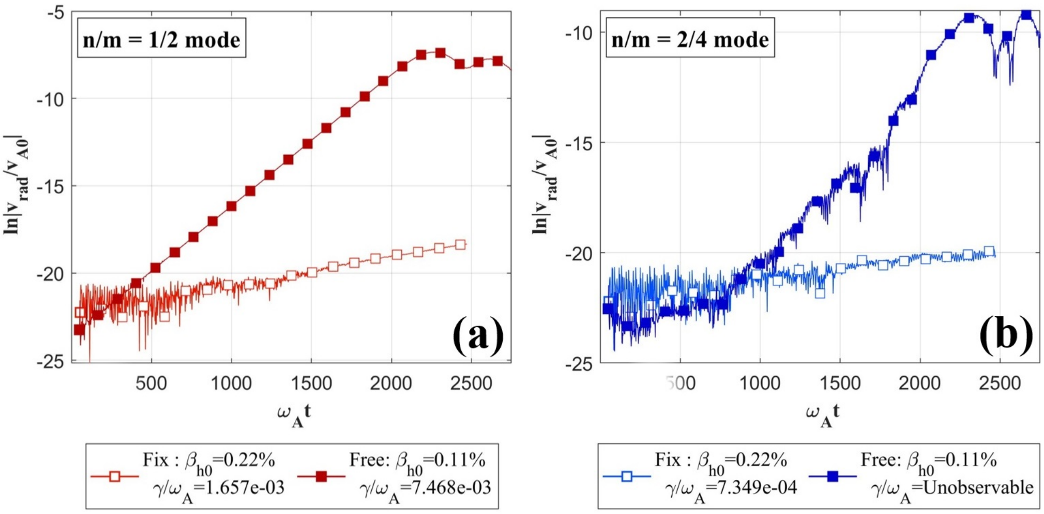

Figure 6.11: The time evolution of the logarithmic amplitude of radial MHD velocity harmonic for $\nabla f_{h0,r60}$ at the location of maximum amplitude. Panels (a) and (b) represent the $n/m = 1/2$ and the $n/m = 2/4$ modes, respectively. The free and fixed boundary simulation results are denoted by the filled and unfilled markers, respectively.

only an interchange parity but also tearing parity during the nonlinear phase[88]. The formation of the magnetic island is possible. This has also been observed in the simulation of the Abrupt Large Event (ALE) in JT-60U[66]. The scale of the magnetic reconnection by the $n/m = 1/2$ EPM needs further validation since the utilized η in this simulation is higher than the experiment. To maintain numerical stability, significantly higher grid resolution (and computational resource) is required to compensate for the reduction in η.

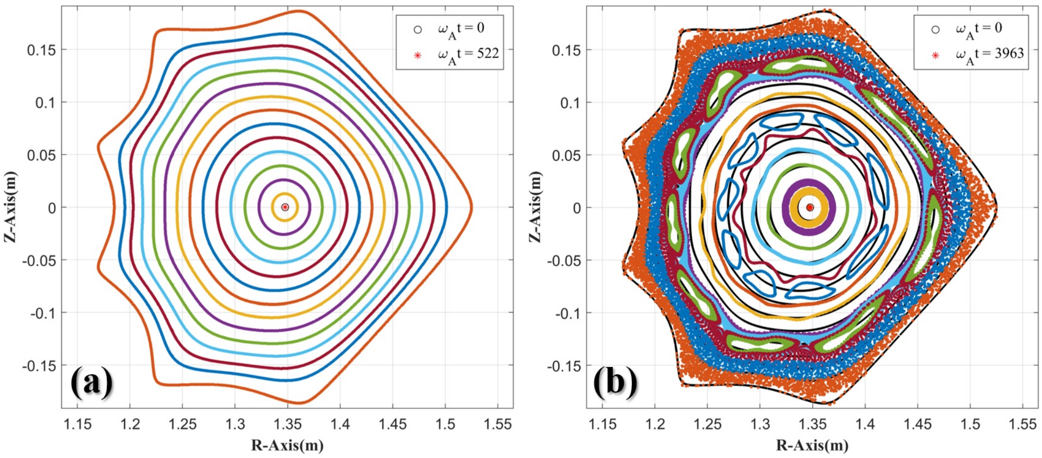

Figure 6.12: The Poincaré plot of the Heliotron J magnetic field modified by the $n/m = 1/2$ EPM. The black marker and colored marker represent the initial and the modified magnetic fields, respectively. Panels (a) and (b) show the Poincaré plot of the modified magnetic field during the linear ($\omega_A t = 522$) and nonlinear ($\omega_A t = 3963$) growth phases, respectively.

6.4.2 Experimental Validation of the $n/m = 1/2$ EPM

The bulk plasma density fluctuation ($\delta\rho$) profile of the $n/m = 1/2$ EPM and the $n/m = 2/4$ GAE calculated by the "$\nabla f_{h0,r60}$ is compared with the density fluctuation measured with the beam emission spectroscopy (figure 3.7). The $n/m = 1/2$ EPM and the $n/m = 2/4$ GAE density harmonics ($\delta\rho$) are shown in figures 6.13(a-b), respectively. The free and the fixed boundary simulation results are represented by solid line and dashed line, respectively. The bulk plasma density fluctuation profiles are closer to the edge region when compared to the radial MHD velocity profiles. This is due to the non-uniformity of the equilibrium bulk plasma density profile. The free boundary simulation results agree well with the density fluctuation signal shown in figure 3.7[25]. The simulated $n/m = 1/2$ EPM ($r/a \approx 0.6907$) corresponds to the maximum peak within the 84.4 kHz ¡ f

¡ 96.0 kHz frequency range at $r/a \approx 0.774$, while the simulated $n/m = 2/4$ GAE ($r/a \approx 0.6356$) corresponds to the maximum peak within the 137.7kHz kHz ¡ f ¡ 149.3 kHz frequency range at $r/a \approx 0.675$, respectively. The discrepancies in terms of the radial location of the $n/m = 1/2$ EPM and the $n/m = 2/4$ GAE between the simulation and the experiment are 0.0833 and 0.0394, respectively. In the fixed boundary simulation, the deviations become much larger. The deviations for the $N/m = 1/2$ and $n/m = 2/4$ modes increase to 0.2428 and 0.1324, respectively. These also suggest that the free boundary condition is necessary for reproducing the experimental observation in Heliotron J.

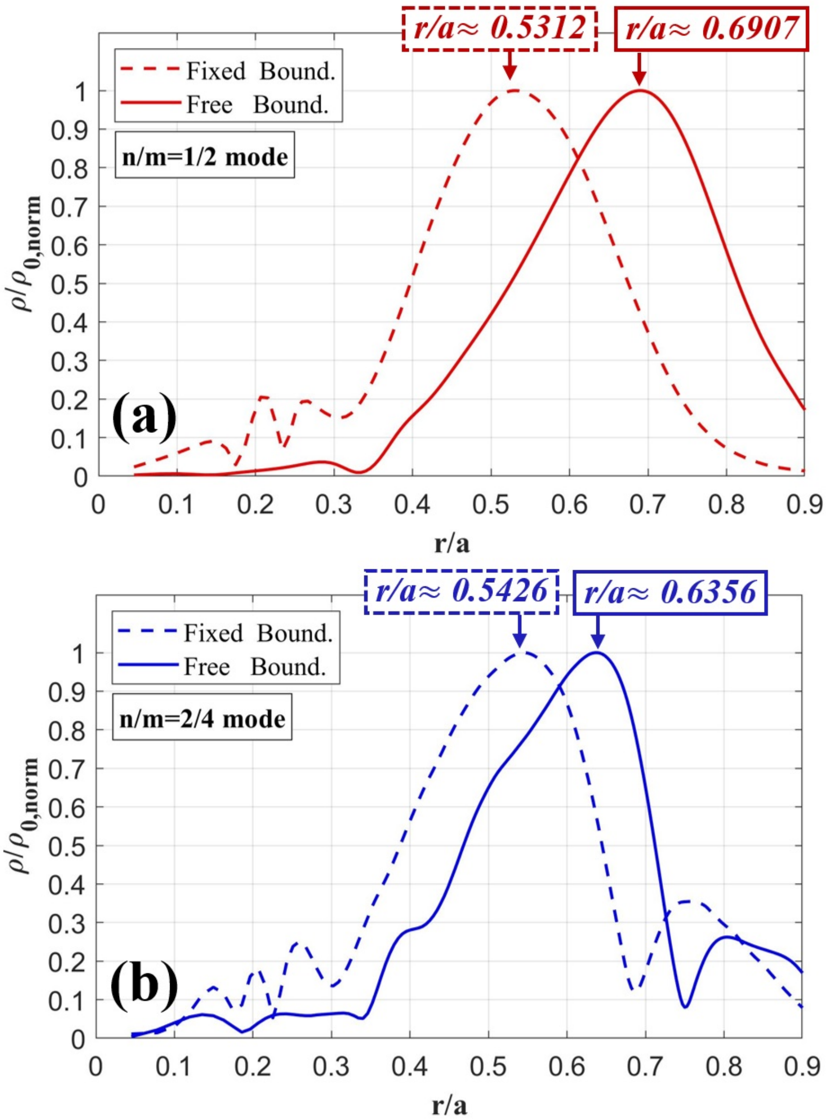

Figure 6.13: The density fluctuation profiles for the $n/m = 1/2$ EPM and the $n/m = 2/4$ GAE for the free boundary "$\nabla f_{h0,r60}$" simulation are shown in panels (a) and (b), respectively. The dash and solid lines represent the free and fixed boundary simulation results.

6.4.3 Kinetic analysis of EP redistribution by the $n/m = 1/2$ EPM and the $n/m = 2/4$ GAE in Heliotron J

Redistribution in velocity space

In this section, the interaction between the EPs and the $n/m = 1/2$ EPM and the $n/m = 2/4$ GAE from the free boundary simulation of the $\nabla f_{h0,r60}$ case is investigated by analyzing the perturbed EP distribution function (δf_h) in velocity (v,Λ) and spatial spaces. The similar approach to chapter 5 is utilized in this section; however, only the helicity ($\mu_B/\nu_B = 1/1$) and toroidicity ($\mu_B/\nu_B = 1/0$) magnetic Fourier components are considered in this analysis. The resonant layers become apparent when the shear Alfvén wave electric field becomes sufficiently large. Since the observed modes are EPM and GAE, the resonant velocities are not identical between co-passing and cntr-passing EPs[89]. The redistribution of the co-passing and counter-passing EPs are shown in figures 6.14, respectively. In contrast to figure 5.11 in chapter 5, the toroidicity and helicity-induced resonant velocities for both the $n/m = 1/2$ and the $n/m = 2/4$ modes are plotted in yellow and purple colors, respectively. The dashed line and dotted line marked with circular markers represent the toroidicity and helicity-induced resonant velocities, respectively. For the EP redistribution by the $n/m = 1/2$ EPM, it is strongest in the high velocity region (see point "1" in figure 6.14). The poloidal resonance numbers ($m+\mu_B j$) of the $n/m = 1/2$ EPM and the $n/m = 2/4$ GAE around point "1" are 1 and 2, respectively. The poloidal resonance number of the $n/m = 1/2$ EPM ($m + \mu_B j = 1$) is closer to $m = 2$ than the poloidal resonance number of the $n/m = 2/4$ GAE ($m+\mu_B j = 2$) to $m = 4$. The resonance layer in the high velocity region tends to have a wider width than the low velocity region. This can be understood by the larger orbit width of the high velocity EPs than the low velocity EPs. These EPs can drift across different flux surfaces; hence, they experience wider ranges of $\iota/2\pi$. This increases the difference between the simulation results and the generalized EP-SAW resonance condition for stellarator/heliotron because $\iota/2\pi$ is assumed to be constant. The helicity-induced resonances ($\mu_B/\nu_B = 1/1$) can be observed in the low velocity region (see point "2" in figure 6.14). The initial distribution function (∇f_{h0}) at around point 2 is lower than the $0.075 < v_h/v_{A0} < 0.125$ velocity region. However, the more intense δf_h is observed around point 2. This is caused by several the helicity and toroidicity-induced resonances within this region. The redistribution caused by the $n/m = 2/4$ GAE is infinitesimal due to its much lower amplitude. This is evident from the regions with only the $n/m = 2/4$ resonant velocity, such as the counter-passing EP redistribution in the $v_h/v_{A0} > 0.30$ velocity range (See point "3" in figure 6.14(b)). In this region, only the $n/m = 2/4$ resonant velocity curve exists, and the clear EP redistribution is

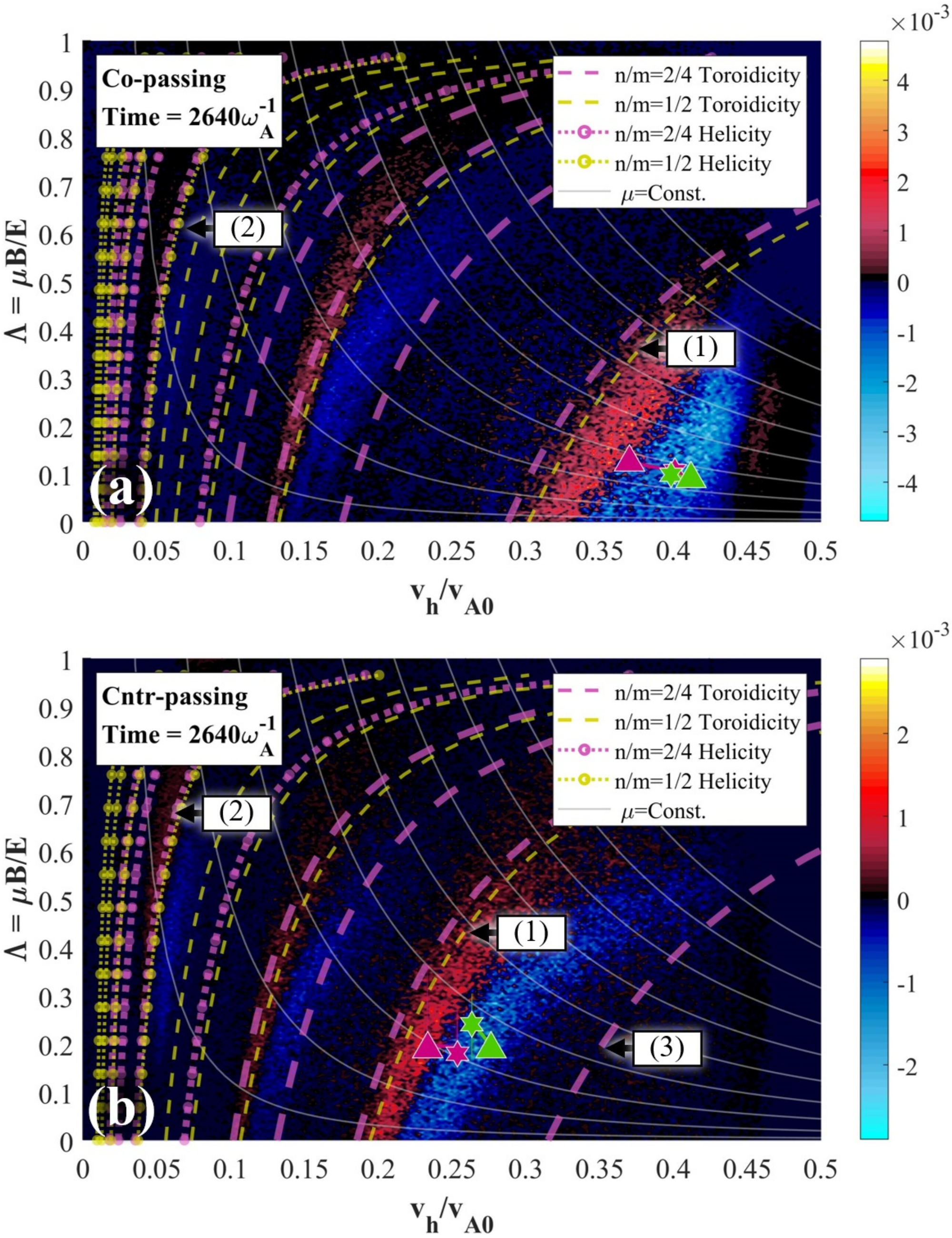

Figure 6.14: The perturbed EP distribution functions due to the interaction with the $n/m = 1/2$ EPM and the $n/m = 2/4$ GAE in velocity space $\delta f_h(v, \Lambda)$ for $\nabla f_{h0,r60}$: (a) co-passing and (b) counter-passing EPs. The dashed and circular marker dotted lines represent toroidicity and helicity-induced resonances, respectively. The yellow and purple colors represent the resonant curves for the $n/m = 1/2$ EPM and the $n/m = 2/4$ GAE, respectively. The purple and green markers indicate the destabilizing and stabilizing resonant EPs with the highest value of $|\delta f_h|$, respectively. The hexagram-shaped and triangular markers indicate the initial and final locations in the velocity space of these resonant EPs, respectively. The Poincaré plot of these EPs are shown in figure 6.17(a-d).

not observed. This is difference from the fixed boundary results (figure 5.11(b)) in chapter 5 because the $n/m = 2/4$ GAE is a dominant mode. In addition, the EP interaction with the $n/m = 1/2$ EPM is weaker for the counter-passing EP. Neglecting the spatial dependence, the weaker interaction is due to the fact that the high velocity $n/m = 1/2$ toroidicity-induced resonance for the counter-passing EP is located in the lower velocity region.

The majority of the redistributions (δf_h) in velocity space are due to the energy transfer from the EPs to the $n/m = 1/2$ EPM. This can be seen from the fact that the positive δf_h (clump) is located in the low velocity side of the resonance layer. The stabilization process can only be observed in the $v_h/v_{A0} > 0.425$ velocity range of the co-passing EP where the clump is located in the high velocity region. This is caused by the sharp $\frac{\partial f_{h0}}{\partial v} < 0$. To confirm these explanations, the total EP energy transfer (ΔE_h) is calculated in velocity space from $\int \vec{E} \cdot \vec{v} dt$. The integrated results for each region in phase space are shown in figure 6.15. The negative (blue) value means that EPs in the particular phase space are losing energy to the shear Alfvén wave. The negative energy transfer regions emerge throughout the velocity phase space, except for the $v_h/v_{A0} > 0.425$ region. In term of the total energy transfer, the main contributions are from the high velocity resonances for both co-passing and counter-passing EPs (see point "1" in figure 6.15), while the contribution of the low velocity resonances ($v_h/v_{A0} < 0.20$) are negligible. This is caused by the lower equilibrium EP distribution function (∇f_{h0}) for the bump-on-tail distribution and from the fact that lower energy particles can transfer less energy to the shear Alfvé wave[90].

Redistribution in spatial space

The spatial redistribution of the high velocity EPs by the $n/m = 1/2$ EPM and the $n/m = 2/4$ GAE for $\nabla f_{h0,r60}$ are discussed. In chapter 5, the dependency of the EP spatial redistribution on the location of the resonant particles in phase space has been demonstrated. The redistributed EP parallel pressure profile by the $n/m = 1/2$ EPM for $\nabla f_{h0,r60}$ is shown in figure 6.16. The majority of the EP redistribution during $t \leq 2247\omega_A^{-1}$ is caused by the $n/m = 1/2$ EPM. Initially, this spatial redistribution increases the EP pressure gradient around $r/a \approx 0.50$. This enhances the EP-driving for the $n/m = 2/4$ GAE. At $t > 2378\omega_A^{-1}$, the EP pressure profile is flattened around $r/a \approx 0.50$. The hollow EP pressure profile forms when the resonant markers that transit the core region[12, 61] have a large δf_h. The guiding centers of the resonant EPs with the largest value of the net energy transfer are traced. The Poincaré plots of the traced resonant co-passing and

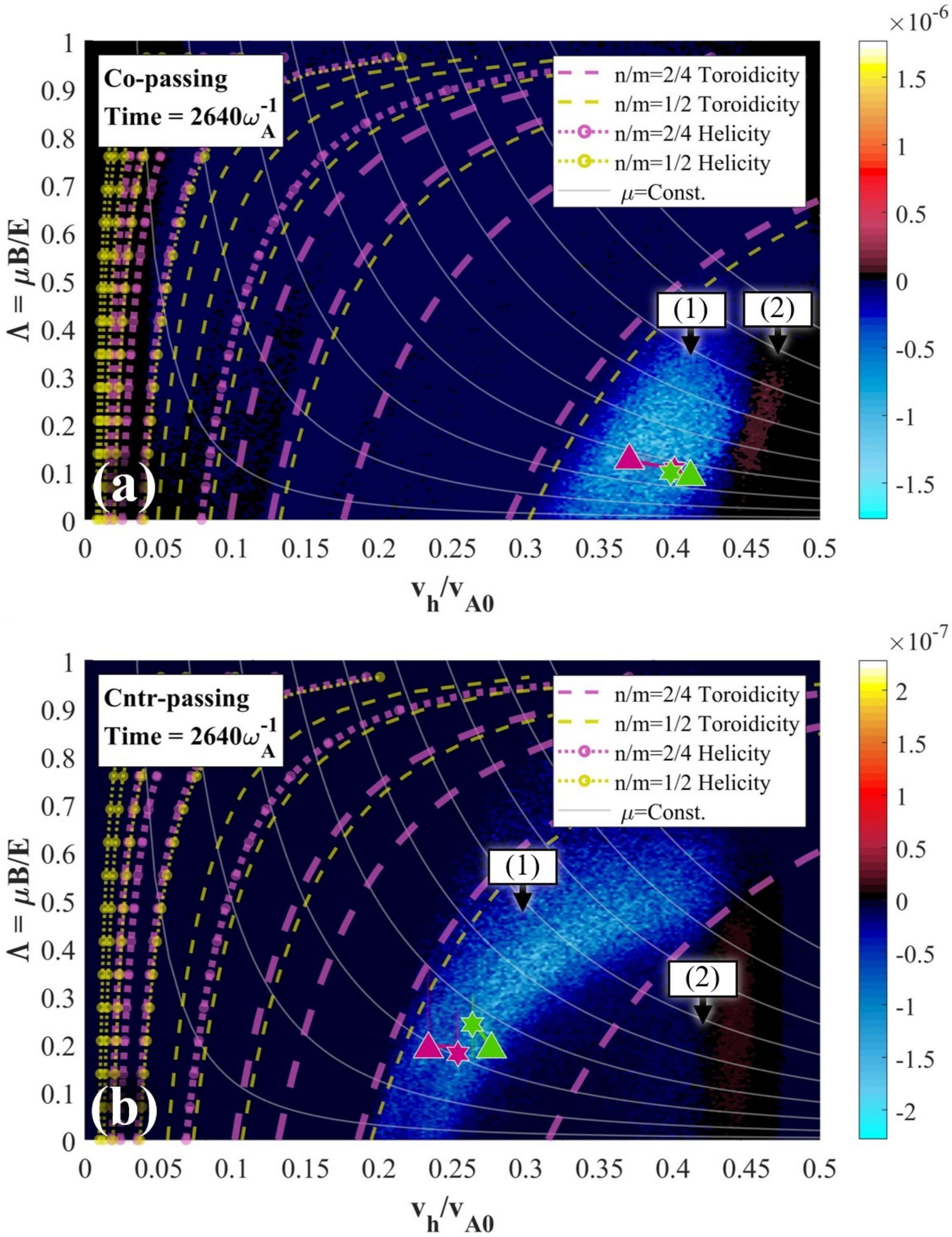

Figure 6.15: The total transferred EP energy via the interaction with the $n/m = 1/2$ EPM and the $n/m = 2/4$ GAE electric field ($\Sigma w_i \vec{v}_{h,i} \cdot \vec{E}$) for $\nabla f_{h0,r60}$: (a) co-passing and (b) counter-passing EPs. The dashed and circular marker dotted lines represent toroidicity and helicity-induced resonances, respectively. The yellow and purple colors represent the resonant curve for the $n/m = 1/2$ EPM and the $n/m = 2/4$ GAE, respectively. The purple and green markers indicate the destabilizing and stabilizing resonant EPs with the highest value of $|\delta f_h|$, respectively. The hexagram-shaped and triangular markers indicate the initial and final locations in the velocity space of these resonant EPs, respectively. The Poincaré plot of these EPs are shown in figure 6.17(a-d).

counter-passing EPs are shown in figures 6.17(a-b) and (c-d), respectively. The destabilizing and stabilizing resonant EPs are shown in panels (a and c) and (b and d), respectively. The time evolution of the kinetic energy of these traced EPs are shown in panel (e). The markers with different colors in each panel represent the same resonant EP but at different times. The color of the marker corresponds to the rainbow color bar on the horizontal axis of the panel (e). During the linear growth phase of the $n/m = 1/2$ EPM, the resonant co-passing EP transit the core region. They have sufficiently large orbit widths such that they can interact with the perpendicular electric of the $n/m = 1/2$ EPM at the plasma edge. This supports the conjecture in section 6.5 where the radially outward shift of the mode profile in the free boundary simulation can enhance the EP and shear Alfvén wave interaction. In contrast to the resonant co-passing EPs, the resonant counter-passing EPs do not transit the core region. Their orbits are localized around the plasma edge. This implies that the resonant counter-passing EPs not only have lower ∇f_{h0} in velocity space but also in spatial space. This further supports the fact that the net EP energy transfer to the $n/m = 1/2$ EPM by the

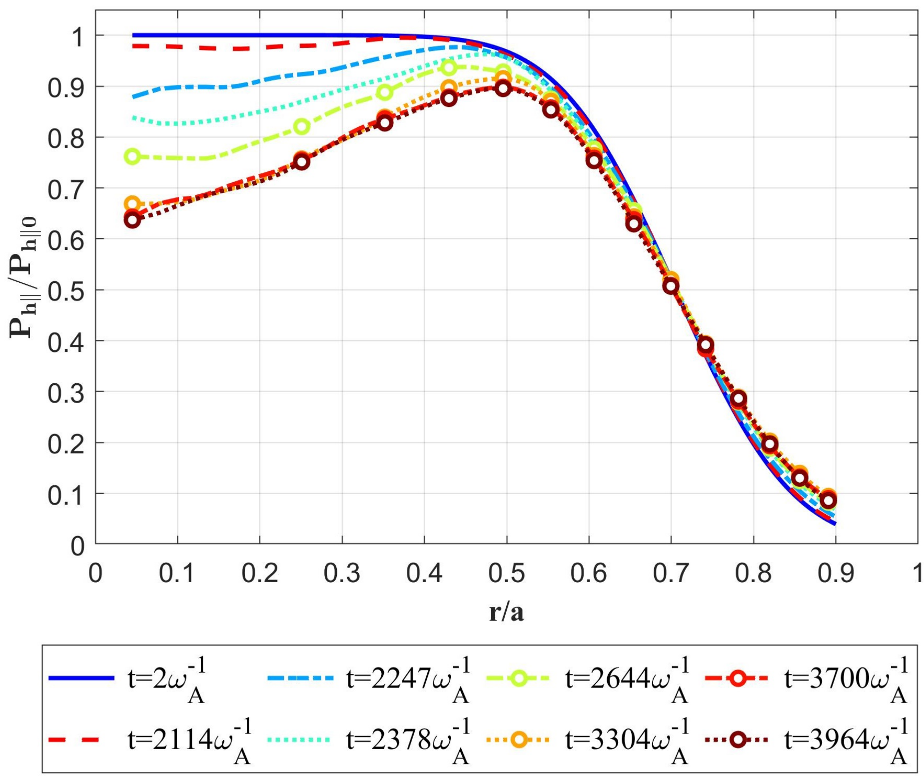

Figure 6.16: The spatial EP redistributions by the $n/m = 1/2$ EPM and the $n/m = 2/4$ GAE for the free boundary $\nabla f_{h0,r60}$ simulation at various time. The $n/m = 1/2$ EPM starts to saturate around t=$2247\omega_A^{-1}$, while the $n/m = 2/4$ GAE saturates after t=$2378\omega_A^{-1}$.

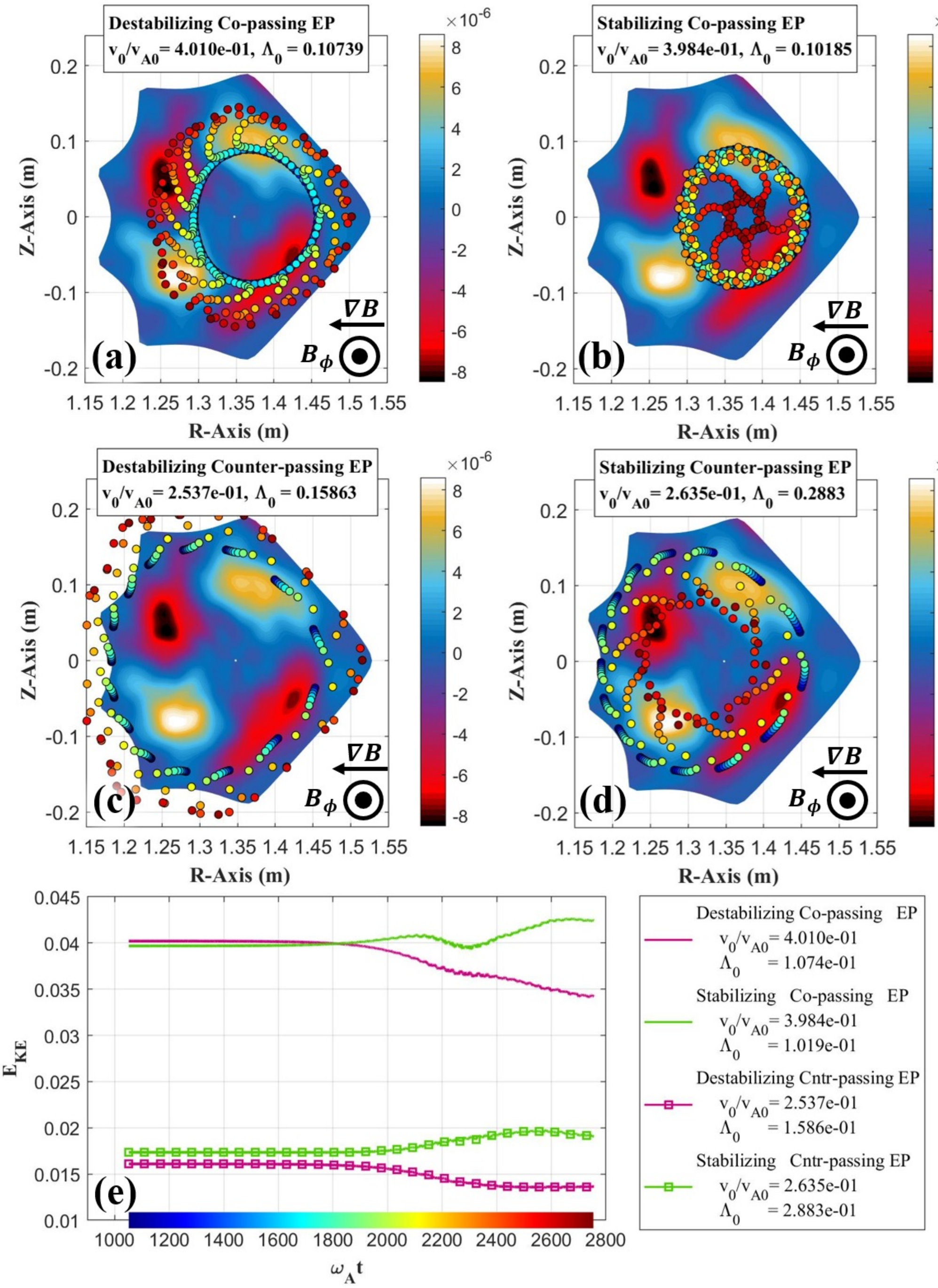

Figure 6.17: The Poincaré plot of the resonant co-passing and counter-passing EPs interacting with the $n/m = 1/2$ EPM in the free boundary "$\nabla f_{h0,r60}$" simulation. The co-passing and counter-passing EPs with the largest value of $|\delta f_h|$ are shown in panels (a-b) and (c-d), respectively. Panels (a) and (c) show destabilizing EPs, while panels (b) and (d) show stabilizing EPs. The time evolution of the kinetic energy of these EPs is shown in (e). The color of each marker in panels (a-d) represents time. The color bar for time is presented on the horizontal axis of the panel (e). The directions of the toroidal magnetic field and the magnetic field gradient are shown at the lower right corner of the panels (a-d).

counter-passing EPs is lower than the co-passing EP (figure 6.15(b)).

The convective transport of the destabilizing EP and the stabilizing EP is in the opposite direction. According to figures 6.17(a-d), the destabilizing EPs are transported radially outward, while the stabilizing EP are transported inward. These results are similar to the tokamak plasma. In the tokamak plasma, the variation of the EP toroidal canonical angular momentum (P_ϕ) also depends on its kinetic energy (E_k)[53, 54]. In the toroidally axisymmetric configuration, "E'", a combination of E_k and P_ϕ, is conserved during the wave-particle interaction. The conservation of "E'" is expressed as $dE'/dt = d(E_k - \omega P_\phi/n)/dt = 0$. By a simple algebraic manipulation, the toroidal canonical angular momentum (P_ϕ) can be written as $\delta P_\phi = (n/\omega)\delta E$. Since the sign of the transport direction depends on the sign of δP_ϕ, the destabilizing ($\delta E_k < 0$) and stabilizing ($\delta E_k > 0$) EPs will be transported radially outward ($\delta P_\phi k < 0$) and inward ($\delta P_\phi k > 0$), respectively. Since the EP destabilization effect must be greater than the stabilization effect, this creates net radially outward transport; thus, producing a hollow EP pressure profile.

In the physical view, the transport direction can also be explained by the sign of the perceived electric field ($\frac{dW}{dt} = \vec{v_h} \cdot \vec{E}$). Since the grad-B drift and curvature drift is pointing downward in Heliotron J, the perceived electric fields of the resonant EPs at the $z = 0$ m plane are pointing upward and downward for the destabilizing and stabilizing EPs, respectively. This results in the different direction of the $E \times B$ kick between the destabilizing and stabilizing EPs.

6.4.4 Frequency Chirping of the $n/m = 1/2$ EPM

In the experiment, the asymmetric downward frequency chirping of the $n/m = 1/2$ EPM has been observed in the power spectrum density (PSD) of the magnetic probe signal. The #61569 PSD of the toroidal magnetic probe signal in the $75kHz$ ¡ f ¡ $110kHz$ frequency range is shown in figure 6.18. This indicates that the EP driving rate (γ_h) and the MHD dissipation rate (γ_d) are comparable[91, 92, 93]. In the experiment, the frequency of the $n/m = 1/2$ EPM chirps from 100 kHz to 87 kHz. In this experiment, the plasma was heated by ECH and NBI. It was found that the application of the on-axis ECH heating can suppress EP-driven MHD modes[25, 94, 95]. These studies also showed that the EP-driven MHD mode transients from the continuous mode to the chirping mode

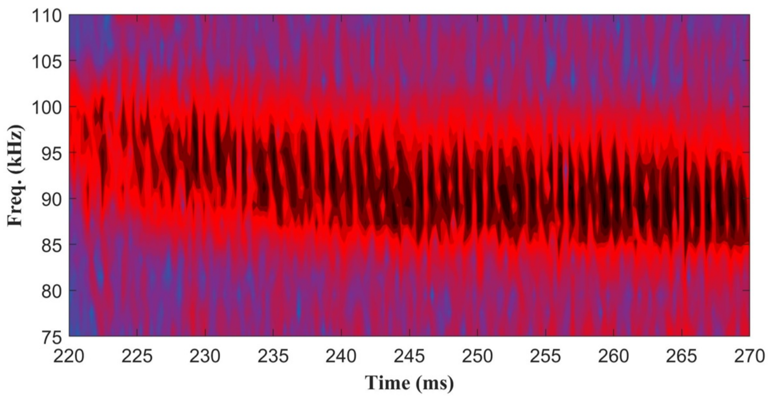

Figure 6.18: The downward frequency chirping of the $n/m = 1/2$ EPM measured with the Mirnov coil in #61569 discharge.

as the ECH power increases. When the ECH power is sufficiently high, the mode bursts. The prospective physical causes are the changes in the trapped electron collision damping rate and the EP pressure profile[79]. Since the trapped electron collision damping effect is excluded in the fluid model, the ECH suppression effect can be compensated by the higher dissipation coefficients (η, ν). These coefficients are already higher than the experimental values as shown in chapter 5. γ_h and γ_d of the $n/m = 1/2$ EPM calculated by the free boundary simulation of the $\nabla f_{h0,r60}$ case are calculated by the time evolution of total EP energy transfer and the MHD fluctuation energy transfer. The calculated γ_h and γ_d for the $n/m = 1/2$ EPM are shown in figure 6.19. It is seen that γ_h and γ_d are at the comparable level.

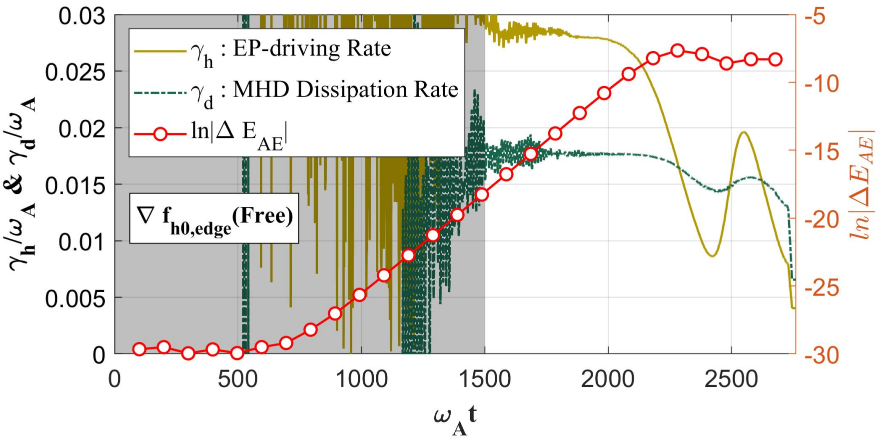

Figure 6.19: The time evolution of the γ_h (yellow solid line), γ_d (green dash-dotted line), and ΔE_{AE} (red solid line with unfilled circles) of the $n/m = 1/2EPM$. γ_h and γ_d are referred to the left vertical axis, while ΔE_{AE} is referred to the right vertical axis.

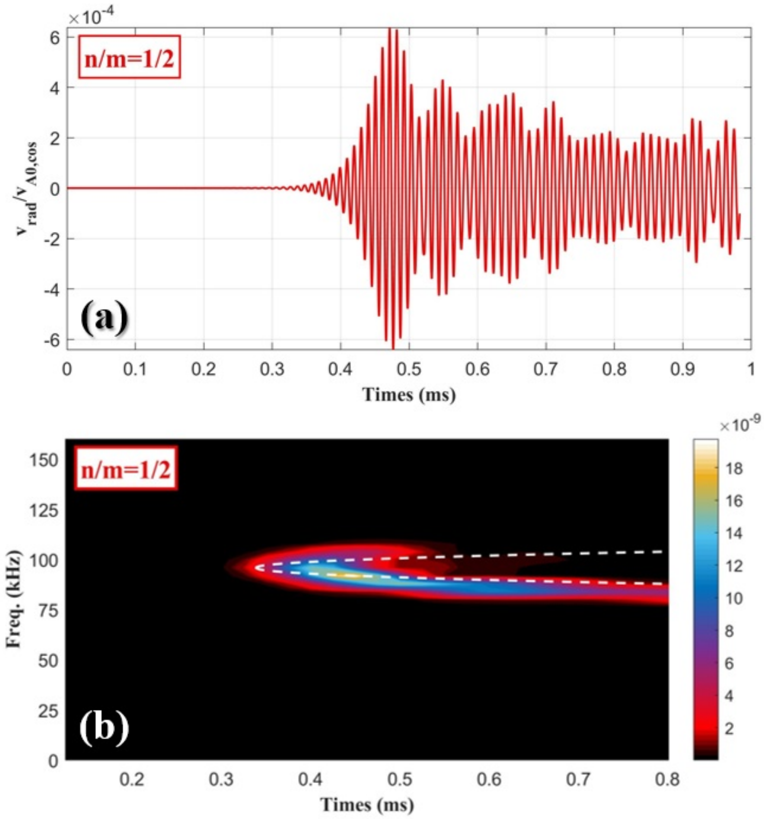

Figure 6.20: (a) The time evolution of cosine components of the $n/m = 1/2$ radial MHD velocity harmonics. (b) The power spectral density of the $n/m = 1/2$ radial MHD velocity harmonic. The calculated frequency chirping from the Berk-Breizman model[91, 96] is plotted by the white dashed line.

The time evolution of the simulated $n/m = 1/2$ EPM radial MHD velocity is shown in figure 6.20(a). After the mode saturation at $t \approx 0.475ms$, the beating pattern is observed. The PSD of the $n/m = 1/2$ EPM radial MHD velocity harmonic is shown in figure 6.20(b). The simulated results are also compared with the Berk–Breizman (BB) model[96], where the EP driving rate and MHD dissipation rate are obtained from figure 6.8(a). The results from the Berk-Breizman model are denoted by the white dashed lines in figure 6.20(b). The asymmetric downward frequency chirping is observed. The $n/m = 1/2$ EPM chirps downward from the linear frequency (ω_o) of 97.46 kHz to 80.00 kHz. The upward frequency chirping has a much lower amplitude. It can be observed only within the $0.30 < t < 0.50$ range. After $t \approx 0.50$ ms, the upward frequency chirping dissipates. This is possibly caused by the increase in the toroidicity-induced resonant velocity between the $n/m = 1/2$ EPM and the co-passing EPs. When the frequency of the n/m=1/2 EPM chirps upward, EP needs higher velocity to keep resonate with the mode. Since the majority of the EP drive is caused by the interaction between the high-velocity co-passing EPs and shear Alfvén wave through the "m+j=1" high-velocity toroidicity-induced resonance (See figure 6.14), the increase in the co-passing EP resonant velocity can exceed the NBI injection energy of Heliotron J. This also implies that the resonant velocity of the upward frequency chirping will shift into the $\partial f_h/\partial v < 0$ (stabilizing) region.

6.5 Dependency of the free boundary effect on the plasma shape

In this section, the dependency of the free boundary effect on the plasma shape is estimated. In the toroidally symmetric configuration (e.g. tokamak), the role of the boundary condition was found to be more significant in the strongly shaped plasma[43]. In Heliotron J plasma, this dependence is analyzed in the 3 main magnetic configurations: low bumpiness ($\epsilon_{01} = 0.01$), standard ($\epsilon_{01=0.06}$), and high bumpiness configurations ($\epsilon_{01=0.15}$). The MHD equilibrium of the standard and high bumpiness configurations are calculated based on the same bulk plasma density and temperature profiles as the low bumpiness configuration in sections 6.1-6.4. The MHD equilibria for these magnetic configurations are shown in figures

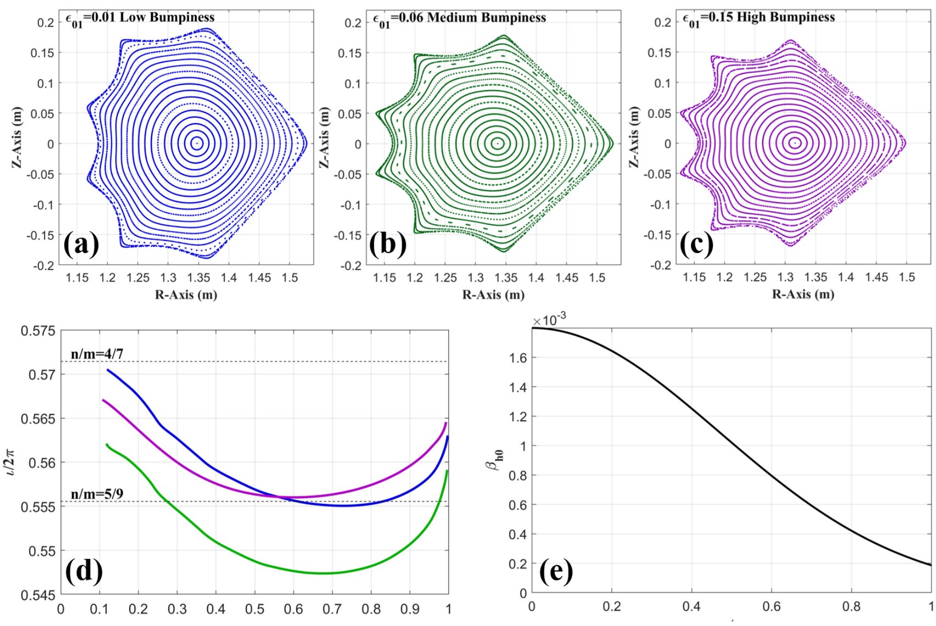

Figure 6.21: The low beta currentless MHD equilibria for the low, standard, and high bumpiness configurations. The Poincareé plot of the equilibrium magnetic field for the low, standard, and high bumpiness magnetic configurations are shown in panels (a), (b), and (c), respectively. The rotational transform profiles of these MHD equilibria are shown in panel (d). The initial EP pressure profile is shown in panel (e).

6.21. The Poincaré plot and the rotational transform ($\iota/2\pi$) profile of these MHD equilibria are shown in panels (a-c) and (d), respectively. From the Poincaré plot, the plasma is more shaped and has a smaller plasma volume in the standard and high bumpiness configurations. The difference in terms of the $\iota/2\pi$ profile is infinitesimal. This is also reflected in the calculated $n/m = 2/4$ shear Alfvén continuum for each MHD equilibrium (figure 6.22). The initial EP pressure profile for this calculation is shown in figure 6.21(e). Differ from sections 6.1-6.4, the initial EP pressure profile has a strong gradient in the core region.

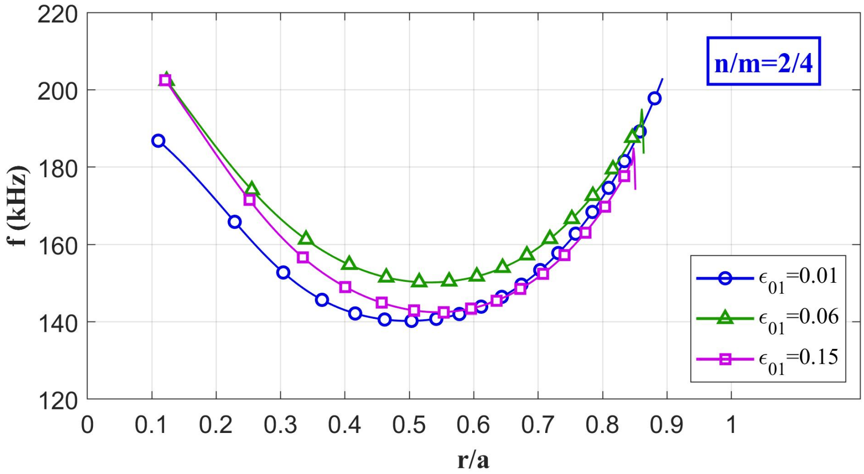

Figure 6.22: The $N_f = +2$ shear Alfvén continua of the low beta currentless for the (a) low bumpiness, (b) standard, and (c) high bumpiness configurations. The $n/m = 2/4$ shear Alfvén continuum is plotted by blue solid line. Other shear Alfvén continua are plotted by gray solid lines.

In these MHD equilibria, the $n/m = 2/4$ mode is observed as a single dominant mode for all the magnetic configurations. The fixed and free boundary simulation results for the low, standard, and high magnetic configurations are compared. The spatial profile of the $N_f = +2$ radial MHD velocity harmonics calculated with the fixed and free boundary simulations are shown in figures 6.23(a,c,e) and (b,d,f), respectively. For all the magnetic configurations, the $n/m = 2/4$ GAEs are peaked around the $0.30 < r/a < 0.50$ range. Similar to the results in sections 6.3 and 6.4, the major differences between the fixed and free boundary simulations results are the radial location and the spatial width of the mode. In the free boundary simulation, the mode spatial profile radially shifts outward to the plasma edge region by roughly $\Delta(r/a) \approx 0.05$, and the mode widths are also broadened. According to the $n/m = 2/4$ shear Alfvén continuum shown in figure 6.22, these $n/m = 2/4$ modes do not located at the extremum of their individual $n/m = 2/4$ shear Alfvén continua but adjacent. The mode structures from all cases also have a finite sine component, which suggests a strong interaction with the shear Alfvén continuum.

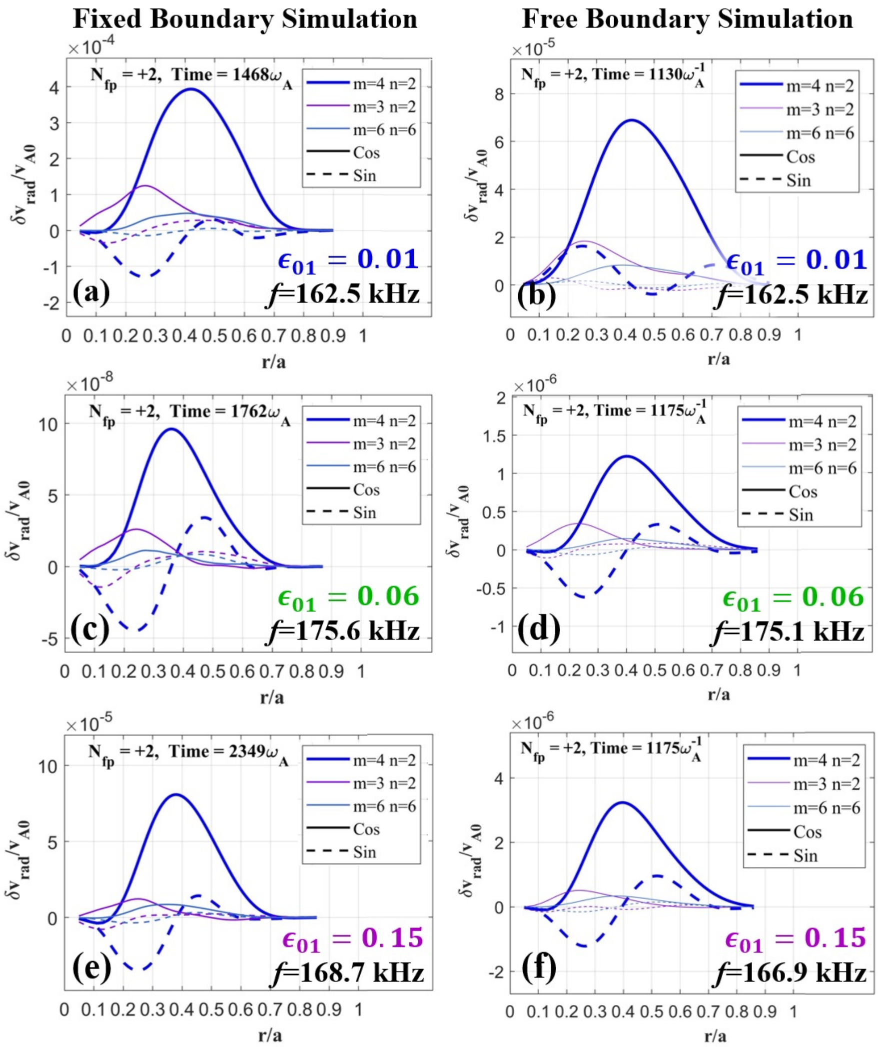

Figure 6.23: The spatial profile of the $N_f = 2$ radial MHD velocity harmonic from the low ($\epsilon_{01} = 0.01$, a-b), standard ($\epsilon_{01} = 0.06$, c-d), and high bumpiness ($\epsilon_{01} = 0.15$, e-f) configurations. The fixed and free boundary simulation results are shown in panels (a, c, and e) and (b, d, and f), respectively.

Therefore, it is sufficient to conclude that these $n/m = 2/4$ modes are EPMs.

The logarithmic time evolution of the $n/m = 2/4$ radial MHD velocity harmonics from each magnetic configuration are shown in figure 6.24. In this figure, the $n/m = 2/4$ EPM from the low, standard, and high bumpiness configurations are represented by blue, green, and violet colors, respectively. The estimated linear growth rate (γ/ω_A) of the $n/m = 2/4$ EPM with the fixed boundary simulation for the low, standard, and high bumpiness configurations are 9.69×10^{-3}, 3.540×10^{-3}, and 5.985×10^{-3}, respectively. The linear growth rate of the $n/m = 2/4$ EPM is highest for the low bumpiness case, while the linear growth rate is significantly lower in the standard and high bumpiness configurations. Interestingly, the linear

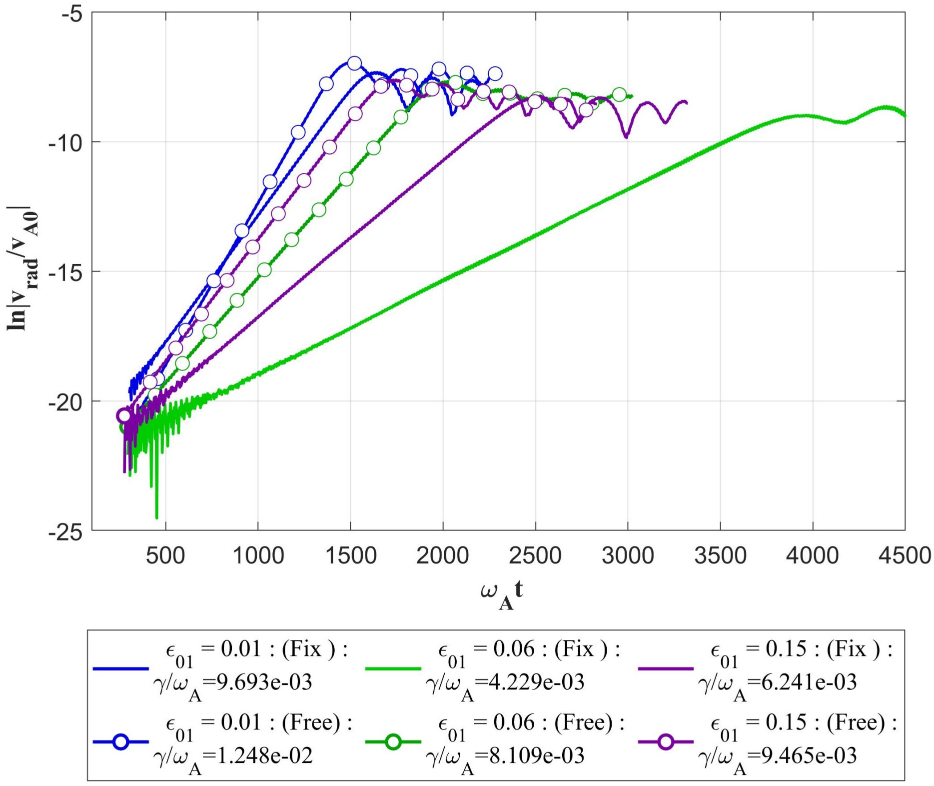

Figure 6.24: The time evolution of the logarithmic amplitude of the $n/m = 2/4$ radial MHD velocity harmonic for the low, standard, and high bumpiness configurations. The fixed and free boundary simulation results are shown in panels (a) and (b), respectively.

growth rate from all of the magnetic configurations becomes comparable in the free boundary simulation. In the free boundary simulation, the linear growth rate of the $n/m = 2/4$ for the low, standard, and high bumpiness configurations increase to 1.248×10^{-2}, 8.109×10^{-3}, and 9.465×10^{-3}, respectively. The changes are roughly 28.75%, 91.75% , and 51.66% for the low, standard, and high bumpiness configurations, respectively. These results suggest the importance of the boundary condition in the strongly shaped plasma. In addition, these results also show that the boundary condition has the essential role in Heliotron J. The effect of the boundary condition is finite even for the $n/m = 2/4$ EPM that is localized in the core region.

6.6 Summary

The roles of the boundary condition for the simulation of the EP-driven MHD instabilities in Heliotron J were investigated in this chapter. The free and fixed boundary simulation results were compared. It was shown that the free boundary condition is necessary to reproduce the experimentally observed EP-driven MHD modes (e.g. $n/m = 1/2$ EPM and $n/m = 2/4$ GAE) in the peripheral region of Heliotron J. With the free boundary condition, the $n/m = 1/2$ EPM and the $n/m = 2/4$ GAE at the peripheral region can be destabilized within the range of reasonable initial EP pressure. The free boundary simulation predicts a higher linear growth rate when compared to the fixed boundary case. The increase in the linear growth rate is brought about by the enhancement of the EP driving rate while the MHD dissipation remains almost the same. This is caused by the changes in the EP and shear Alfvén wave interaction through the broadening and the outward radial shift of the mode spatial profile. The effect of the free boundary condition will be significant if the EP spatial gradient is located in the peripheral region. It was supported by the kinetic analysis of the EP redistribution in real and velocity spaces. Since the initial EP velocity distribution is the bump-on-tail velocity distribution, the resonant EPs with the largest value of δf_h are the high velocity co-passing EPs from the core region. These resonant co-passing EPs have sufficiently large orbit widths such that they can effectively interact with the $n/m = 1/2$ EPM at the plasma edge.

The dependency of the linear growth rate of the $n/m = 1/2$ and $n/m = 2/4$ GAEs on the perfectly conducting wall position. The set of artificially created perfectly conducting walls is created based on the actual Heliotron J vacuum vessel and the LCFS. The linear growth rates of both the $n/m = 1/2$ and $n/m = 2/4$ GAEs significantly increase as the distance between the LCFS and the perfectly conducting wall increases. After a finite increase in the wall distance, the linear growth rate quickly approaches "no wall limit," where further increases in the wall distance do not affect the outcome. This result also shows that the changes in the linear growth rate are more significant for the low-n MHD mode ($n/m = 1/2$ GAE).

The dependency of the free boundary effect on the plasma shape was investigated. These results suggested that the boundary condition becomes more significant in the MHD equilibrium with strongly shaped plasma and smaller plasma volume. The boundary condition can have a significant effect on the EP-driven MHD mode even if the mode is located more toward the core region ($r/a < 0.4$) in Heliotron J. In addition, the dependence of the linear growth rate (γ/ω_A) of the EP-driven MHD mode on the distance between the plasma and the perfectly conducting wall ($\Delta\overline{w}$) is stronger than the tokamak plasma[44]. This is possibly due to the low magnetic of Heliotron J. It would be interesting to investigate the effects of the free boundary condition on other stellarator/heliotron configurations, such as the Large Helical Device (LHD). It is expected that the free boundary effects will be weaker since LHD has a higher magnetic shear.

Chapter 7

Conclusions

In summary, the EP-SAW and SAW-SAW interactions in Heliotron J, the quasi-isodynamic optimized low magnetic shear helical-axis heliotron, were clarified and discussed. These interactions were investigated numerically by MEGA, a hybrid EP-MHD simulation code. The presented results have expanded the view of the EP-driven MHD instabilities in Heliotron J. These include the role of EPs in each particular phase space and their interactions with the SAW via toroidicity and helicity-induced resonances. These results also clarify the EP transport in Heliotron J. Besides the clarification of the EP-SAW and SAW-SAW interactions in Heliotron J, the experimental validation was performed. Previously, MEGA has been applied only in the planar axis device with high magnetic shear, such as tokamak and LHD. Unlike these devices, the fixed boundary condition significantly affects the EP-driven MHD mode in Heliotron J where the EP interaction with the low-n MHD mode is significantly underestimated. This discrepancy between the simulation and experiment was tackled by the free boundary condition. The role and the necessity of the boundary condition in Heliotron J in the simulation of the low-n MHD mode has been confirmed.

In the first part (chapter 5), the EP-driven MHD modes in the low beta currentless equilibrium of Heliotron J were simulated. The referred experimental discharge is #61569. From the magnetic fluctuation measured with the Mirnov coils and the density fluctuation signal measured with BES, the peripheral $n/m = 1/2$ EPM at $r/a > 0.70$ is the dominant mode. The second dominant mode is the $n/m = 2/4$ GAE at $r/a \approx 0.50$. In addition to these two modes, another mode with the same frequency as the $n/m = 1/2$ EPM was observed near the plasma core ($0.30 < r/a < 0.50$). This mode has a smaller amplitude than the $n/m = 1/2$ EPM. From the MEGA simulation results, the $n/m = 2/4$ and $n/m = 1/2$ modes GAEs were destabilized at $r/a \approx 0.50$. The $n/m = 2/4$ GAE was successfully reproduced in the simulation; however, the $n/m = 1/2$ EPM cannot be destabilized by any means (e.g. increasing the spatial gradient of the EP distribution function and EP pressure). In contrast to the experiment, the $n/m = 1/2$ GAE was observed at $r/a \approx 0.50$ instead. This $n/m = 1/2$ GAE has a much smaller linear growth rate than the $n/m = 2/4$ GAE. The possible candidate of this $n/m = 1/2$ GAE is the weaker EP-driven MHD mode at $0.171 < r/a < 0.522$ since it shares a similar frequency as the $n/m = 1/2$ EPM; however, the amplitude of this weaker mode in the experiment is still greater than the $n/m = 2/4$ GAE. According to the kinetic analysis, the poloidal resonance number $(m + j\mu_B)$ of the $n/m = 1/2$ high-velocity toroidicity-induced resonance for the co-passing EP is 1. This is closer to its poloidal mode number (m=2) than the $n/m = 2/4$ GAE case. For the $n/m = 2/4$ GAE, the poloidal resonance number of the high-velocity toroidicity-induced resonance for the co-passing EP is 2, which is farther than its poloidal mode number (m=4). This suggests that the EP-SAW interaction should be stronger for the $n/m = 1/2$ GAE than the $n/m = 2/4$ GAE, but this was not observed in the simulation. Other factors and assumptions, such as the boundary condition, need to be reconsidered. In the last section, the interactions between the EPs and the $n/m = 2/4$ GAE between the bump-on-tail and the slowing-down velocity distributions were compared. The bump-on-tail case represents the experimentally observed EP energy distribution, while the slowing-down case represents the ideal scenario where $\tau_{cx} >> \tau_{sd}$ The calculation results showed no significant difference in the linear growth rates between these two distributions. For both the bump-on-tail and slowing-down distributions, the high velocity EPs effectively interact with the $n/m = 2/4$ GAE through the high velocity toroidicity-induced resonance. The role of the helicity-induced resonances are weaker than the toroidicity-induced resonances because they are localized in the low velocity region ($v_h/v_{A0} < 0.10$). In the bump-on-tail velocity distribution, the EPs in $v_h/v_{A0} > v_{inj}$ range have a strong stabilization mechanism. This is due to the finite $\partial f/\partial v < 0$. In the slowing-down distribution, the existence of these helicity-induced resonances in the low velocity region compensates the reduction of the EP drive via the high velocity toroidicity resonance. The differences in the initial EP distribution also cause differences in the redistributed EP pressure profile. The hollow (flat) EP pressure profile is formed after the saturation of the EP-driven MHD modes in the bump-on-tail (slowing-down) distribution.

In the second part (chapter 6), the discrepancy in the $n/m = 1/2$ EPM between the simulation and the experiment was investigated. It was tackled by the free boundary simulation. In this boundary condition, the MHD plasma at the LCFS is not surrounded by the perfectly conducting wall but the vacuum region. Due to the low magnetic shear of Heliotron J, any low-n MHD mode potentially has a large mode width. It is possible that even the core localized low-n MHD mode can cause a finite plasma displacement at the LCFS. With the free boundary condition, the missing $n/m = 1/2$ EPM at the plasma edge has been successfully reproduced. The underlying effect of the boundary condition is on the kinetic part of the EP, while its effect on the MHD part is small. The simulated mode spatial profile by the free boundary simulation is also broader than the fixed boundary results. The peak of the mode is also shifted radially outward toward the edge region. These two modifications enhance the EP-SAW interaction in three ways: (1) broader profile allows more EPs to interact with the mode, (2) mode perceives the stronger EP spatial gradient (if the EP spatial gradient is finite at the peripheral region), and (3) the high velocity co-passing EPs transit the core region. It is also demonstrated that the $n/m = 1/2$ EPM cannot be destabilized in the fixed boundary condition even if the significantly higher EP beta is utilized. Lastly, the dependency of the free boundary effect on the plasma shape and volume was investigated. The low, standard, and high bumpiness magnetic configurations were considered. The plasma of the standard and the high bumpiness configurations are more shaped and have a smaller volume than the low bumpiness configuration. The calculation results show that the calculated linear growth rates from the standard and high bumpiness magnetic configurations were significantly lower in the fixed boundary simulation. The effect of the boundary condition is significant even on the low-n mode that is located in the core region ($0.3 < r/a < 0.4$).

Future Studies

In this study, the EP-SAW and SAW-SAW interactions in the high beta plasma have not yet been investigated in Heliotron J. The effect of the non-inductive current drive on the EP-SAW resonance has not been investigated. The non-inductive current drive can alter the EP-SAW resonance through the change in the rotational transform. Another interesting consequence of the non-inductive current-driven MHD equilibrium is the formation of the low-order magnetic islands. In the field of the EP-driven MHD instability simulation, the nested flux surface is a common assumption. This assumption is valid only in the high shear device because the size of the magnetic island is negligible. In the low magnetic shear device (e.g. Heliotron J and W7-X), the low-order magnetic island can have a finite width. Previously, the effect of the magnetic island on the EP-driven MHD mode has been studied theoretically and experimentally such as the frequency up-shift of the accumulation point of the shear Alfvén continuum[97, 98] and the formation of the magnetic island-induced Alfvén eigenmode (MiAE)[99]. However, the impact of the static magnetic island on the EP-driven MHD mode in the realistic plasma shape has not yet been simulated. This issue will also be important in the high beta plasma equilibrium. Since MEGA has been successfully validated with Heliotron J, a low shear device, its application on the MHD equilibrium with low-order magnetic islands is advantageous because the MHD plasma is represented by the cylindrical coordinate.

In addition to ECCD, the electron cyclotron resonance heating (ECRH) was also found to have a stabilization effect on the EP-driven MHD instability in certain plasma discharges. In Heliotron J and TJ-II devices, the amplitude of the EP-driven modes was reduced with the application of the on-axis ECRH. The time evolution of the mode changes from continuous modes into the chirping mode. However, this is not always true. In the low-bumpiness configuration of Heliotron J, the amplitude of the $n/m = 1/2$ EPM and the $n/m = 2/4$ GAE reduce with the increasing ECRH power (109-234 kW). However, at the ECRH power of 308 kW, the amplitude of the EPM and GAE slightly increase. The nonlinear relation between ECRH power and amplitude of EP-driven MHD mode was also observed in other magnetic configurations[79]. The application of ECRH can affect (1) EP slowing-down time (τ_{sd}), (2) bulk plasma pressure, and (3) trapped electron collisional damping rate. The first and second parameters can be investigated by the current model in MEGA. For the collisional damping of the trapped electron, a more sophisticated model is necessary.

In the recent study, the thermal ion kinetic effect is incorporated in the new MEGA code[85]. This allows us to investigate the alpha channeling effect of the thermal ion[100, 101]. The additional toroidally asymmetric resonances in stellarator and heliotron configurations can potentially increase the ion Landau damping[16]. The effectiveness of these additional resonances in the stellarator and heliotron configuration can be further investigated.

Acknowledgements

I would like to sincerely thank both of my current and former academic advisor Assoc. Prof. Dr. Kado Shinichiro and Asst. Prof. Dr. Yamamoto Satoshi (QST) for their kind supports, guidance, and opportunities during my graduate study. Both of them provided me with invaluable knowledge especially in the Heliotron J magnetic field, experiment, and presentation skills. Indispensably, I also need to thank Prof. Dr. Todo Yasushi (NIFS), my co-advisor. He assisted me with technical support on MEGA, the simulation methodology, and the theoretical discussion on the EP-driven MHD instability-related topics.

I also need to express my appreciation to all Heliotron J professors: Prof. Dr. Nagasaki Kazunobu, Assoc. Prof. Dr. Minami Takashi, Asst. Prof. Dr. Kobayashi Shinji, Asst. Prof. Dr. Oshima Shinsuke, Dr. Okada Hiroyuki, Dr. Mizuuchi Tohru, and Dr. Konoshima Shigeru for their fruitful discussions and experimental supports. Prof. Dr. Nagasaki Kazunobu always has a keen interest in my research. For the MHD equilibrium preparation, I need to thank Assoc. Prof. Dr. Takashi Minami and Asst. Prof. Dr. Kobayashi Shinji for providing me with the technical knowledge on Thomson scattering and charge exchange recombination spectroscopy (CXRS). Asst. Prof. Dr. Kobayashi Shinji equipped me with technical knowledge in the neutral beam injection and the beam emission spectroscopy (BES) systems of Heliotron J. Asst. Prof. Dr. Ohshima Shinsuke always gives me fruitful comments during the seminar. Lastly, I need to thank Dr. Mizuuchi Tohru for granting me an opportunity to study magnetic confinement fusion during my master's program.

The presented MHD equilibria in this work were prepared by HINT. This code was provided by Assoc. Prof. Dr. Suzuki Yasuhiro (National Institute for Fusion Science, NIFS, Japan). I need to express my gratitude for his guidance on the MHD equilibrium calculation by HINT.

The presented MEGA and HINT calculation results in this thesis were performed at the Plasma Simulator (FUJITSU FX100 and NEC SX-Aurora TSUB-

ASA) of the National Institute of Fusion Science (NIFS) and the JFRS-1 of the International Fusion Energy Research Center. I would like to sincerely thank all the technicians and the any-related members.

This thesis was partially supported by the "PLADyS", JPSP Core-to-Core, A. Advanced Research Networks and Future Energy Research Association. My doctoral and master's studies were fully supported by the and Monbukagakusho (MEXT) and Konosuke Matsushita Memorial Foundation (KMMF) scholarships, respectively.

Lastly, I am eternally grateful for the invaluable love and lifetime support of my family, my father, Adulsiriswad Manas; my mother, Adulsirisawad Runjana; and my brother, Adulsirisawad Nithi. In this imperfect world, they have put all of their efforts to raise me in a warm environment. All of their efforts are not futile, they have granted me an opportunity to conduct magnetic confinement fusion research.

Lists of Publication, Presentations and Awards

- ## Publication

1. P. Adulsiriswad, Y. Todo, S. Yamamoto, S. Kado, S. Kobayashi, S. Ohshima, H. Okada, T. Minami, Y. Nakamura, A. Ishizawa, S. Konoshima , T. Mizuuchi and K. Nagasaki, "Magnetohydrodynamic hybrid simulation of Alfvén eigenmodes in Heliotron J, a low shear helical axis stellarator/heliotron," Nucl. Fusion 60 (2020) 096005
2. P. Adulsiriswad, Y. Todo, S. Kado, S. Yamamoto, S. Kobayashi, S. Ohshima, H. Okada, T. Minami, Y. Nakamura, A. Ishizawa, S. Konoshima , T. Mizuuchi and K. Nagasaki, "Numerical Investigation of the Peripheral Energetic Particle driven MHD Modes in Heliotron J, a Low Shear Helical-Axis Stellarator/Heliotron with Free Boundary Hybrid Simulation," *Submitted to Nuclear Fusion*

- ## Oral Presentation

1. P. Adulsiriswad, Y. Todo, S. Kado, S. Yamamoto, S. Kobayashi, S. Ohshima, T. Minami, H. Okada, A. Ishizawa, Y. Nakamura, S. Konoshima, T. Mizuuchi, K. Nagasaki "Numerical Investigation of the Energetic Particle Redistribution and Interaction with Alfvén Eigenmode in Heliotron J" *Physical Society of Japan, 2020 Autumn Meeting*, Online Conference, 8 September 2020, 8pB2-4

- ## Poster Presentations

1. P. Adulsiriswad, S. Yamamoto, Y. Todo, Y. Suzuki, K. Nagasaki, S. Ohshima, H. Okada, S. Kado, T. Minami, S. Kobayashi, and T. Mizuuchi "Study of Fast-ion-driven MHD Instabilities in Heliotron J Equilibrium by Particle-MHD Hybrid Simulation code MEGA" *American Physics Society Division of Plasma Physics Meeting 2018*, Portland, Oregon, United State of America, 7 November 2018

2. P. Adulsiriswad, Y. Todo, S. Yamamoto, S. Kado, S. Kobayashi, S. Ohshima, H. Okada, T. Minami, Y. Nakamura, A. Ishizawa, T. Mizuuchi, S. Konoshima, and K. Nagasaki "Hybrid Simulation of Global Alfvén Eigenmode and Energetic Particle Mode in Heliotron J, a Low Shear Helical Axis Heliotron" *16th IAEA Technical Meeting on Energetic Particles in Magnetic Confinement System*, Shizuoka, Japan, 4 September 2019, P2-11.

3. P. Adulsiriswad, Y. Todo, S. Yamamoto, S. Kado, S. Kobayashi, S. Ohshima, H. Okada, T. Minami, Y. Nakamura, A. Ishizawa, T. Mizuuchi, S. Konoshima, and K. Nagasaki "Simulation Study of Energetic Particle-Driven Modes in Helical Axis Heliotron with the Bump-on-tail and Slowing-down Energetic Particle Energy Distributions" *22nd International Stellarator and Heliotron Workshop*, Madison, Wisconsin, United State of America, 24 September 2019, P-28.

4. P. Adulsiriswad, Y. Todo, S. Kado, S. Yamamoto, S. Kobayashi, S. Ohshima, T. Minami, H. Okada, A. Ishizawa, Y. Nakamura, S. Konoshima, T. Mizuuchi, K. Nagasaki "Simulation study of Energetic Particle-driven MHD Modes and Energetic Particle Redistribution in Heliotron J" *4th Asia-Pacific Conference on Plasma Physics*, Online Conference, 26-31 October 2020, MF-P17

• Awards

1. Student Presentation Award of the Physical Society of Japan, Division 2 at 2020 Autumn meeting of the Physical Society of Japan "Numerical Investigation of the Energetic Particle Redistribution and Interaction with Alfvén Eigenmode in Heliotron J" *Physical Society of Japan, 2020 Autumn Meeting*, 8-11 September 2020, 8pB2-4

2. Poster Presentation Award in the 4th Asia-Pacific Conference on Plasma Physics (AAPPS-DPP) "Simulation Study of the Energetic Particle-driven MHD Modes and Energetic Particle Redistribution in Heliotron J" *4th Asia-Pacific Conference on Plasma Physics*, 26-31 October 2020, MF-P17

3. Student Award of Kyoto University, Institute of Energy Science and Engineering (令和2年度京都大学エネルギー理工学研究所学生賞) "ハイブリッドシミュレーションコードを用いたヘリオトロンJプラズマにおける高エネルギー粒子励起MHD不安定に関する研究," *Kyoto University, Institute of Advanced Energy*, 2020

Bibliography

[1] Francesco Berna, Paul Goldberg, Liora Kolska Horwitz, James Brink, Sharon Holt, Marion Bamford, and Michael Chazan. Microstratigraphic evidence of in situ fire in the acheulean strata of wonderwerk cave, northern cape province, south africa. *Proceedings of the National Academy of Sciences*, 109(20):E1215–E1220, 2012.

[2] British Petroleum Company. Bp statistical review of world energy. Technical report, 2020.

[3] Vaclav Smil. *Energy Transitions: Global and National Perspectives*. Praeger, Santa Barbara, California, 2017.

[4] International Energy Agency. Global energy-related co_2 emissions. https://www.iea.org/data-and-statistics/charts/global-energy-related-co2-emissions-1900-2020.

[5] Lyman Spitzer Jr. The stellarator concept. *The Physics of Fluids*, 1(4):253–264, 1958.

[6] John M Greene. A brief review of magnetic wells. *Comments on Plasma Physics and Controlled Fusion*, 17:389–402, 1997.

[7] Masahiro Wakatani. *Stellarator and heliotron devices*, volume 95. Oxford University Press on Demand, 1998.

[8] Mitsutaka Isobe, Kunihiro Ogawa, Takeo Nishitani, Hitoshi Miyake, Takashi Kobuchi, Neng Pu, Hoiroki Kawase, Eiji Takada, Tomoyo Tanaka, Siyuan Li, et al. Neutron diagnostics in the large helical device. *IEEE Transactions on Plasma Science*, 46(6):2050–2058, 2018.

[9] K Ogawa, M Isobe, K Toi, F Watanabe, Donald A Spong, A Shimizu, M Osakabe, S Ohdachi, S Sakakibara, LHD Experiment Group, et al. Observation of energetic-ion losses induced by various mhd instabilities in the large helical device (lhd). *Nuclear fusion*, 50(8):084005, 2010.

[10] K Ogawa, M Isobe, K Toi, A Shimizu, DA Spong, M Osakabe, S Yamamoto, LHD Experiment Group, et al. A study on the tae-induced fast-ion loss process in lhd. *Nuclear Fusion*, 53(5):053012, 2013.

[11] S Yamamoto, K Ogawa, M Isobe, DS Darrow, S Kobayashi, K Nagasaki, H Okada, T Minami, S Kado, S Ohshima, et al. Faraday-cup-type lost fast ion detector on heliotron j. *Review of Scientific Instruments*, 87(11):11D818, 2016.

[12] WW Heidbrink, CS Collins, M Podestà, GJ Kramer, DC Pace, CC Petty, L Stagner, MA Van Zeeland, RB White, and YB Zhu. Fast-ion transport by alfvén eigenmodes above a critical gradient threshold. *Physics of Plasmas*, 24(5):056109, 2017.

[13] CS Collins, WW Heidbrink, ME Austin, GJ Kramer, DC Pace, CC Petty, L Stagner, MA Van Zeeland, RB White, YB Zhu, et al. Observation of critical-gradient behavior in alfvén-eigenmode-induced fast-ion transport. *Physical review letters*, 116(9):095001, 2016.

[14] Ya I Kolesnichenko, VV Lutsenko, H Wobig, and V Yakovenko. Alfvén instabilities driven by circulating ions in optimized stellarators and their possible consequences in a helias reactor. *Physics of Plasmas*, 9(2):517–528, 2002.

[15] Ya I Kolesnichenko, A Könies, VV Lutsenko, and Yu V Yakovenko. Affinity and difference between energetic-ion-driven instabilities in 2d and 3d toroidal systems. *Plasma Physics and Controlled Fusion*, 53(2):024007, 2011.

[16] Ya I Kolesnichenko and AV Tykhyy. Landau damping of alfvénic modes in stellarators. *Plasma Physics and Controlled Fusion*, 60(12):125004, 2018.

[17] S Yamamoto, K Toi, N Nakajima, S Ohdachi, S Sakakibara, KY Watanabe, M Goto, K Ikeda, O Kaneko, K Kawahata, et al. Observation of helicity-induced alfven eigenmodes in large-helical-device plasmas heated by neutral-beam injection. *Physical review letters*, 91(24):245001, 2003.

[18] DA Spong, R Sanchez, and A Weller. Shear alfvén continua in stellarators. *Physics of Plasmas*, 10(8):3217–3224, 2003.

[19] M Wakatani, Y Nakamura, K Kondo, M Nakasuga, S Besshou, T Obiki, F Sano, K Hanatani, T Mizuuchi, H Okada, et al. Study of a helical axis heliotron. *Nuclear fusion*, 40(3Y):569, 2000.

[20] T Klinger, T Andreeva, S Bozhenkov, C Brandt, R Burhenn, B Buttenschön, G Fuchert, B Geiger, O Grulke, HP Laqua, et al. Overview of first wendelstein 7-x high-performance operation. *Nuclear Fusion*, 59(11):112004, 2019.

[21] Haifeng Liu, Akihiro Shimizu, Mitsutaka Isobe, Shoichi Okamura, Shin Nishimura, Chihiro Suzuki, Yuhong Xu, Xin Zhang, Bing Liu, Jie Huang, et al. Magnetic configuration and modular coil design for the chinese first quasi-axisymmetric stellarator. *Plasma and Fusion Research*, 13:3405067–3405067, 2018.

[22] S Yamamoto, Kazunobu Nagasaki, Y Suzuki, T Mizuuchi, H Okada, S Kobayashi, Boyd Blackwell, Katsumi Kondo, G Motojima, N Nakajima, et al. Observation of magnetohydrodynamic instabilities in heliotron j plasmas. *Fusion science and technology*, 51(1):92–96, 2007.

[23] S Kobayashi, K Nagaoka, S Yamamoto, T Mizuuchi, K Nagasaki, H Okada, T Minami, S Murakami, HY Lee, Y Suzuki, et al. Fast-ion response to energetic-particle-driven mhd activity in heliotron j. *Contributions to Plasma Physics*, 50(6-7):534–539, 2010.

[24] S Ohshima, S Kobayashi, S Yamamoto, K Nagasaki, T Mizuuchi, H Okada, T Minami, K Hashimoto, N Shi, L Zang, et al. Edge plasma responses to energetic-particle-driven mhd instability in heliotron j. *Nuclear Fusion*, 56(1):016009, 2015.

[25] S Yamamoto, K Nagasaki, S Kobayashi, K Nagaoka, A Cappa, H Okada, T Minami, S Kado, S Ohshima, S Konoshima, et al. Suppression of fast-ion-driven mhd instabilities by ech/eccd on heliotron j. *Nuclear Fusion*, 57(12):126065, 2017.

[26] LG Zang, S Yamamoto, DA Spong, K Nagasaki, S Ohshima, S Kobayashi, T Minami, XX Lu, N Nishino, S Kado, et al. Observation of a beam-driven low-frequency mode in heliotron j. *Nuclear Fusion*, 59(5):056001, 2019.

[27] S Kobayashi, H Okada, T Mizuuchi, K Nagasaki, S Yamamoto, K Hanatani, F Sano, M Kaneko, Y Suzuki, Y Nakamura, et al. Studies of high energy ions in heliotron j. 2005.

[28] M Kaneko, S Kobayashi, Y Suzuki, T Mizuuchi, K Nagasaki, H Okada, Y Nakamura, K Hnatani, S Murakami, K Kondo, et al. Fast ion dynamics of nbi plasmas in heliotron j. *Fusion science and technology*, 50(3):428–433, 2006.

[29] H Okada, Y Torii, S Kobayashi, M Kaneko, H Kitagawa, T Tomokiyo, H Takahashi, T Mutoh, T Mizuuchi, K Nagasaki, et al. Dependence of the confinement of fast ions generated by icrf heating on the field configuration in heliotron j. *Nuclear fusion*, 47(9):1346, 2007.

[30] NN Gorelenkov and SE Sharapov. On the collisional damping of tae-modes on trapped electrons in tokamaks. *Physica Scripta*, 45(2):163, 1992.

[31] J Varela, Kazunobu Nagasaki, Kenichi Nagaoka, Satoshi Yamamoto, KY Watanabe, Donald A Spong, Luis Garcia, Alvaro Cappa, and Akira Azegami. Modeling of the eccd injection effect on the heliotron j and lhd plasma stability. *Nuclear Fusion*, 60(11):112015, 2020.

[32] Y Todo and T Sato. Linear and nonlinear particle-magnetohydrodynamic simulations of the toroidal alfvén eigenmode. *Physics of plasmas*, 5(5):1321–1327, 1998.

[33] Y Todo, R Seki, DA Spong, H Wang, Y Suzuki, S Yamamoto, N Nakajima, and M Osakabe. Comprehensive magnetohydrodynamic hybrid simulations of fast ion driven instabilities in a large helical device experiment. *Physics of Plasmas*, 24(8):081203, 2017.

[34] Hao Wang, Yasushi Todo, Charlson C Kim, et al. Hole-clump pair creation in the evolution of energetic-particle-driven geodesic acoustic modes. *Physical review letters*, 110(15):155006, 2013.

[35] Christoph Slaby, Axel Könies, Ralf Kleiber, and José Manuel García-Regaña. Effects of collisions on the saturation dynamics of taes in tokamaks and stellarators. *Nuclear Fusion*, 58(8):082018, 2018.

[36] Donald A Spong, Ihor Holod, Y Todo, and M Osakabe. Global linear gyrokinetic simulation of energetic particle-driven instabilities in the lhd stellarator. *Nuclear Fusion*, 57(8):086018, 2017.

[37] Charlson C Kim, Carl R Sovinec, Scott E Parker, NIMROD Team, et al. Hybrid kinetic-mhd simulations in general geometry. *Computer physics communications*, 164(1-3):448–455, 2004.

[38] Yawei Hou, Ping Zhu, Charlson C Kim, Zhaoqing Hu, Zhihui Zou, Zhengxiong Wang, and NIMROD Team. Nimrod calculations of energetic particle driven toroidal alfvén eigenmodes. *Physics of Plasmas*, 25(1):012501, 2018.

[39] Jacobo Varela, Donald A Spong, and Luis Garcia. Analysis of alfven eigenmodes destabilization by energetic particles in tj-ii using a landau-closure model. *Nuclear Fusion*, 57(12):126019, 2017.

[40] Y Todo, MA Van Zeeland, A Bierwage, WW Heidbrink, and Max E Austin. Validation of comprehensive magnetohydrodynamic hybrid simulations for alfvén eigenmode induced energetic particle transport in diii-d plasmas. *Nuclear Fusion*, 55(7):073020, 2015.

[41] A Bierwage, K Shinohara, Y Todo, N Aiba, M Ishikawa, G Matsunaga, M Takechi, and M Yagi. Self-consistent long-time simulation of chirping and beating energetic particle modes in jt-60u plasmas. *Nuclear Fusion*, 57(1):016036, 2016.

[42] R Seki, Y Todo, Y Suzuki, K Ogawa, M Isobe, DA Spong, and M Osakabe. Hybrid simulation of nbi fast-ion losses due to the alfvén eigenmode bursts in the large helical device and the comparison with the fast-ion loss detector measurements. *Journal of Plasma Physics*, 86(5), 2020.

[43] Eugene Y Chen, HL Berk, B Breizman, and LJ Zheng. Free-boundary toroidal alfven eigenmodes. *Physics of Plasmas*, 18(5):052503, 2011.

[44] SX Yang, GZ Hao, YQ Liu, ZX Wang, YJ Hu, JX Zhu, HD He, and AK Wang. Toroidal alfvén eigenmode triggered by trapped anisotropic energetic particles in a toroidal resistive plasma with free boundary. *Nuclear Fusion*, 58(4):046016, 2018.

[45] Sergio Briguglio, G Fogaccia, G Vlad, F Zonca, K Shinohara, M Ishikawa, and M Takechi. Particle simulation of bursting alfvén modes in jt-60u. *Physics of Plasmas*, 14(5):055904, 2007.

[46] Liu Chen. Theory of magnetohydrodynamic instabilities excited by energetic particles in tokamaks. *Physics of Plasmas*, 1(5):1519–1522, 1994.

[47] Y Todo, T Sato, K Watanabe, TH Watanabe, and R Horiuchi. Magnetohydrodynamic vlasov simulation of the toroidal alfvén eigenmode. *Physics of Plasmas*, 2(7):2711–2716, 1995.

[48] N Nakajima, Chio-Zong Cheng, and Masao Okamoto. High-n helicity-induced shear alfvén eigenmodes. *Physics of Fluids B: Plasma Physics*, 4(5):1115–1121, 1992.

[49] K Toi, S Ohdachi, S Yamamoto, N Nakajima, S Sakakibara, KY Watanabe, S Inagaki, Y Nagayama, Y Narushima, H Yamada, et al. Mhd instabilities and their effects on plasma confinement in large helical device plasmas. *Nuclear fusion*, 44(2):217, 2004.

[50] Ya I Kolesnichenko, VV Lutsenko, A Weller, A Werner, Yu V Yakovenko, J Geiger, and OP Fesenyuk. Conventional and nonconventional global alfvén eigenmodes in stellarators. *Physics of Plasmas*, 14(10):102504, 2007.

[51] K Shinohara, Y Kusama, M Takechi, A Morioka, M Ishikawa, N Oyama, K Tobita, T Ozeki, S Takeji, S Moriyama, et al. Alfvén eigenmodes driven by alfvénic beam ions in jt-60u. *Nuclear fusion*, 41(5):603, 2001.

[52] Lev Davidovich Landau. On the vibrations of the electronic plasma. *Zh. Eksp. Teor. Fiz.*, 10:25, 1946.

[53] DJ Sigmar, CT Hsu, R White, and Chio-Zong Cheng. Alpha-particle losses from toroidicity-induced alfvén eigenmodes. part ii: Monte carlo simulations and anomalous alpha-loss processes. *Physics of Fluids B: Plasma Physics*, 4(6):1506–1516, 1992.

[54] Y Todo. Introduction to the interaction between energetic particles and alfven eigenmodes in toroidal plasmas. *Reviews of Modern Plasma Physics*, 3(1):1, 2019.

[55] T Obiki, F Sano, M Wakatani, K Kondo, T Mizuuchi, K Hanatani, Y Nakamura, K Nagasaki, H Okada, M Nakasuga, et al. Goals and status of heliotron j. *Plasma Physics and Controlled Fusion*, 42(11):1151, 2000.

[56] Masahiro Wakatani and Sigeru Sudo. Overview of heliotron e results. *Plasma physics and controlled fusion*, 38(7):937, 1996.

[57] T Obiki, S Sudo, and F Sano. Confinement improvement in ech and nbi heated heliotron e plasmas. In *Plasma physics and controlled nuclear fusion research 1990. V. 2*. 1991.

[58] HE Mynick, TK Chu, and AH Boozer. Class of model stellarator fields with enhanced confinement. *Physical Review Letters*, 48(5):322, 1982.

[59] Masayuki Yokoyama, Yuji Nakamura, and Masahiro Wakatani. An optimized helical axis stellarator with modulated l= 1 helical coil. *J. Plasma Fusion Res*, 73(7):723–731, 1997.

[60] M. Kaneko. ヘリオトロン J における高速イオンの挙動に関する研究. PhD thesis, Kyoto University, Kyoto, 2006.

[61] Panith Adulsiriswad, Y Todo, Satoshi Yamamoto, Shinichiro Kado, S Kobayashi, Shinsuke Ohshima, Hiroyuki Okada, T Minami, Yuji Nakamura, Akihiro Ishizawa, et al. Magnetohydrodynamic hybrid simulations of alfvén eigenmodes in heliotron j, a low shear helical axis stellarator/heliotron. *Nuclear Fusion*, 2020.

[62] Y Todo, HL Berk, and BN Breizman. Nonlinear magnetohydrodynamic effects on alfvén eigenmode evolution and zonal flow generation. *Nuclear Fusion*, 50(8):084016, 2010.

[63] Y Todo, HL Berk, and BN Breizman. Saturation of a toroidal alfvén eigenmode due to enhanced damping of nonlinear sidebands. *Nuclear Fusion*, 52(9):094018, 2012.

[64] Hao Wang and Yasushi Todo. Linear properties of energetic particle driven geodesic acoustic mode. *Physics of Plasmas*, 20(1):012506, 2013.

[65] Y Todo, MA Van Zeeland, and WW Heidbrink. Fast ion profile stiffness due to the resonance overlap of multiple alfvén eigenmodes. *Nuclear Fusion*, 56(11):112008, 2016.

[66] Andreas Bierwage, Kouji Shinohara, Yasushi Todo, Nobuyuki Aiba, Masao Ishikawa, Go Matsunaga, Manabu Takechi, and Masatoshi Yagi. Simulations tackle abrupt massive migrations of energetic beam ions in a tokamak plasma. *Nature communications*, 9(1):1–11, 2018.

[67] Y Todo. Critical energetic particle distribution in phase space for the alfvén eigenmode burst with global resonance overlap. *Nuclear Fusion*, 59(9):096048, 2019.

[68] XQ Wang, H Wang, Y Todo, Y Xu, JL Wang, HF Liu, J Huang, X Zhang, H Liu, J Cheng, et al. Nonlinear simulations of energetic particle-driven instabilities interacting with alfvén continuum during frequency chirping. *Plasma Physics and Controlled Fusion*, 63(1):015004, 2020.

[69] Jonhathan Pinon, Yasushi Todo, and Hao Wang. Effects of fast ions on interchange modes in the large helical device plasmas. *Plasma Physics and Controlled Fusion*, 60(7):075007, 2018.

[70] A Bierwage, Y Todo, N Aiba, and K Shinohara. Sensitivity study for n-nb-driven modes in jt-60u: boundary, diffusion, gyroaverage, compressibility. *Nuclear Fusion*, 56(10):106009, 2016.

[71] Robert G Littlejohn. Variational principles of guiding centre motion. *Journal of Plasma Physics*, 29(1):111–125, 1983.

[72] Hao Wang, Yasushi Todo, Takeshi Ido, and Masaki Osakabe. Simulation study of high-frequency energetic particle driven geodesic acoustic mode. *Physics of Plasmas*, 22(9):092507, 2015.

[73] Oscar Buneman. Dissipation of currents in ionized media. *Physical Review*, 115(3):503, 1959.

[74] John Dawson. One-dimensional plasma model. *The Physics of Fluids*, 5(4):445–459, 1962.

[75] D Tskhakaya, K Matyash, R Schneider, and F Taccogna. The particle-in-cell method. *Contributions to Plasma Physics*, 47(8-9):563–594, 2007.

[76] Richard Courant, Kurt Friedrichs, and Hans Lewy. Über die partiellen differenzengleichungen der mathematischen physik. *Mathematische annalen*, 100(1):32–74, 1928.

[77] Satoshi Yamamoto, Gen Motojima, Shinji Kobayashi, Tohru Mizuuchi, Hiroyuki Okada, Kazunobu Nagasaki, Boyd Blackwell, Katsumi Kondo, Yuji Nakamura, Noriyoshi Nakajima, et al. Energetic ion driven mhd instabilities and their impact on ion transport in heliotron j plasmas. Joint Conference of 17th International Toki Conference and 16th . . . , 2007.

[78] K Nagasaki, S Yamamoto, S Kobayashi, K Sakamoto, Y Nagae, Y Sugimoto, YI Nakamura, G Weir, N Marushchenko, T Mizuuchi, et al. Stabilization of energetic-ion-driven mhd modes by eccd in heliotron j. *Nuclear Fusion*, 53(11):113041, 2013.

[79] Satoshi Yamamoto, Kazunobu Nagasaki, Kenichi Nagaoka, Jacobo Varela, Alvaro Cappa, Enrique Ascasibar, Francisco Castejon, Josep Maria Fontdecaba, José Manuel García Regaña, Antonio González, et al. Effect of ech/eccd on energetic-particle-driven mhd modes in helical plasmas. *Nuclear Fusion*, 2020.

[80] Y. Nakamura, Y. Suzuki, S. Yamagishi, K. Kondo, N. Nakajima, T. Hayashi, DA Monticello, and AH Reiman. Mhd equilibrium and pressure driven instability in l= 1 heliotron plasmas. *Nuclear fusion*, 44(3):387, 2004.

[81] Yasuhiro Suzuki, Yuji Nakamura, Katsumi Kondo, Takaya Hayashi, SS Lloyd, and Henry James Gardner. Mhd equilibrium of a low-shear helical axis heliotron. *Plasma physics and controlled fusion*, 45(6):971, 2003.

[82] Y. Suzuki, Y. Nakamura, K. Kondo, N. Nakajima, and T. Hayashi. Mhd equilibrium of heliotron j plasmas. In *Progress in plasma theory and understanding of fusion plasmas: ITC-13 Proceedings*. 2004.

[83] G Motojima, K Nagasaki, M Nosaku, H Okada, KY Watanabe, T Mizuuchi, Y Suzuki, S Kobayashi, K Sakamoto, S Yamamoto, et al. Control of non-inductive current in heliotron j. *Nuclear Fusion*, 47(8):1045, 2007.

[84] Allen H Boozer. Establishment of magnetic coordinates for a given magnetic field. Technical report, Princeton Univ., NJ (USA). Plasma Physics Lab., 1981.

[85] Y Todo, Masahiko Sato, Hao Wang, Malik Idouakass, and Ryosuke Seki. Magnetohydrodynamic hybrid simulation model with kinetic thermal ions and energetic particles. *Plasma Physics and Controlled Fusion*, 2021.

[86] Mario Podesta, Laszlo Bardoczi, CS Collins, Nikolai N Gorelenkov, William W Heidbrink, Vinicius N Duarte, Gerrit J Kramer, Eric D Fredrickson, Marina Gorelenkova, Doohyun Kim, et al. Reduced energetic particle transport models enable comprehensive time-dependent tokamak simulations. *Nuclear Fusion*, 59(10):106013, 2019.

[87] LW Yan, XR Duan, XT Ding, JQ Dong, QW Yang, Yi Liu, XL Zou, DQ Liu, WM Xuan, LY Chen, et al. Overview of experimental results on the hl-2a tokamak. *Nuclear Fusion*, 51(9):094016, 2011.

[88] M Sato and A Ishizawa. Nonlinear parity mixtures controlling the propagation of interchange modes. *Physics of Plasmas*, 24(8):082501, 2017.

[89] A Weller, M Anton, J Geiger, M Hirsch, R Jaenicke, A Werner, W7-AS Team, C Nührenberg, E Sallander, and DA Spong. Survey of magnetohydrodynamic instabilities in the advanced stellarator wendelstein 7-as. *Physics of Plasmas*, 8(3):931–956, 2001.

[90] Andreas Bierwage and Kouji Shinohara. Orbit-based analysis of resonant excitations of alfvén waves in tokamaks. *Physics of Plasmas*, 21(11):112116, 2014.

[91] HL Berk, BN Breizman, and M Pekker. Nonlinear dynamics of a driven mode near marginal stability. *Physical review letters*, 76(8):1256, 1996.

[92] BN Breizman, HL Berk, MS Pekker, F Porcelli, GV Stupakov, and KL Wong. Critical nonlinear phenomena for kinetic instabilities near threshold. *Physics of Plasmas*, 4(5):1559–1568, 1997.

[93] HL Berk, BN Breizman, J Candy, M Pekker, and NV Petviashvili. Spontaneous hole–clump pair creation. *Physics of Plasmas*, 6(8):3102–3113, 1999.

[94] K Nagaoka, T Ido, E Ascasíbar, T Estrada, S Yamamoto, AV Melnikov, A Cappa, C Hidalgo, MA Pedrosa, B Ph Van Milligen, et al. Mitigation of nbi-driven alfvén eigenmodes by electron cyclotron heating in the tj-ii stellarator. *Nuclear Fusion*, 53(7):072004, 2013.

[95] Avrilios Lazaros, Akihiro Shimizu, Yasuo Yoshimura, Keisuke Matsuoka, Shoichi Okamura, Chihiro Suzuki, and CHS Group. New experimental evidence for the stabilizing effect of a superthermal electron avalanche during electron cyclotron resonant heating. *Physics of Plasmas*, 9(7):3007–3012, 2002.

[96] HL Berk, BN Breizman, and NV Petviashvili. Spontaneous hole-clump pair creation in weakly unstable plasmas. *Physics Letters A*, 234(3):213–218, 1997.

[97] VS Marchenko and SN Reznik. Excitation of the beta-induced alfven eigenmodes by a magnetic island. *Nuclear fusion*, 49(2):022002, 2008.

[98] Alessandro Biancalani, Liu Chen, Francesco Pegoraro, and Fulvio Zonca. Continuous spectrum of shear alfvén waves within magnetic islands. *Physical review letters*, 105(9):095002, 2010.

[99] BJ Sun, MA Ochando, and D López-Bruna. Alfvén eigenmodes including magnetic island effects in the tj-ii stellarator. *Nuclear Fusion*, 55(9):093023, 2015.

[100] Hao Wang, Yasushi Todo, Masaki Oasakabe, Takeshi Ido, and Yasuhiro Suzuki. Simulation of energetic particle driven geodesic acoustic modes and the energy channeling in the large helical device plasmas. *Nuclear Fusion*, 59(9):096041, 2019.

[101] Hao Wang, Yasushi Todo, Masaki Osakabe, Takeshi Ido, and Yasuhiro Suzuki. The systematic investigation of energetic-particle-driven geodesic acoustic mode channeling using mega code. *Nuclear Fusion*, 60(11):112007, 2020.